Title

Earthquakes of Varying Depths: Understanding Seismicity at Volcanic Summits and in Subducting Slabs

Permalink

https://escholarship.org/uc/item/54b4g2bb

Author

Fildes, Rebecca

Publication Date

2023

Peer reviewed|Thesis/dissertation

Earthquakes of Varying Depths:
Understanding Seismicity at Volcanic Summits and in Subducting Slabs

By

REBECCA A. FILDES
DISSERTATION

Submitted in partial satisfaction of the requirements for the degree of

DOCTOR OF PHILOSOPHY

in

Earth and Planetary Sciences

in the

OFFICE OF GRADUATE STUDIES

of the

UNIVERSITY OF CALIFORNIA

DAVIS

Approved:

_____

Magali I. Billen, Chair

_____

Maxwell L. Rudolph

_____

John B. Rundle

Committee in Charge

2023

i

Contents

Abstract

Earthquakes occur in a variety of geologic settings throughout the Earth: from volcanic summits all the way down to depths of 660 km at the bottom of the mantle transition zone. Though they pose significant hazard in some regions, earthquakes are also scientific opportunities to gain insight about different processes within the Earth system. Earthquakes all share the common behavior of suddenly releasing energy that had been stored within rock, but the driving forces and physical conditions of individual systems where they occur varies greatly. Earthquake observations that characterize rupture source properties reveal both the similarities and differences between shallow and deep earthquakes. These are key to differentiating the types of processes that could be leading to earthquake failure in different systems under varying physical conditions. Our general understanding of earthquake proprieties are used in the studies presented here to help guide investigations of both volcanic systems and subducting slabs. Here we present two types of earthquake analyses: statistical modeling of shallow volcanic earthquakes and geodynamic modeling for deep earthquake investigation.

In a volcanic setting, the driving forces behind the stress changes in the system leading to seismicity can be associated with magma migration and pressure changes within the plumbing of a volcano. Improving our understanding of this relationship could help us to utilize future earthquake occurrences in interpreting changes in a volcano's behavior. Here we use earthquake statistics and statistical hazard modeling to investigate earthquakes occurring during the active 2018 Kīlauea Volcano eruption and find changes in earthquake behavior that temporally align with physical changes in the behavior of the larger volcanic system. Much deeper below Earth's surface, in subducting lithosphere, the driving forces leading to deep

(>70 km) earthquakes are associated with the long-term deformation of the subducting slab. Although they do not pose the seismic hazard that the Kīlauea earthquakes do, improving our understanding of how these unusual earthquakes can occur at high temperatures and pressures found in the deep slab can help us better understand the rheology of Earth's lithosphere as well as what processes may be going on within it (e.g., phase transitions, thermal shear heating). For this portion of the thesis we present novel numerical subduction modeling methods developed specifically to be paired with deep earthquake observations to investigate the role long-term strain-rates play in where deep earthquakes occur.

Understanding both the commonalities and differences between the types of earthquakes observed at volcanic summits and within subducting lithosphere is helpful for understanding more general earthquake behavior. Earthquakes are both a hazard that needs improved understanding, as well as a vital tool themselves to better understanding different lithospheric processes of varying temporal and spatial scales across Earth's system.

Acknowledgments

First, thank you to my family for supporting me from the other side of the country, coming to visit here in California, and showing enthusiasm when I talk to them about the cool rocks we see on their trips.

Thank you to my thesis committee members Max Rudolph and John Rundle for their insight and feedback on research projects. I had numerous insightful conversations with Max and appreciate his pointed questions and focus on details of different parameter choices and method implementations in my numerical models. John provided a lot of perspective on the earthquake statistics work in the early part of this thesis I am grateful for, as well as the invaluable experiences I had on our trip together to Japan for a hazards workshop. Thank you to Don Turcotte for his instrumental insight and support during the early parts of my PhD especially. I very much value the conversations we had about earthquake statistics and volcano dynamics. I will always remember the advice Don gave me before attending my first conference, "The best science happens drinking gin and tonics by the pool". I am very grateful for the support from and countless conversations with Jim McClain. From my own research topics to science hobbies like moonquakes and marsquakes, I always enjoyed our conversations. The 3 summers I spent TAing geophysics summer field hold some very special memories, and I value all I learned from you in Bishop and the Eastern Sierra.

Shout-out to the Billen Group! It has been a great atmosphere to learn and collaborate in with Menno, Haoyuan, and Trey in our lab group. I have really enjoyed the collaborative atmosphere where it felt like we were all enjoying the science we were doing and learning

from each other, which stemmed from Magali. I have to acknowledge the structure-tectonics group in the department where I spent a lot of time in interdisciplinary reading groups and on field trips. These were very important for my interdisciplinary development as an Earth scientist. It was very much appreciated that I was welcomed into these groups as someone with very little geology background and who was doing no field geology as part of their own research. After being here for 6 years there are so many more grad students and faculty I am grateful for in our department. Specifically, Hannah, Elizabeth, Kaitlyn, Alba, Vero, Dylan, Chris, and Elaine. I have loved teaching with you, learning with you, talking about research together, going on field trips, and generally being in a space where our shared enthusiasm for science and our support for each other go hand in hand.

During the course of my PhD I learned from two incredible advisors who shared the qualities of enjoyment and enthusiasm in the impressive research they conduct, as well as understanding and support for their students as both people and academics. My first advisor, Louise Kellogg, was the reason I came to Davis in the first place. She was encouraging of me asking my own questions, and helpful in forming my initial thesis projects. Even when she was out sick, she would send me new videos or news stories coming out of the Kīlauea eruption that she found interesting or cool and wanted to share. It seemed like she always enjoyed the science and enjoyed the process of asking new questions. I will always be grateful for Louise's support and sensitivity when we lost our department member Eldridge Moores on a field trip I was attending. I am extremely grateful for the short time I was able to learn from her and feel both her balance of support and enthusiasm for Earth science questions.

Although Magali Billen was not here during my first year at Davis and we did not formally meet until midway through my second year, I now cannot imagine my PhD without her. Her support and guidance academically and personally began before she was even my advisor, when she returned from sabbatical, and has never wavered over the last 4.5 years. From helping me get my Kīlauea work published, to offering me a place in her lab and being patient with me as I started a brand new research project, all while checking in on

my mental and emotional well-being, I am extremely grateful for her support. I have loved working on the deep earthquake project with Magali and really have enjoyed learning from and collaborating with her on all the facets of this project. Her enthusiasm and enjoyment of the science she does is contagious and it has been really fun pursuing our research questions together. Throughout our time together the balance of sensitivity, awareness, space, and support I have felt from her has been more than I could've asked for and it is hard to put into words how grateful I am for that.

Lastly, I have to acknowledge all of the support and guidance Jody has provided over the last 4 years in helping me process the losses of Eldridge and Louise and the lingering effects of these events. I am extremely grateful for our relationship and her continued guidance.

Although, my PhD took many turns and did not end up how I had envisioned it, I am so grateful I got to work with all the scientists I did, and was able to be a part of the EPS community. It is hard to put into words what this community and it's individual members have meant to me over the last 6 years, but through the ups and downs of my PhD, I am so grateful I chose UCD to pursue my PhD.

Chapter 1

Interevent Seismicity Statistics Associated With the 2018 Quasiperiodic Collapse Events at Kīlauea, HI, USA

1.1   Introduction of Published Manuscript 1

The work of my first chapter was published in Earth and Space Science, an American Geophysical Union (AGU) journal in 2020. See Appendix A for license to include in this thesis. The research in this first chapter was conducted with my advisor at the time, Louise Kellogg. The research methods were developed collaboratively with Louise and Donald Turcotte, with many useful conversations with John Rundle.

The funding for this project was provided through grants awarded Louise Kellogg and the UC Davis Graduate Studies Summer GSR Award for Engineering or Computer-related Applications and Methods.

Earth and Space Science

Correspondence to:
R. A. Fildes,
rfildes@ucdavis.edu

Interevent Seismicity Statistics Associated With the 2018 Quasiperiodic Collapse Events at Kīlauea, HI, USA

Rebecca A. Fildes[1] , Louise H. Kellogg[1] , Donald L. Turcotte[1] , and John B. Rundle[1,2]

[1]Department of Earth and Planetary Sciences, University of California, Davis, CA, USA, [2]Department of Physics, University of California, Davis, CA, USA

Abstract Following the M_w 6.9 Hawaiian earthquake on 4 May 2018, a remarkable quasiperiodic sequence of collapse events began at Halemaʻumaʻu Crater at the summit of Kīlauea Volcano. The collapse events were associated with the drainage of magma from beneath the summit to the Lower East Rift Zone where fissure eruptions occurred. From 4 June 2018 to 2 August 2018 forty-seven collapse events M_w 5.3 ± 0.1 occurred with the same temporal pattern of seismicity occurring between sequential pairs of collapse events. This paper focuses on this interevent seismicity pattern. Following a collapse event, there was a relatively quiescent period. This was followed by a sudden increase in seismicity, occurring at a nearly linear rate of 397 ± 96 earthquakes per day. These seismically active periods lasted until the next collapse event occurred. The pattern then repeated itself beginning again with postcollapse quiescence. We provide a statistical summary of this seismicity behavior by isolating the quiescent and active times to look at immediate precollapse and postcollapse activity. In mid-June there were significant changes in the quiescent time lengths (decreased), the number of earthquakes during the interevent times (increased), and the rates of seismicity during the active times (increased). This type of interevent study could be conducted with other seismically well recorded, sequential caldera collapse events and also with other data types to look for potential physical explanations and an improved understanding of precollapse and postcollapse activity.

1. Introduction

The 2018 seismic and volcanic activity associated with Kīlauea Volcano provides a unique opportunity to study a very well recorded, staged caldera collapse sequence associated with extensive magma drainage and lava eruptions. The 2018 events included magma draining from the summit, 24 fissure eruptions in the Lower East Rift Zone (LERZ) covering 35.5 km^2, and a quasiperiodic sequence of 62 distinct caldera collapse events at the summit associated with extensive seismicity (Neal et al., 2019). This unique set of caldera collapse events was associated with inflation and deflation cycles of the volcano's summit as well as swarms of seismicity (Neal et al., 2019).

In addition to the frequent collapse events occurring with relatively consistent large moment magnitudes, there was a high level of smaller seismicity occurring around the summit (Neal et al., 2019). In early June, the collapse events had become more periodic and a regular pattern of this smaller magnitude seismicity was observable between sequential collapses. In contrast to a typical tectonic M_w 5 earthquake, which would produce an aftershock sequence with an exponential decay rate, these large seismic volcanic events were preceded by very high rates of seismicity and followed by relative seismic quiescence. A previous study of three basaltic caldera collapses (Piton de la Fournaise, Fernandina, and Miyakejima) focused on the temporal trend of total interevent time between stages of collapse and concluded that understanding interevent times is important to better understand the overall collapse dynamics (Michon et al., 2011).

Therefore, as a consistent feature of the interevent times, we chose to break down and study these smaller magnitude earthquake patterns to look for any significant changes throughout the sequence that may be associated with other physical changes in the system. This is a different approach to breaking down the interevent seismicity that has not been utilized in past large, episodic caldera collapse event studies analyzing Bárdarbunga Volcano, Miyakejima Volcano, Piton de la Fournaise, and Fernandina. Studies such as Kobayashi et al. (2003) (Miyakejima), Filson et al. (1973) (Fernandina), and Francis (1974) (Fernandina) have focused on caldera collapse related seismicity, but the sequence of events during the Kīlauea caldera collapse differed in both levels of activity and density of monitoring equipment recording the events. The

2

quality and quantity of seismic data collected throughout the 2018 Kīlauea sequence of events offers the unique opportunity to apply this approach to breaking down the interevent seismicity, but it could also be applied to other seismically well recorded collapse events in the future.

The purposes of this paper are (1) to introduce this approach to characterizing the precollapse and postcollapse event earthquakes so that it might be utilized in future studies and (2) present the statistical results for Kīlauea to make them available to researchers examining the collapse process through other data or physical models of the volcanic system and collapse process.

2. Observations and Geologic Setting

2.1. The 2018 Kīlauea Eruption

Neal et al. (2019) provided a thorough timeline of the volcanic and seismic events, which occurred during the 2018 period of heightened activity. They describe summit subsidence and the draining of the summit lava lake in Halemaʻumaʻu Crater beginning on 1 May 2018 at the start of the eruptive sequence. They reported that a M_w 6.9 tectonic earthquake occurred on 4 May on a thrust fault dipping at 20° to the northwest beneath the southeastern flank of Kīlauea Volcano. Displacement on this fault resulted in the subsidence of the southeastern flank of the volcano. They also report that this earthquake further opened the rift zone and aided in magma transport away from the summit. According to Neal et al. (2019), after the M_w 6.9 event, the drainage of the summit lava lake increased and by 10 May the lava lake was out of view from the rim of the crater. Also, at this time they detail that ash explosions and eruptions were occurring at the summit as well as an increasing number of mid-magnitude earthquakes (M 3–4). At the end of May, subsidence of the caldera floor around Halemaʻumaʻu Crater began.

From 16 May to 2 August there were 62 total collapse events within the summit caldera, which were described by Neal et al. (2019) as very long period (VLP) events with the sources of these events associated with changes in volume. Initially, large emissions of ash and volcanic gases were reportedly associated with these events. From middle-late May, the first 12 of these collapse events at the summit occurred at irregular intervals with associated explosions. They also reported that they were preceded by a small inflationary period and produced seismic signals assigned moment magnitudes of 4.9 ± 0.2. Subsequently, these explosive irregular events became more periodic collapse events within Halemaʻumaʻu Crater, though with a double-couple component as reported in the United States Geological Survey (USGS) (2018a). From late May to early August, these latter 50 large collapse events occurred almost daily at the summit with M_w 5.3 ± 0.1. According to Neal et al. (2019), each collapse event resulted in the floor of the caldera dropping several meters. The summit magma chamber was continually drained sending magma down rift to the LERZ, and this episodic sequence of collapse events continued. They state that 2 August is when the final collapse event occurred at the summit and by 4 August the summit subsidence, the small seismicity, and the LERZ effusion had slowed or stopped. The walls of the deepened caldera extend to heights up to 100 m (Neal et al., 2019). A highly detailed account of the entire sequence broken up into daily reports has been given by the Hawaii Volcano Observatory (HVO) of the United States Geological Survey (USGS) (2018b).

2.2. Kīlauea Volcano

Kīlauea, a basaltic shield volcano, is the southeastern most of the five volcanic systems that make up the island of Hawaiʻi, located in Hawaii, USA. A shaded relief map illustrating the surface structure of the summit caldera and Halemaʻumaʻu Crater prior to the 2018 events as well as their geographic location is given in Figure 1. A major feature within the large summit caldera at Kīlauea is Halemaʻumaʻu Crater, which is nearly circular and had a diameter of about 1 km prior to the most recent sequence of collapse events. Kīlauea has two active rift zones on the southern and eastern flanks of the volcano extending from the summit to below sea level. The LERZ has been particularly active in recent history in comparison to the less active southwest rift zone (e.g., Epp et al., 1983; Wolfe et al., 1987).

Kīlauea Volcano is the result of hot spot volcanism and produces basaltic magmas with low viscosities (Turcotte & Schubert, 2014). Shield volcanoes such as Kīlauea contain near-surface magma chambers that play an important role in activity. Input of magma from depth results in the growth and inflation of the magma chamber. Surface eruptions reduce the size of the magma chamber resulting in deflation (Lacey et al., 1981). Episodic inflation-deflation events at Kīlauea have been extensively studied to gain insight
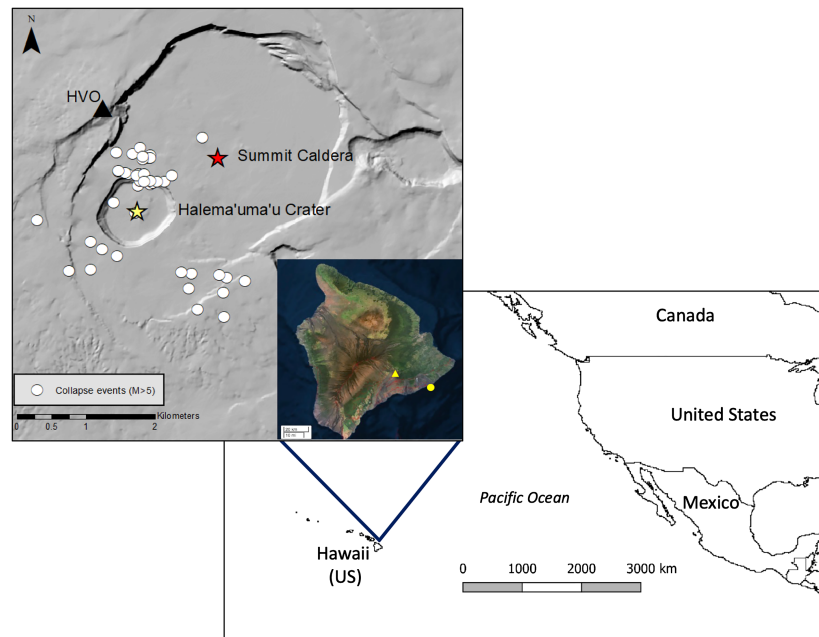
3

Figure 1. Hawaii's geographic location featuring a shaded relief map showing the Kīlauea summit caldera prior to the 2018 events discussed in this paper. Epicenters of the 47 large collapse events during our study period are indicated by the white circles. The red and yellow stars indicate the centers of the summit caldera and Halemaʻumaʻu Crater, respectively, and the black triangle indicates the location of the Hawaiian Volcano Observatory (HVO). *Inset:* The Island of Hawaiʻi with the locations of Kīlauea's summit (yellow triangle) and the epicenter of the M_w 6.9 mainshock (yellow circle).

into the volcanic system. Eaton and Murata (1960) looked at swelling activity of the summit caldera using tiltmeter data from the 1959–1960 eruptions. Other examples include the 1969–1971 Mauna Ulu eruption (Swanson et al., 1979) and the 1983–1985 East Rift Zone eruption (Wolfe et al., 1987). Heliker and Mattox (2003) reported summit inflation-deflation events associated with fountaining eruptions of the LERZ. Mechanisms responsible for these events may include a temporary blockage in magma supply (Cervelli & Miklius, 2003) and/or convective overturns of the summit magma reservoir (Poland et al., 2009). Tilling et al. (2010) have also given an excellent overview of the volcanism at Kīlauea emphasizing the role of inflation-deflation cycles. Anderson et al. (2015) associate prior episodic summit inflation-deflation events to pressure variations in a shallow magma chamber located beneath the east margin of the Halemaʻumaʻu Crater.

Colella and Dieterich (2015) considered in detail a sequence of 47 inflation-deflation cycles at Kīlauea from 1983 to 1985 associated with fountaining eruptions. This eruption cycle had a number of similarities to the eruption cycle considered in this paper. The inflations and deflations occurred at the summit caldera, and the eruptions of lava occurred in the LERZ. They noted that as an inflation period ended there was an increase in seismicity that was attributed to the stress accumulation in the summit from the intrusion of magma. Similarly, they attribute the decrease in seismicity during deflation to stress relaxation as magma was transported along the rift zone to the eruption site. Inflation occurred in one or more magma chambers beneath the Kīlauea summit caldera and was concentrated near Halemaʻumaʻu Crater. However, no systematic sequence of episodic caldera collapse events occurred as in the 2018 eruption.

3. Methods

3.1. Data Selection

In this study, we analyze the earthquake data from the USGS Earthquake Catalog that occurred on the Island of Hawaii between 4 May 2018 and 15 August 2018. The following sections explain our initial
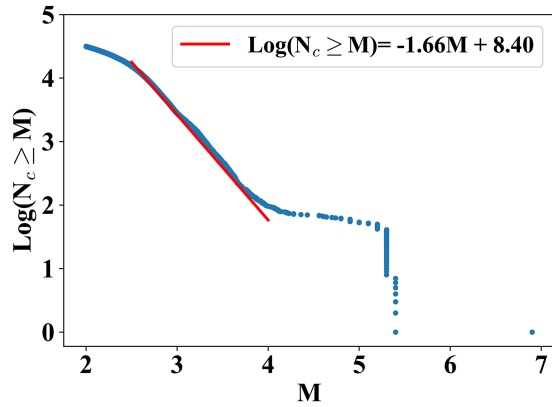
Figure 2. The frequency-magnitude statistics of earthquakes from 4 May 2018 to 2 August 2018. The red line shows the Gutenberg-Richter fit for $2.5 \leq M \leq 4.0$. The 62 caldera collapse events are included and make up the majority of the $4.7 \leq M \leq 5.4$ events.

investigation of this full data set as well as our methods to select a subset of this data to apply our technique to. All times considered here are Greenwich Mean Time. We begin counting time t (in days) at the time of occurrence of the $M_w = 6.9$ tectonic earthquake as this is a well-defined and significant event at the beginning of the whole sequence of heightened activity. This earthquake occurred at 22:32:54 on 4 May 2018, which will be $t = 0$. The timeline concludes with the occurrence of the last collapse event at $t = 89.97$ days, on 2 August 2018. During this entire sequence 62 collapse events occurred with most events radiating seismic energy equivalent to a magnitude $M_w = 5 \pm 0.3$ earthquake (Neal et al., 2019).

3.1.1. Magnitude

We consider the frequency-magnitude statistics of the earthquakes in the study region from 4 May to 2 August 2018. The cumulative number of earthquakes N_c with a magnitude greater than or equal to M is given as a function of M in Figure 2. In many cases the frequency-magnitude scaling of earthquakes is well approximated by the Gutenberg-Richter relation given by

$$\log_{10}(N_c) = a - bM \tag{1}$$

where a is a measure of seismic intensity and the b value is the scaling relating the number of small events to large events and is generally near 1 (Gutenberg & Richter, 1954). The smaller event magnitudes are given in local or duration magnitude, and the larger events are given in moment magnitude.

We give the least squares fit of equation (1) to the data in Figure 2 over the magnitude range $2.5 \leq M \leq 4.0$ and find that $a = 8.40$ and $b = 1.66$. The rollover of the data at small magnitudes, $M \leq 2.5$, is attributed to the incompleteness of the catalog data. The sensitivity of the network has a considerably lower cutoff, but the very high rate of seismicity saturates the seismic records and causes the observed rollover. For this reason, the analysis carried out in this study uses only events $M \geq 2.5$.

3.1.2. Temporal

We introduce a timeline, illustrated in Figure 3, to provide a basis for explaining the temporal evolution of seismicity associated with the collapse events. We show the accumulation of earthquakes, including collapse events, from the M_w 6.9 earthquake on 4 May 2018 ($t = 0$) to the last collapse event on 2 August 2018 ($t = 89.97$). In Figure 3a we give the cumulative number N_c of earthquakes with $M \geq 4.7$ (the minimum magnitude of large collapse events) as a function of time t. The large aftershocks of the M_w 6.9 earthquake can be observed in the first cluster of events, and the remainder of the data is collapse events (Neal et al., 2019). The rate of occurrence of collapse events becomes quasiperiodic in early June, about one per day, and slowly decreases until the sequence terminates on 2 August 2018. In Figure 3b, we give the cumulative number N_c of earthquakes with $M \geq 2.5$ as a function of time t. As the collapse events become more periodic, you can see in Figure 3b that the rate of small seismicity greatly increases. The shaded red region of Figures 3a and 3b, 4 June to 2 August 2018, which contain this heightened period of small seismicity among 47 quasiperiodic collapse events, was selected as the study period we focus on in this paper.

3.1.3. Spatial

We now turn to the spatial dependence. This study is focused on temporal patterns so we use the available locations from the USGS Earthquake Catalog. The distribution in space of the epicenters of the seismicity is qualitatively very similar for the 46 interevent periods from 4 June to 2 August. We illustrate the distribution for a typical interevent period. The summit distribution of the epicenters of $M \geq 2.5$ earthquakes between the collapse events at $t = 53.42$ and $t = 54.68$ days is given in Figure 4a as an example. It can be seen that the epicenters are concentrated in the summit caldera. The seismicity is mainly concentrated at the summit but becomes more diffuse downslope and to the rest of the island (not pictured).

In order to quantify the spatial distribution of epicenters in Figure 4a, we give the distribution of radial distances from the center of the caldera. The center we take is the red star in Figure 1, and the distribution is given in Figure 4b. We see that 95% of the total number of earthquakes with $M \geq 2.5$ that occurred on the
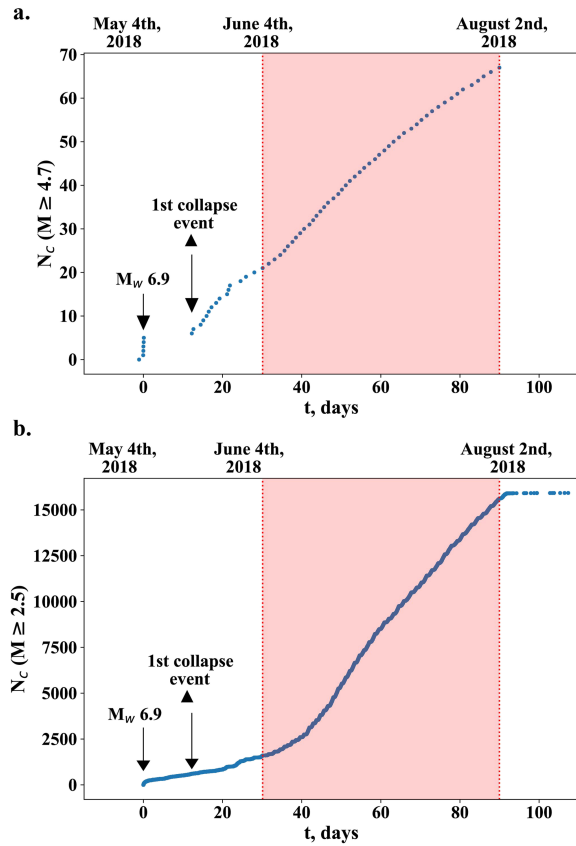
Figure 3. (a) The blue dots count the cumulative number, N_c, of $M \geq 4.7$ earthquakes and collapse events as a function of time t. (b) Same plot as (a) but for $M \geq 2.5$. The red shaded region (identical on both plots), 4 June 2018 to 2 August 2018 ($t = 30.13$–89.97), indicates the time period on which the statistical analysis of this study focuses.

island of Hawai'i during the interval considered in Figure 4a lie within a circle, centered at the red star, with radius of $r = 4.15$ km. They are concentrated near the summit. The seismicity becomes more diffuse downslope, but there is no well-defined bound on this. We use this statistic to justify using the seismicity for the entire island of Hawai'i in our study. Using the lower cutoff of $M \geq 2.5$ eliminates a lot of the smaller seismicity associated with other activity downrift.

3.2. Interevent Seismicity

The focus of this study is on the smaller seismicity occurring during 46 interevent periods between 47 collapse events. A subset of the timeline of seismicity and collapse events is given in Figure 5. Seismic behavior between collapse events was remarkably similar. A typical example of an interevent period is given in Figure 6 for the time between the collapse events that occurred in late June at $t = 53.42$ and $t = 54.68$ days (same interval illustrated in Figure 4 for spatial data selection). Following a collapse event, there is a relatively quiescent period. This is followed by a gradual buildup of seismicity into an active period with a near-constant rate of seismicity that continues until the next collapse event. The first period, the quiescent time, clearly has a different behavior than the latter period, the active time. By splitting the total interevent time and isolating these time periods, we look at immediate precollapse and immediate postcollapse dynamics in the seismicity.

The boundary between these two time periods was determined quantitatively. We began with a small window of time at the end of an interevent period and fit a straight line to this subset of data with a least squares linear regression. We iteratively increased the length of time included in the regression, extending to earlier times, until the correlation coefficient began to decrease. This was taken as the point of curvature of the data. We used the slope of this linear regression as the rate of seismicity, earthquakes per day, and the x intercept of the line to divide the quiescent period and the active period. This was done manually for each of the 46 interevent periods.

In order to look at the precollapse and postcollapse event activity throughout the sequence as a whole, five main characteristics of each interevent period were measured. For each interevent period, we measured the total interevent time between collapse events (Δt), duration of quiescent time (t_q), duration of active time (t_a), rate of seismicity during the active time ($\frac{dN_c}{dt}$), and the total number of events that occurred during the interevent time (N_c) (Figure 6). We also used Gutenberg-Richter statistics on each interevent time, quiescent time, and active time to look for trends in magnitude distributions (b values).

4. Results

Overall, the pattern of collapse event, quiescent time, and active time repeated itself 46 times between the 47 collapse events within our study period. In Figure 7 we give the time series of the smaller seismicity statistics throughout our study period. These time series can be classified as weakly antipersistent, with the cumulative number of events displaying the strongest antipersistence. An antipersistent time series has alternating highs and lows (sequential values are negatively correlated), whereas a persistent series would have values that consistently increase or consistently decrease (sequential values are positively correlated) (Turcotte, 1997). This is nonunique in general eruptive behavior in that Newman et al. (2012) illustrate, for example, that a shorter interevent time between eruptions of the Old Faithful geyser in Yellowstone National Park follows a longer interevent time, and a longer interevent time follows a shorter interevent time and thus classify it as antipersistent.
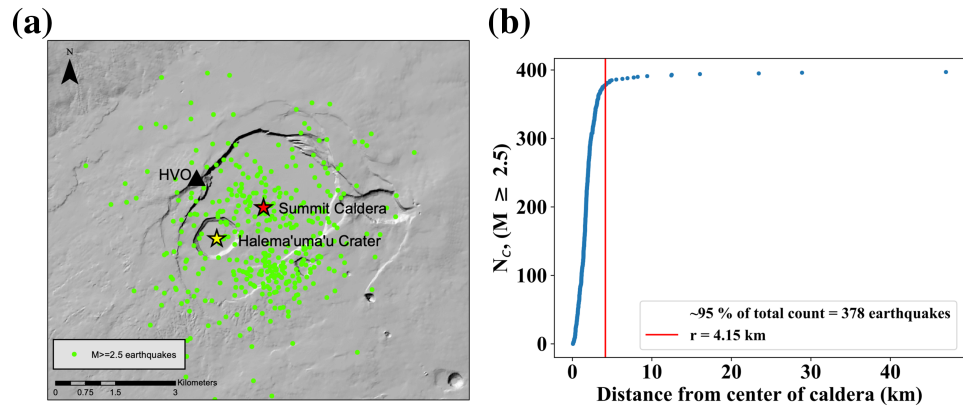
(a)   **(b)**

Figure 4. (a) The spatial distribution of the epicenters of $M \geq 2.5$ events that occurred in the interval between the summit seismic events of $t = 53.42$ and $t = 54.68$ days. The red and yellow stars indicate the centers of the summit caldera and Halema'uma'u Crater, respectively. (b) The cumulative number of these epicenters found at a radial distance from the center of the summit caldera (red star in (a)). We find that 378 earthquakes lie within a circle with radius $r = 4.15$ km. This represents 95% of all earthquakes on the Island during this period.

Although there was variable scatter in the data, some overall trends were clear. First, looking at the overall interevent time, Δt, a best fit line through the data reveals a very shallow positive slope. Although antipersistent, with values ranging from less than 1 day to just over 2 days, we consider the interevent times fairly constant throughout the sequence with only a small general increase (Figure 7a). The active time, t_a, showed an overall general increase throughout the sequence as well (Figure 7c). In contrast to these monotonic trends, the quiescent time, t_q had a significant shift in trend during the sequence around $t = 40$ days, 14 June. The quiescent time decreases for about the first 10 days of our study period before remaining relatively consistent for the rest of the sequence (Figure 7b). After the collapse event of 17 June, there was only one interevent time whose quiescent time was longer than its active time. The cumulative number of earthquakes, N_c, and the rate of seismicity during the active time, $\frac{dN_c}{dt}$, both had significant changes in trend at this early-middle June point in the sequence too. The cumulative number of earthquakes fluctuates around 100 for the first 10 days before increasing to variable but consistent rates fluctuating around 325 earthquakes per interevent time for the remainder of sequence (Figure 7d). The final variable analyzed was the rate of seismicity during the active time. These rates were remarkably linear with an average correlation coefficient of

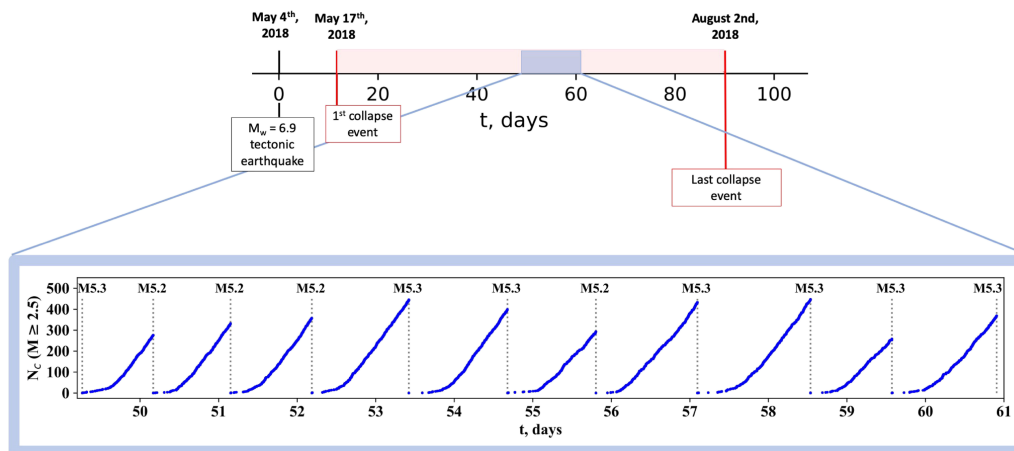**Figure 5.** A subset of the 46 interevent periods which illustrates the repetitive pattern of seismicity observed between the 47 large summit seismic events. The cumulative number N_c of $M \geq 2.5$ earthquakes is given as a function of time t. The vertical lines indicate the occurrence of a large collapse event and its magnitude is noted. The cumulative count of earthquakes resets to zero after each large event.
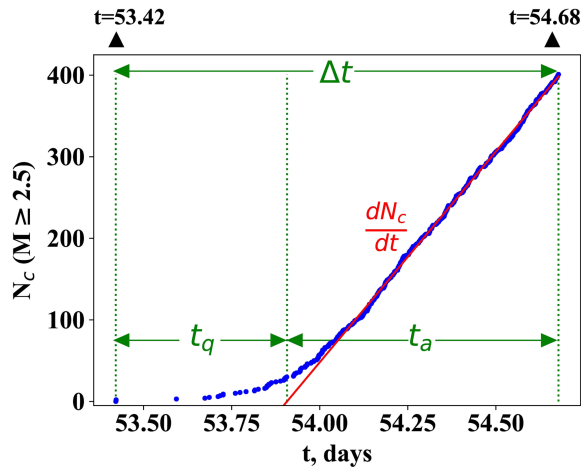
7

Figure 6. Annotated example of the seismicity during the interval between two typical collapse events (black triangles) at $t = 53.42$ and $t = 54.68$ days (interval used in Figures 4 and 7). The blue circles indicate the cumulative number, N_c, of $M \geq 2.5$ earthquakes as a function of time t. Time intervals of interevent time, quiescent time, and active time are shown in green as Δt, t_q, and t_a, respectively. The red line is the least squares fit to the data during the active time, and its slope, $\frac{dN_c}{dt}$, indicates the rate of seismicity.

0.9996. The rates were fairly low around 250 earthquakes per day, increasing slightly for the first 10 days before steeply increasing to over 500 earthquakes per day. After this jump in rate of seismicity, there was a gradual decrease in rates throughout the rest of the sequence as the rates fell back toward 250 earthquakes per day (Figure 7e). The rates were generally decreasing and returned to the level of seismicity before the jump in rates around 14 June. It is unclear if this is a coincidence or if it might be indicative of the physical system's behavior.

We note that the paper Shelly and Thelen (2019), published while this paper was under review, suggests that further work to improve the earthquake catalog is needed before analyzing magnitudes of events. We have included the b value analysis results that we had already completed and qualitatively contribute to our study. However, we caution the reader that these b values could change if further work on the earthquake catalog leads to significant changes in earthquake magnitudes. The Gutenberg-Richter scaling for our entire study period shown in Figure 2 shows that the b value ($b = 1.66$) is quite high compared with tectonic earthquakes in general (generally $b = 1$), but the fit of the data to the scaling is quite good. The larger b value is not atypical for volcanic settings where larger numbers of smaller earthquakes are often seen, especially during eruptive phases (Roberts et al., 2015). The Gutenberg-Richter scaling was applied to the seismicity of each interevent time. The average interevent b value was 1.67 with a minimum of 1.29 and a maximum of 2.06. There were no significant temporal trends observed in b values throughout the study period (Figure S1 in the supporting information).

Not only did the quiescent and active times behave differently in terms of rates of activity but also in magnitudes of activity. As seen in Figure 8, the quiescent times comprised smaller magnitude and fewer overall events in comparison to the active times. Even though the number of events was low, the Gutenberg-Richter scaling was applied to each interevent's quiescent time and active time. The average interevent b value for quiescent times was 2.04, and the average for active times was 1.65. The active time b values fluctuated similarly to the total interevent times between 1.23 and 2.23. As the majority of the earthquakes occurred in the active time, it makes sense that the b values of this time period are more closely aligned with the b values of the total interevent times (Figure S1). The quiescent time saw much more variation in b values ranging from 1.07 up to 3.43.

Although there were continually decreasing rates of seismicity during the active times as the sequence progressed, there was no clear signal indicative of the abrupt termination of this sequence. In early August, the active seismicity in the system as a whole appeared to cease. The last large collapse event occurred on 2

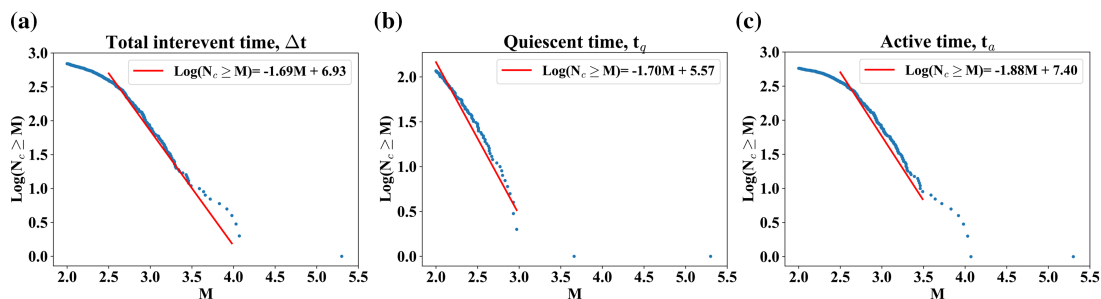**Figure 7.** These three plots are showing the frequency-magnitude statistics broken down for an example interevent period (period used in Figure 6). The red line shows the Gutenberg-Richter fit. The plots are interpreted the same as in Figure 2 but for specific spans of time: (a) events occurring during total interevent period, (b) events occurring during the quiescent time, and (c) events occurring during the active time.
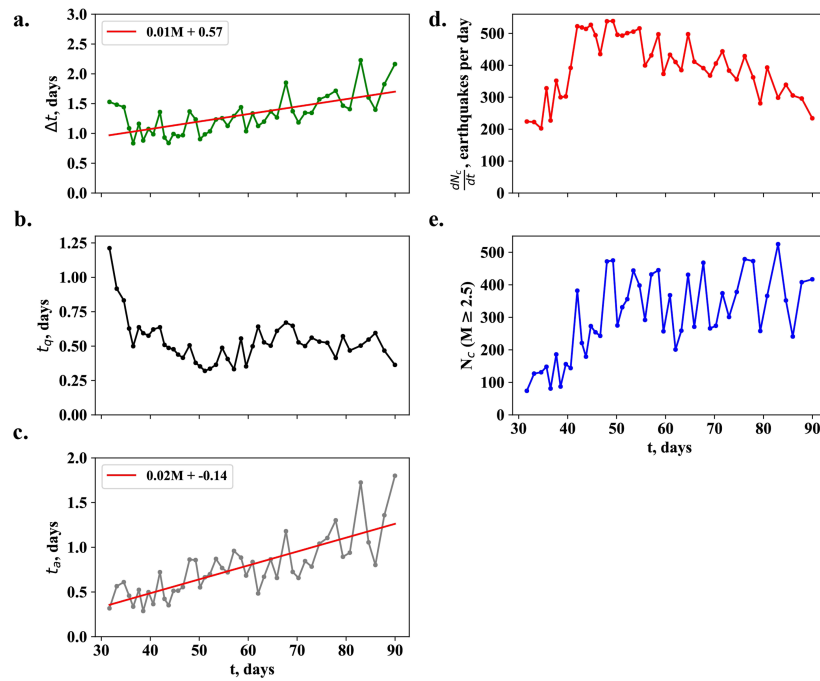
Figure 8. These plots show how the characteristics we studied changed throughout the study period. Panels (a–e) have the same *x* axis which is time, *t*, for the days of our study period. Each round marker represents 1 of the 46 interevent periods. The *y* axes are each a different variable of the interevent periods: (a) length of interevent time, (b) length of quiescent time, (c) length of active time, (d) rates of seismicity during the active times, and (e) cumulative number of earthquakes during the interevent time.

August. An initial quiescent period followed by an active period of constant seismicity typical of interevent times is seen. However, instead of culminating in another collapse event, the rate of seismicity simply decays (Figure 9).

5. Discussion

The type of analysis presented in this study could aid in improving our understanding of the Kīlauea volcanic system itself and caldera collapse of basaltic systems. The analysis reveals changes in activity that could be associated with changes to the physical system, which we discuss in the context of Kīlauea and other recorded caldera collapse events. Though they have been previously studied, the 2018 set of events provide
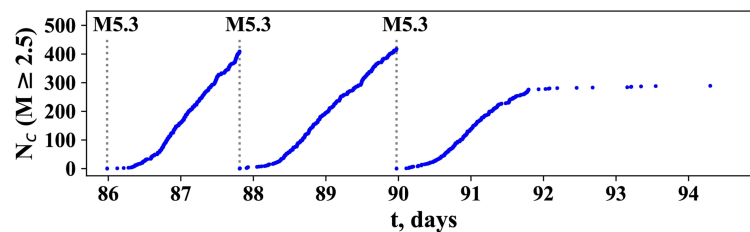
Figure 9. As in Figure 5, the cumulative number N_c of $M \geq 2.5$ earthquakes is given as a function of time *t*. The gray lines indicate the occurrence of a large collapse event and its magnitude noted. The cumulative count of earthquakes resets to zero after each large event. The final three collapse events are shown, and the far-right sequence of earthquakes shows the seismicity for 5 days following the last large seismic event that occurred on 2 August 2018 ($t = 89.97$).

9

opportunities to revisit the relationships within the system between the summit and the LERZ with modern instrumentation data as well as this recorded earthquake data and analysis.

The steady drainage of magma from Kīlauea's summit magma chamber from 2 May until 2 August 2018 was clearly connected to the sequence of collapse events including those that we study. Neal et al. (2019) estimated that over this period of time, the volume of collapse at the summit was 0.825 km^3. This value was similar to their estimates of erupted material in the LERZ during this time. The pattern of seismicity we observed is part of this complex process, but as a first approximation we suggest a periodic failure of the floor of the Halemaʻumaʻu Crater as also suggested by Neal et al. (2019) and following the piston model proposed in other caldera collapse events such as Miyakejima (Kumagai et al., 2001) and Bárdarbunga (Gudmundsson et al., 2016). At the start of the eruption, the crater floor was made up of solidified magma and rubble from the walls of the crater. After a collapse event, the floor of the crater rests on the top of the magma chamber. The floor has some strength and remains in place as magma withdrawal continues. The loss of magma reduces the basal support of the floor. The required support comes from the surrounding floor and walls of the summit caldera. As magma continues to be lost from the magma chamber and drains toward the LERZ, its support of the crater floor is reduced, but it is held in place by the transfer of stress to the surrounding rock in the caldera. As the stresses increase, small earthquakes begin to occur as illustrated in Figure 4 (during the quiescent time). The continued withdrawal of magma results in a further increase in stresses that reaches a critical point causing a transition to high levels of seismicity (the active time), until the lateral support of the floor fails. The collapse of walls and descent of the floor onto the lowered level of magma results in the collapse event and the release of seismic energy in the VLP events. The collapse event results in a further deposition of rubble from the walls of the crater onto the floor and an increase in the size and depth of the crater. The process then repeats in the observed episodic manner as magma is drained from the reservoir and moved downrift until the next collapse event occurs. The analysis of the interevent seismicity shows that the process of stress buildup is consistent and repeatable between collapse events.

Our focus at Kīlauea on precollapse and postcollapse conditions and breaking down the interevent seismicity into the quiescent and active times revealed some interesting characteristics of the seismicity, which could be related to the failure process leading to collapse. The decrease in duration of quiescent time after the first few pattern cycles indicates that the critical value of stress in the caldera floor and walls was reached in shorter amounts of time after a collapse event. The Gutenberg-Richter frequency-magnitude scaling results indicated that these shorter quiescent times had a higher relative number of smaller magnitude events to larger magnitude events (indicated by the overall higher b values; see Figure S1). Although the sample size was small because this was a time of quiescence, this was a fairly consistent characteristic. The larger magnitude events between collapse events occurred closer in time to the approaching collapse event, rather than to the previous collapse events as indicated by the lower b values calculated for the active times. After the large collapse events, time is needed again to reach the critical stress buildup needed for the larger earthquakes. The larger earthquakes happen as the floor is starting to reach failure, but this built-up stress still culminates in the collapse event. The built-up stresses are not large enough during the quiescent time to cause these mid- and larger magnitude interevent earthquakes. The mid-June changes in interevent seismicity statistics also seem to suggest a physical change in the collapse events. These changes could be related to changes in degrees of inflation and deflation, effusion volume and rates into the LERZ, magma supply from below, and/or geographic locations of fissures, which all have been studied as proxies for physical system changes during previous eruptions in Kīlauea and are discussed here. Some of these physical characteristics have been similarly utilized for collapse events elsewhere and are also discussed below.

The interpretation of the interevent seismicity presented above appeals to changes in magma supply and withdrawal which in turn affect the stress state of the caldera floor. Therefore, comparison to independent observation that constrains magma supply to and removal from the caldera would provide further support for this interpretation. As the inflation-deflation events were episodic with the collapse events, the degree to which the summit inflated and deflated (using tiltmeters) could be analyzed in a similar time series approach to look for significant changes during the sequence. For example, Epp et al. (1983) proposed an inverse relationship between Kīlauea's summit deformation, measured by tiltmeter, and the elevation of actively erupting fissures in the LERZ. They concluded that there was an increase in the amount the tilt changed with decreasing elevation of fissures. Similarly, Eaton and Murata (1960) discuss the interplay between erupted lava volumes, fissure location/elevation, and changes in tilt. Though much of the activity was

focused at Fissure 8, the 2018 events had a total of 24 active fissures in the LERZ (Neal et al., 2019). The geographic locations and durations of activity may correlate with not only the extent of tilt changes but also potentially the summit seismic activity such as that of the intercollapse times studied in this paper. As more lava output and effusion rate data become available, this could provide more insight into systematic changes that could correlate with (or not) the mid-June change in activity we see in the seismicity rates and quiescent time durations.

Previous caldera collapse studies have also focused on the pressure changes and relationships between the summit and rift zone eruptions as a way to approach collapse dynamics. The Bárdarbunga volcano in Iceland experienced caldera collapse from 2014–2015. Gudmundsson et al. (2016) studied this event using many data types including seismicity, GPS displacements, magma flow rates, and geobarometric and subaerial gas analysis. Through their analysis of these and modeling of the system, Gudmundsson et al. (2016) concluded that this collapse event was initiated by drainage of magma away from the summit and continued in stages as the product of a pressure feedback between the magma path flowing away from the summit and the block ("piston") on top of the summit magma chamber. In the past at Kīlauea, insight into the magma chamber pressure conditions has been interpreted using lava lake levels (Patrick et al., 2015). In the case of the 2018 events, the lava lake had drained extensively to depths that were no longer visible by the start of the large collapse events. Neal et al. (2019) reference tilt signals detected downrift in their suggestion that collapse events and pressure changes are linked through the summit magma plumbing system and the LERZ. As detailed tilt data come out and are analyzed, this could be examined with our seismicity analysis to further examine the piston model pressure feedback explanation that was presented for the Icelandic caldera collapse.

Other volcanoes with less instrumentation such as Miyakejima in Japan have also displayed VLP signals during caldera-forming events (Kumagai et al., 2001). In 2000, there were VLP seismic signals recorded once to twice a day for almost a month, but in contrast to the 2018 Kīlauea events, the magnitudes of the events were inconsistent (Kumagai et al., 2001). There were other obvious differences with the 2000 Miyakejima events such as the fact that the erupted materials only amounted to 1% of the collapse volume (Geshi et al., 2002), whereas the erupted volume of Kīlauea was estimated by Neal et al. (2019) to be close to the volume of collapse at the summit. There were earthquake "preswarms" before the VLP events as studied by Kobayashi et al. (2003). The four preswarms they studied though contained much fewer earthquakes than the interevent times observed at Kīlauea. If available, the full catalog of small seismic events throughout the sequence of VLP events may be able to be studied in a similar way to this paper to learn more about the Miyakejima event. Investigating this and other caldera-forming events, for which there is available seismic data, could lead to a better understanding of both the quasiperiodic and nonepisodic caldera-forming collapse sequences at active volcanoes.

Just as the beginning trigger of the 2018 sequence of events was described as enigmatic by Neal et al. (2019), the end of the sequence also is poorly understood. Although the rates of interevent seismicity were generally decreasing in the latter part of the sequence as discussed above, there was no diagnostic signal within this data set that indicated that the sequence was coming to an end or pause in activity. Further research into the characteristics of the smaller seismicity or other data types may provide insight into this abrupt end of heightened activity and this periodic sequence as a whole. Neal et al. (2019) do point out that in some correlation to the final collapse event occurring on 2 August, that by 4 August the subsidence at the summit mostly stopped as well as the LERZ effusion. These terminal dates, along with duration of the whole process, are not always correlated. As Michon et al. (2011) point out at Piton de la Fournaise, the collapse process only lasted 2 days, but the eruption continued on for about a month after. Michon et al. (2011) attribute these differences to underlying factors of the physical system, concluding that one of the main factors in changes to these trends at the three different systems that they studied (Piton de la Fournaise, Fernandina, and Miyakejima) was magma outflow rates. This detailed type of interevent study using eruption rates, tilt steps, and displacement measurements, among others, could be reapplied and revisited using the further broken down interevent times and the trends of these specific time intervals where available/possible.

6. Conclusions

We have presented an approach for statistical analysis of the interevent seismicity behavior occurring between volcanic summit caldera collapse events. In this approach, we isolate the quiescent and active

11

times to look at immediate precollapse and postcollapse seismic activity. For Kīlauea, we find that the statistical nature of the intercollapse seismicity is generally antipersistent with some overall trends and a significant change in behavior occurring during mid-June. During mid-June there were significant changes in the quiescent time lengths (decreased), the number of earthquakes during the interevent times (increased), and the rates of seismicity during the active times (increased). While it is inferred that these changes are related to a change in the physical state of the volcanic system, the exact nature of the change remains unknown.

The statistical behavior of the small magnitude seismicity, however, does provide an important data set that describes a very regular, repeatable process occurring between collapse events, which may also be sensitive to larger-scale changes linked to magma flow away from the summit region. Due to the very recent occurrence of the events, the utility of the analysis we have presented here may become more clear as new and ongoing data sets and studies are published, and new physical models for collapse events are explored that can more explicitly link changes in stress state to magma supply and collapse mechanics. New detailed studies on the modeling of the caldera collapse mechanics, the lava effusion behavior at the fissures, the East Rift Zone's feedback system with the summit, and magma sources and geochemistry have been published while this paper was in review and provide further context and insight to the Kīlauea system as a whole (e.g., Anderson et al., 2019; Gansecki et al., 2019; Patrick et al., 2019). An example of another recent intercollapse seismicity study on these events is Butler (2020), which analyzes the interevent seismicity as "foreshocks" of the collapse events. The low number of caldera collapse events that have occurred globally requires full exploration of each system's properties and characteristics in order to gain insight into the underlying physical processes within these volcanic systems as well as general process of caldera collapse.

Data

Maps were made using the National Map and National Elevation Dataset (NED) proved by the U.S. Geological Survey (https://www.usgs.gov/core-science-systems/ngp/tnm-delivery/). Earthquake data were acquired on 22 August 2018 from the U.S. Geological Survey Earthquake Catalog (https://earthquake.usgs.gov/earthquakes/search/). Magnitudes, epicenter locations, dates and times were all downloaded from USGS Earthquake Catalog. Analysis and figures done using Python 3.6.4. ArcGIS and QGIS were also used in making maps.

References

Anderson, K. R., Johanson, I. A., Patrick, M. R., Gu, M., Segall, P., Poland, M. P., et al. (2019). Magma reservoir failure and the onset of caldera collapse at Kīlauea Volcano in 2018. *Science*, *366*(6470), eaaz1822. https://doi.org/10.1126/science.aaz1822

Anderson, K. R., Poland, M. P., Johnson, J. H., & Miklius, A. (2015). Episodic deflation-inflation events at Kīlauea Volcano and implications for the shallow magma system. In *Hawaiian Volcanoes* (pp. 229–250). Washington, DC: American Geophysical Union. https://doi.org/10.1002/9781118872079.ch11

Butler, R. (2020). Volcanic earthquake foreshocks during the 2018 collapse of Kīlauea Caldera. *Geophysical Journal International*, *220*(1), 71–78. https://doi.org/10.1093/gji/ggz425

Cervelli, P., & Miklius, A. (2003). The shallow magmatic system of Kilauea Volcano. In *The Pu'u 'Ö'ö-Küpaianaha Eruption of Kīlauea Volcano, Hawai'i: The First 20 Years* (pp. 149–164). Reston, VA: U.S. Geological Survey.

Colella, H. V., & Dieterich, J. H. (2015). Analysis of seismicity rate changes and tilt during early episodic fountaining stage of Pu'u 'Ō'ō, Hawai'i, eruption. In *Hawaiian Volcanoes* (pp. 213–228). Washington, DC: American Geophysical Union. https://doi.org/10.1002/9781118872079.ch10

Eaton, J. P., & Murata, K. J. (1960). How volcanoes grow. *Science*, *132*(3432), 925–938. https://doi.org/10.1126/science.132.3432.925

Epp, D., Decker, R. W., & Okamura, A. T. (1983). Relation of summit deformation to East Rift Zone eruptions on Kilauea Volcano, Hawaii. *Geophysical Research Letters*, *10*(7), 493–496. https://doi.org/10.1029/GL010i007p00493

Filson, J., Simkin, T., & Leu, L. (1973). Seismicity of a caldera collapse: Galapagos Islands 1968. *Journal of Geophysical Research*, *78*(35), 8591–8622. https://doi.org/10.1029/JB078i035p08591

Francis, T. J. G. (1974). A new interpretation of the 1968 Fernandina caldera collapse and its implications for the mid-oceanic ridges. *Geophysical Journal International*, *39*(2), 301–318. https://doi.org/10.1111/j.1365-246X.1974.tb05456.x

Gansecki, C., Lee, R. L., Shea, T., Lundblad, S. P., Hon, K., & Parcheta, C. (2019). The tangled tale of Kīlauea's 2018 eruption as told by geochemical monitoring. *Science*, *366*(6470). https://doi.org/10.1126/science.aaz0147

Geshi, N., Shimano, T., Chiba, T., & Nakada, S. (2002). Caldera collapse during the 2000 eruption of Miyakejima Volcano, Japan. *Bulletin of Volcanology*, *64*(1), 55–68. https://doi.org/10.1007/s00445-001-0184-z

Gudmundsson, M. T., Jónsdóttir, K., Hooper, A., Holohan, E. P., Halldórsson, S. A., Ófeigsson, B. G., et al. (2016). Gradual caldera collapse at Bárdarbunga volcano, Iceland, regulated by lateral magma outflow. *Science*, *353*(6296), aaf8988–aaf8271. https://doi.org/10.1126/science.aaf8988

Gutenberg, B., & Richter, C. F. (1954). *Seismicity of the earth and associated phenomena* (2nd ed.). Princeton, NJ: Princeton University Press.

Heliker, C., & Mattox, T. (2003). The first two decades of teh Pu'u'O'o-Kupaianaha eruption: Chronology and selected bibliography. In *The Pu'u 'Ö'ö-Küpaianaha Eruption of Kīlauea Volcano, Hawai'i: The First 20 Years* (pp. 1–28). Reston, VA: U.S. Geological Survey.

12

Kobayashi, T., Ohminato, T., & Ida, Y. (2003). Earthquakes series preceding very long period seismic signals, observed during the 2000 Miyakejima volcanic activity. *Geophysical Research Letters*, *30*(8), 1423. https://doi.org/10.1029/2002GL016631

Kumagai, H., Ohminato, T., Nakano, M., Ooi, M., Kubo, A., Inoue, H., & Oikawa, J. (2001). Very-long-period seismic signals and caldera formation at Miyake Island, Japan. *Science*, *293*(5530), 687–690. https://doi.org/10.1126/science.1062136

Lacey, A., Ockendon, J. R., & Turcotte, D. L. (1981). On the geometrical form of volcanoes. *Earth and Planetary Science Letters*, *54*(1), 139–143. https://doi.org/10.1016/0012-821X(81)90074-1

Michon, L., Massin, F., Famin, V., Ferrazzini, V., & Roult, G. (2011). Basaltic calderas: Collapse dynamics, edifice deformation, and variations of magma withdrawal. *Journal of Geophysical Research*, *116*, 1–8. https://doi.org/10.1029/2010JB007636

Neal, C. A., Brantley, S. R., Antolik, L., Babb, J. L., Burgess, M., Calles, K., et al. (2019). The 2018 rift eruption and summit collapse of Kīlauea Volcano. *Science*, *363*(6425), 367–374. https://doi.org/10.1126/science.aav7046

Newman, W. I., Turcotte, D. L., & Malamud, B. D. (2012). Emergence of patterns in random processes. *Physical Review E*, *86*, 026103. https://doi.org/10.1103/PhysRevE.86.026103

Patrick, M. R., Anderson, K. R., Poland, M. P., Orr, T. R., & Swanson, D. A. (2015), Lava lake level as a gauge of magma reservoir pressure and eruptive hazard. *Geology*, *43*(9), 831–834. https://doi.org/10.1130/G36896.1

Patrick, M. R., Dietterich, H. R., Lyons, J. J., Diefenbach, A. K., Parcheta, C., Anderson, K. R., et al. (2019). Cyclic lava effusion during the 2018 eruption of Kīlauea Volcano. *Science*, *366*(6470). https://doi.org/10.1126/science.aay9070

Poland, M. P., Huth, T. E., & Miklius, A. (2009). Source processes of short-term, transient tilt events at Kilauea Volcano, Hawaii. *AGU Fall Meeting Abstracts*, V43G-2331.

Roberts, N. S., Bell, A. F., & Main, I. G. (2015). Are volcanic seismic b-values high, and if so when? *Journal of Volcanology and Geothermal Research*, *308*, 127–141. https://doi.org/10.1016/j.jvolgeores.2015.10.021

Shelly, D. R., & Thelen, W. A. (2019). Anatomy of a caldera collapse: Kīlauea 2018 Summit Seismicity Sequence in High Resolution. *Geophysical Research Letters*, *46*, 14,395–14,403. https://doi.org/10.1029/2019GL085636

Swanson, D. A., Duffield, W. A., Jackson, D. B., & Peterson, D. W. (1979). *Chronological narrative of the 1969-71 Mauna Ulu eruption of Kilauea Volcano, Hawaii* (USGS Numbered Series No. 1056. Reston, VA: United States Geological Survey. Retrieved from https://pubs.er.usgs.gov/publication/pp1056

Tilling, R.I., Heliker, C., & Swanson, D.A. (2010), *Eruptions of Hawaiian volcanoes: Past, Present, and Future* (General Information Product No. 117) (p. 63). Reston, VA: United States Geological Survey. Retrieved from https://pubs.usgs.gov/gip/117/

Turcotte, D. L. (1997). *Fractals and chaos in geology and geophysics* (2nd ed.). New York: Cambridge University Press.

Turcotte, D. L., & Schubert, G. (2014). *Geodynamics* (3rd ed.). New York: Cambridge University Press.

United States Geological Survey (USGS) (2018a). Earthquake catalog. Retrieved from https://earthquake.usgs.gov/earthquakes/search/

United States Geological Survey (USGS) (2018b). Volcano hazards program, Hawaiian Volcano Observatory. Retrieved from https://volcanoes.usgs.gov/vhp/archive_search.html

Wolfe, E. W., Garcia, M. O., Jackson, D. B., Koyanagi, R. Y., Neal, C. A., & Okamura, A. T. (1987). The Puu Oo eruption of Kilauea Volcano, Episodes 1-20, January 3, 1983, to June 8, 1984. In *Volcanism in Hawaii* (Vol. 1, pp. 471–508). Reston, VA: U.S. Geological Survey.

13

Chapter 2

Natural Time Analysis and Nowcasting of Quasi-Periodic Collapse Events During the 2018 Kīlauea Volcano Euruptive Sequence

2.1 Introduction of Published Manuscript 2

This chapter was published in Earth and Space Science, an American Geophysical Union (AGU) journal in 2022. See Appendix A for license to include in this thesis. The research in this first chapter was initially started with my advisor at the time, Louise Kellogg. The research problem initiated by Louise and I was more formally developed with collaboration with Donald Turcotte and John Rundle. Magali Billen provided helpful feedback on the this project after Louise's passing, especially with the writing and submission process of this manuscript.

Earth and Space Science

Author Contributions:

Investigation: Rebecca A. Fildes
Methodology: Rebecca A. Fildes, Donald L. Turcotte, John B. Rundle
Writing – original draft: Rebecca A. Fildes
Writing – review & editing: Rebecca A. Fildes, Donald L. Turcotte, John B. Rundle

Natural Time Analysis and Nowcasting of Quasi-Periodic Collapse Events During the 2018 Kīlauea Volcano Eruptive Sequence

Rebecca A. Fildes[1] , Donald L. Turcotte[1], and John B. Rundle[1,2]

[1]Department of Earth and Planetary Sciences, University of California, Davis, CA, USA, [2]Department of Physics, University of California, Davis, CA, USA

Abstract The period of heightened volcanic and seismic activity at Kīlauea volcano on the island of Hawai'i, USA from late spring through summer 2018 included a remarkable quasi-periodic sequence of caldera collapse events. From mid-May to early-August, 62 collapse events, each releasing the seismic energy equivalent of a M_w 5.0 ± 0.4 earthquake, occurred about every 1–2 days with over 300 $M \geq 2.5$ earthquakes between sequential collapses. This region, experiencing very high rates of seismicity and frequent large magnitude events, is a good candidate to apply a regional seismic hazard assessment. Nowcasting is a type of statistical analysis that uses small magnitude events to estimate the occurrence of large magnitude events. This is done utilizing the concept of natural time in which time is counted by small magnitude event occurrences between large magnitude events, not in clock time (days passed). This method has produced a "nowcasted" set of large earthquakes that are in good agreement with the actual cataloged events in prior studies analyzing non-volcanic regions. Previously applied to tectonic earthquakes and induced seismicity over longer time frames, this is the first test of nowcasting large caldera collapse events in volcanic associated seismicity and on a relatively short time scale. The technique produced limited "success" nowcasting 37 collapse events that agreed with the catalog of actual events. A temporal dependence of successful nowcasting during the sequence was found that may correlate to previously identified and analyzed physical changes in the volcanic system.

1. Introduction

1.1. Kīlauea Volcano

Kīlauea is the southeastern most volcano of the five volcanic systems comprising the island of Hawai'i in Hawaii, USA (Figure 1). It is also the youngest and recently the most active. The 2018 eruptive phase involved both summit caldera collapse and eruptions on the flanks of the volcano. It is considered the largest (and most damaging) eruption of Hawai'i's past 200 years (Anderson et al., 2019; Gansecki et al., 2019; Neal et al., 2019; Patrick, Dietterich, et al., 2019). The full timeline of events of the 2018 sequence is detailed in Neal et al. (2019): here we highlight the significant dates and events from their paper.

In early May 2018, the summit lava lake of Kīlauea began to drain and subsidence was observed around the summit. On 4 May there was a moment magnitude (M_w) 6.9 earthquake in the flank that they suggest helped open up a rift to make way for magma movement away from the summit reservoirs. Liu et al. (2018) also found that the thrust event rupture was on a shallowly dipping, weak fault and may have had important impacts on rifting during the early stages of eruption. The lava lake continued to drain until it was out of view while fissures in the lower East Rift Zone (LERZ) opened and erupted. Mid-magnitude seismicity began to increase at the summit in mid-May and ash explosions began.

Beginning in mid-May, very-long-period (VLP) seismic events were recorded within the summit caldera. The sources of VLP events are ascribed to changes in volume. From mid-May to early August a total of 62 VLP events were recorded at the summit. On 16 May, the first of these summit seismic events occurred as an ash explosion. Eleven more of these explosions/collapse events at the summit occurred between 16 May and 26 May producing a total of 12 events that each were assigned a M_w 4.9 ± 0.2. Subsidence within the caldera around Halema'uma'u Crater began at the end of May. From late May until 2 August, the latter 50 VLP events, each M_w 5.3 ± 0.1, were large collapses of the caldera floor with each resulting in a drop of several meters of the floor. The quasi-periodic
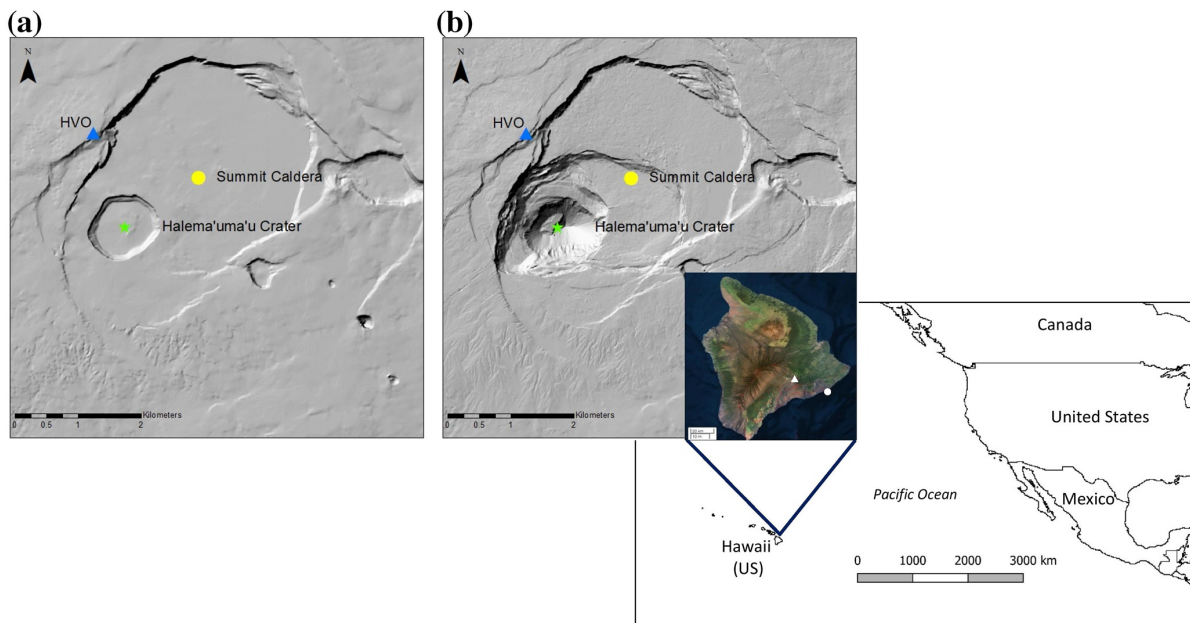
Figure 1. Shaded relief map showing the summit region of Kīlauea prior to the 2018 eruption (a) and then again partway through the 2018 eruption (b) (USGS, 2018). The yellow circle and the green star indicate the centers of the summit caldera and Halema'uma'u Crater, respectively, and the location of the Hawaiian Volcano Observatory is indicated by the blue triangle. Inset: The Island of Hawai'i with Kīlauea's summit (white triangle) and the epicenter of the 6.9 M_w mainshock (white circle). Also referenced is Hawaii's geographic location in the Pacific Ocean.

collapses of the caldera floor and walls were associated with the removal of magma from the summit magma chamber as it was transported down-rift to the fissures in the LERZ.

Several studies have produced specific models of the evolving collapse dynamics throughout the sequence (e.g., Anderson et al., 2019; Gansecki et al., 2019; Neal et al., 2019; Patrick, Dieterich, et al., 2019; Segall et al., 2019; Shelly & Thelen, 2019; Tepp et al., 2020). Periods of inflation were observed at the summit prior to a collapse event followed by deflation after a collapse event. This inflation-deflation pattern repeated itself between collapse events, accompanied by a pattern of smaller magnitude earthquakes. Following a collapse event there was a period of quiescence with very low seismic activity. This was followed by a large increase in rates of seismicity that occurred pre-collapse. Due to their pattern, Butler (2020) categorized these as foreshocks of collapse events, rather than aftershocks, and analyzed them as such. This pattern of post-collapse quiescence and pre-collapse increase in activity repeated itself between all of the collapse events (e.g., Anderson et al., 2019; Fildes et al., 2020; Shelly & Thelen, 2019; Tepp et al., 2020). Neal et al. (2019) reported that there were more than 700 earthquakes below magnitude 4.0 per day. The final collapse event occurred on 2 August and by 4 August they report that both subsidence at the summit and lava effusion in the LERZ had mainly ended.

1.2. Natural Time and Nowcasting

Nowcasting is considered an indirect way of assessing a system's current state (Rundle et al., 2016). It's basic concepts have evolved within the field of economics (e.g., Giannone et al., 2008) and has more recently been applied to assessing seismic hazard. Since it's initial development (Rundle et al., 2016), it has been applied in multiple locations in the United States of America as well as other seismically active locations around the globe (e.g., Donnellan et al., 2018; Luginbuhl, Rundle, Hawkins, & Turcotte, 2018; Luginbuhl et al., 2018a, 2018b, 2019; Pasari, 2019; Pasari & Mehta, 2018; Pasari & Sharma, 2020; Pasari et al., 2021; Rundle et al., 2018; Rundle et al., 2019; Rundle et al., 2020; Varotsos et al., 2017). In earthquake application, it has been developed as a statistical approach to use as an indirect way of gaining insight into the changing stress state and seismic hazard of a region in the time between large seismic events. Nowcasting is based on regional seismicity in an area and is not a single-fault based model. The technique utilizes the concept of "natural time", which replaces clock

16
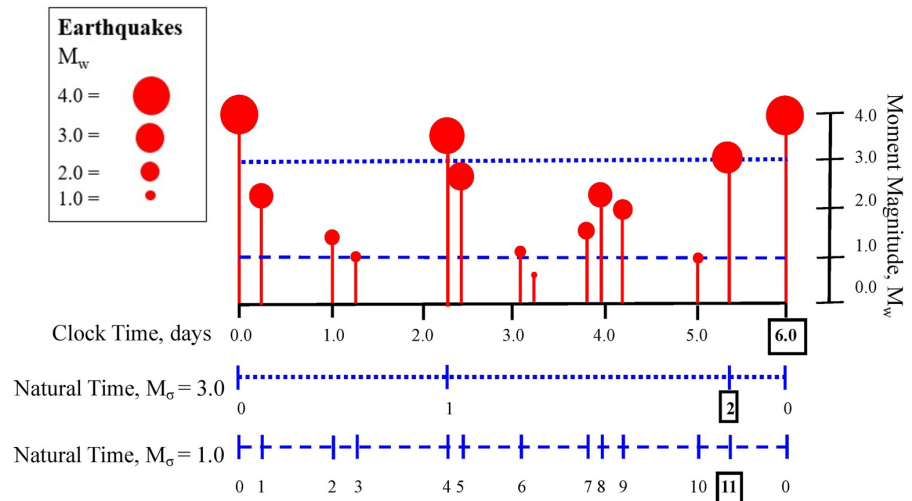
Figure 2. A timeline of earthquake occurrences illustrating the concept of natural time. Natural time is counted here as earthquakes that occur between $M_\lambda \geq 4.0$ events. The top dotted line uses $M_\sigma = 3.0$. The lower dashed line counts natural time using $M_\sigma = 1.0$. Each blue hatch mark on the timelines and number below it are counting natural time. Although the same clock time has passed (6.0 days), between two $M_\lambda = 4.0$ events, the natural time is different depending on the value chosen for M_σ. Notice natural time resets to zero after a M_λ event occurs.

time (days passed) as a way of tracking time between large magnitude events (Varotsos et al., 2002, 2005, 2011). In this way, nowcasting uses small magnitude events to estimate the occurrence of large magnitude events. The goal is computing a set of large magnitude events that temporally agree with observed large magnitude events (Rundle et al., 2016).

For set earthquake magnitudes M_σ and M_λ, natural time is an event-based count for which time is counted as the number of "small" magnitude earthquakes, $M_\sigma \leq M \leq M_\lambda$, that have occurred since the last large magnitude, $M \geq M_\lambda$, earthquake (Rundle et al., 2016) (Figure 2). Natural time counts are sensitive to the choice of M_σ and M_λ. For example, Figure 2 shows a timeline of seismicity over a 6-day long period where the large magnitude earthquake is chosen as $M_\lambda = 4.0$: if $M_\sigma = 3.0$ the natural time is 2, while if $M_\sigma = 1.0$ the natural time is 11. In order to get the best statistics, M_σ should be defined with the smallest magnitude possible within the catalog completeness so that the maximum number of events can be used to obtain a more complete view of the stress state (Luginbuhl et al., 2018). To assess for seismic hazard, M_λ should be chosen large enough for the seismic hazard of the region, but also as a value that occurs frequently enough over the chosen time scale that there are multiple earthquake cycles over which to nowcast (Luginbuhl et al., 2018).

Luginbuhl et al. (2018) state that the nowcasting method assumes that the seismicity being analyzed follows Gutenberg-Richter frequency magnitude scaling. This assumption will be referred to as the "GR Assumption." The Gutenberg-Richter scaling approximates the frequency-magnitude relationship for earthquakes (Gutenberg & Richter, 1954):

$$\log_{10}(N_c) = a - bM \tag{1}$$

Here M represents magnitude and N_c is the cumulative number of events with magnitude $\geq M$. The variable a measures seismic intensity and the value of b (referred to as the "b-value") is the variable that represents the scaling between the number of small events and large events (Gutenberg & Richter, 1954). This b-value is generally near one, but higher b-values have been measured in active volcanic settings where larger numbers of small magnitude events occur (Roberts et al., 2015). The Gutenberg-Richter scaling does not provide any information on time between events, but only the distribution of the sizes of events. Rundle et al. (2016) states that if the overall b-value is relatively constant, then the natural time analysis is independent of temporally varying seismicity levels. An advantage of using natural time is that it does not depend on a constant rate of seismicity and can be applied when seismic activity varies with time and deviates from background rates.

17

If the Gutenberg-Richter scaling is applicable for the earthquakes, then the natural time relationship of small magnitude events to large magnitude events can be derived from Equation 1. The Gutenberg-Richter frequency-magnitude scaling (Equation 1) can be re-arranged and written specifically for $N_{c\sigma}$, the cumulative number of small magnitude events:

$$N_{c\sigma} = 10^a 10^{-bM_\sigma} \tag{2}$$

and for $N_{c\lambda}$, the cumulative number of large magnitude events:

$$N_{c\lambda} = 10^a 10^{-bM_\lambda} \tag{3}$$

If you then divide Equation 3 by Equation 2 and rearrange, you can express the number of large events, $N_{c\lambda}$, in terms of the number of small magnitude events, $N_{c\sigma}$:

$$N_{c\lambda} = 10^{-b(M_\lambda - M_\sigma)} N_{c\sigma} \tag{4}$$

As defined, $N_{c\sigma}$ is natural time (it is counting small magnitude events), so this equation gives the natural time relationship that can be used to produce the nowcasted set of $N_{c\lambda}$. We use this equation in the Methods section to further outline and illustrate the full process of nowcasting.

The goal of the nowcast is to use the natural time relationship (Equation 4) to produce a set of M_λ earthquakes (a computed set of $N_{c\lambda}$) that are in temporal agreement with the actual cataloged M_λ events (the observed set of $N_{c\lambda}$). If successful, this would prove the utility of the method, which could then be used in the future to "nowcast" in real time when the next large event would occur in that region. However, there are certain limitations to this technique. First, the only data type that the nowcasting method utilizes is seismicity data and it is analyzed in a purely statistical manner. Second, although the technique utilizes natural time for the analysis, the outcome is a nowcasted set of events on a timeline, $N_{c\lambda}(t)$: therefore, these methods do not attempt to assign locations of large earthquakes but are instead focused on agreeing with temporal occurrences only. Additionally, as stated above, although it does not rely on constant levels of seismicity according to clock time, it does assume a relatively constant *b*-value over the time period of analysis (Rundle et al., 2016).

The nowcasting method as applied previously in tectonic and induced seismicity settings is tested here for the first time in an active volcanic eruption and caldera collapse sequence. This is also the first application of nowcasting on this short of time interval (data sets of days/months as opposed to years). The goal of this study is to test and evaluate the applicability and utility of nowcasting the seismic hazard of large caldera collapse events, using the 2018 Kīlauea Volcano eruptive sequence as a case study. The sequence of events at Kīlauea described above is a good candidate to which to apply a regional seismic hazard approach such as nowcasting. There were over 60 large magnitude seismic events over the course of about 90 days at the summit of Kīlauea. The collapse events occurred frequently with only about 1–2 days between them and are large enough events ($M \geq 4.7$) that there was infrastructure damage to roads as well as strong shaking observed at the summit park and Hawaii Volcano Observatory (Neal et al., 2019). There was also a significant amount of small seismicity between these events that can be utilized in natural time tracking. These swarms of summit seismicity between large collapse events are closely related to the accumulation of stress in the magma chamber roof and could then also be related to collapse events (Tepp, 2021). A regional seismic hazard approach such as nowcasting may also be advantageous in a rapidly changing environment such as this one where a single fault-based model would prove more difficult as subsidence, collapse, and rupture occurred on short timescales and drastically changed the summit structures.

2. Materials and Methods

2.1. Data Selection

The goal of this study is to test the application of the nowcasting technique to the caldera collapse events. Therefore, earthquakes that occurred between the first collapse event through the last collapse event on 2 August and whose epicenters are within a 5 km radius of the center of the caldera are selected for analysis. This spatial constraint removes all of the seismic activity that was occurring down rift associated with magma movement and the aftershock sequence of the 4 May M_w 6.9 earthquake. The earthquake data used for the analysis was accessed through the United States Geological Survey (USGS) Earthquake Catalog. All times presented in these methods
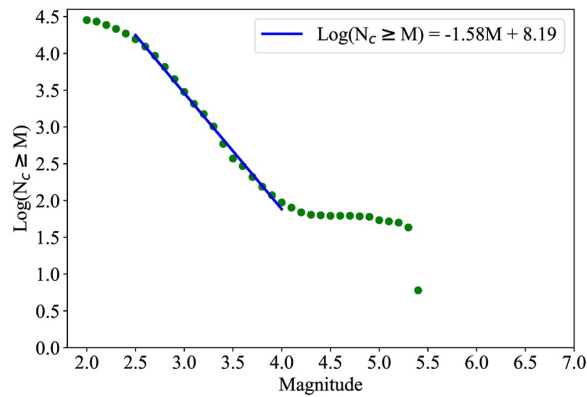
18

Figure 3. *Step 1* of the nowcasting methods is selecting the magnitudes for the nowcast using the fit of the Gutenberg-Richter relationship. The frequency-magnitude statistics of earthquakes from 17 May 2018–2 August 2018 within 5 km of the center of the summit caldera shows that the Gutenberg-Richter equations (Equation 1; blue line) provides a good fit to the data (green dots) for $M = 2.5$–4.0.

are Greenwich Mean Time (GMT). The methods below illustrate the analysis on this initial data set, later referred to as subcase S4.7a.

2.2. Nowcasting Caldera Collapse Events at Kīlauea

The natural time analysis and nowcasting methods carried out in this study follow the procedure outlined in Luginbuhl, Rundle, Hawkins, and Turcotte (2018). In order to test and evaluate the methods' broader applicability to a new subject area, no changes from those original methods are made. The general procedure follows:

1. *Select the magnitudes that will be used for M_σ and M_λ.*
2. *Determine the natural time relationship between M_σ and M_λ sized events.*
3. *Plot the M_σ as a function of clock time (days).*
4. *Calculate $N_{c\lambda}(t)$, the nowcasted set of M_λ events.*

Step 1.   Selecting magnitudes

Prior to carrying out a nowcast of a particular region and time, the values of M_λ and M_σ must be selected to define the nowcast objective and the magnitude of events that will be used in the natural time analysis. This is typically done using the fit of the Gutenberg-Richter scaling relationship to the earthquake data where M_λ is the largest magnitude event that can be fit with the relationship. As the purpose of this study is to evaluate the applicability of nowcasting for the caldera collapse events specifically though, $M_\lambda = 4.7$ is selected since this is the minimum magnitude of the large summit collapses (USGS Earthquake Catalog). This M_λ selection is based solely on the mechanism of earthquakes of this magnitude (events below M4.7 were not summit collapse events). This is unique in nowcasting because in this setting, the earthquakes being used to nowcast the collapse event are not the same type of event and the collapse events themselves, are not fit with the scaling relationship. The lack of strict Gutenberg-Richter scaling fit out to this magnitude will be discussed later. The value selected for M_σ should be as small as possible to include the maximum number of events, but still be within the catalog completeness level. The catalog completeness was estimated using the Gutenberg-Richter scaling relationship (Equation 1).

The data exhibit a prominent roll-off in the number of events for $M < 2.5$ compared to the Gutenberg-Richter fit to the data (Figure 3), supporting the conclusion that the catalog completeness of this data set is estimated to be $M = 2.5$ (Butler, 2020). The *b*-value determined using the linear least-squares fit of Equation 1 to the data in Figure 3, $b = 1.58$, is referred to as the "LS *b*-value." Another way to calculate the *b*-value, the "NT *b*-value", is to calculate it using Equation 4 (the natural time relationship) with the values chosen and calculated for M_λ, M_σ, $N_{c\lambda}$, and $N_{c\sigma}$, and solving for "*b*." In selecting $M_\sigma = 2.5$, events with $2.5 \leq M \leq 4.7$ are considered in the natural time counts. This results in 62 large magnitude events ($N_{c\lambda} = 62$), 13,990 small magnitude events ($N_{c\sigma} = 13,990$), and an NT *b*-value of 1.04. The difference between the LS *b*-value and the NT *b*-value, referred to here as the "Δ *b*-value", is calculated to be 0.54. The Δ *b*-value is indicative of how strictly the GR Assumption is followed or violated; a Δ *b*-value close to 0 would indicate a study where the GR Assumption is strictly followed and an increasing Δ *b*-value indicates increasing violation of the GR Assumption. In previous studies the Δ *b*-value was found to be close to 0, indicating to them that the natural time relationship was accurate (e.g., Luginbuhl, Rundle, Hawkins, and Turcotte 2018). The Δ *b*-value discrepancy in this study will be addressed in the Discussion section later. The maximum likelihood estimation method is also used to calculate the *b*-value, but qualitatively does not change the results of the study (Table S1 in Supporting Information S1). For consistency and comparison with prior nowcasting studies where linear least-squares was used to calculate *b*-values, these values are presented in the main paper.

Step 2.   Determining the natural time relationship

Once M_σ and M_λ are selected, the natural time relationship between them is calculated. The cumulative number of large magnitude events, $N_{c\lambda}$, is plotted as a function of the cumulative number of small magnitude events, $N_{c\sigma}$ (Figure 4a). A linear least squares regression that intercepts the origin is fit to the data:
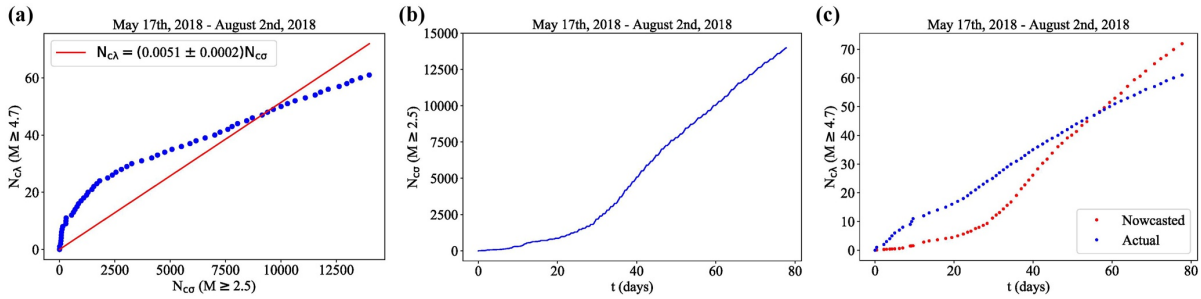
19

Figure 4. Methods for carrying out *Steps 2–4* of the nowcasting method. (a) *Step 2*: Cumulative number of large magnitude events, $N_{c\lambda}$, as a function of the cumulative number of small magnitude events, $N_{c\sigma}$ (blue dots). The red line is a least squares regression fit through the origin and the equation of this line represents the natural time relationship. (b) *Step 3*: the cumulative number of small magnitude events, $N_{c\sigma}$, as a function of clock time (days). (c) *Step 4*: the cumulative number of large magnitude events (collapse events), $N_{c\lambda}$, plotted as a function of clock time (blue dots). The red line is the nowcasted set of collapse events produced by multiplying the $N_{c\sigma}(t)$ plotted in *Step 3*, by the slope of the line calculated in *Step 2*. This plot is produced using the natural time relationship but then plotting the result in clock time for easier understanding and utilization.

$$N_{c\lambda} = 0.0051 N_{c\sigma} \tag{5}$$

This relationship refers back to Equation 4, where the term $10^{-b(M_\lambda - M_\sigma)}$ is the slope of that fit line, in this case 0.0051, and represents the natural time relationship. It is clear in Figure 4a that the relationship between the two data sets is non-linear, but as stated above the analysis is carried out without adjustments to the original methods to ensure consistency.

Step 3.   Small Magnitude Events Clock Time Relationship

Figure 4b shows $N_{c\sigma}(t)$. These are the values of $N_{c\sigma}$ plotted in Step 2, but now plotted as a function of clock time, t. Clock time is presented in days passed since $t = 0$, which is set at the occurrence of the first collapse event. This simple plotting step is an intermediary between visualizing in natural time (*Step 2*) and clock time (*Step 4*).

Step 4.   Calculating the nowcasted set of events

The final step in the process is using the calculated natural time relationship (Equation 5) to nowcast the $M_\lambda \geq 4.7$ collapse events. Figure 4c shows the actual recorded collapse events (blue dots) plotted as a function of clock time. The red dots in Figure 4c are the nowcasted set of collapse events produced by multiplying the values of $N_{c\sigma}(t)$ (plotted in Figure 4b) by 0.0051 (the slope of Equation 5), to give $N_{c\lambda}(t)$ (Equation 6).

$$N_{c\lambda}(t) = 0.0051 N_{c\sigma}(t) \tag{6}$$

The nowcast is produced using the natural time relationship, but plotted in terms of clock time for easier understanding and illustration. There is not good agreement between the nowcasted set of events and the actual recorded set of events as the red and blue dots deviate quite a lot from each other (Figure 4c). The cause of this deviation will be explored in the Results and Discussion sections.

In order to quantify the fit of the nowcasted events to the observed events, a root-mean-square deviation (RMSD) is calculated:

$$\text{RMSD} = \sqrt{\frac{\sum_{n=1}^{N} (\text{Model}_n - \text{Observed}_n)^2}{N}} \tag{7}$$

The RMSD quantifies how well a model fits an observed data set using the measured residuals between values of the two sets. A perfect model that exactly fits the observed data would have an RMSD value of 0, as there would be no residuals between the modeled points and the observed points. Therefore, a lower RMSD indicates a more well-fit model. The resulting data set plotted in Step 4 (Figure 4c) is turned into a cumulative distribution function (CDF) to normalize the counts of large earthquakes to be fractions of 1.00 (Figure 5). This will be necessary when comparing results of nowcasting cases with varying numbers of M_λ events. Then, the RMSD value is
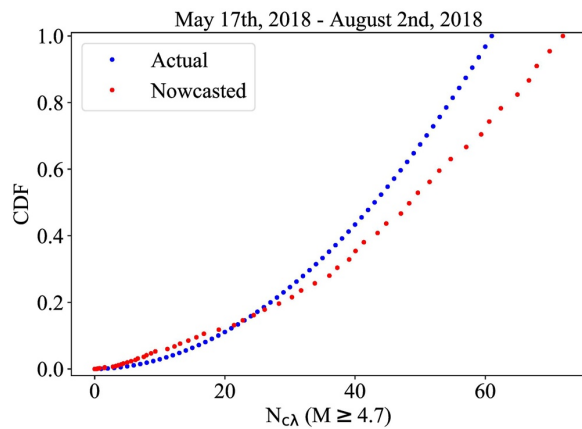
20

Figure 5. Cumulative distribution function of cumulative number of large magnitude events for observed and nowcasted events of subcase S4.7a. Colors are the same as Figure 4c.

calculated between the CDF of the observed earthquakes and the CDF of the nowcasted earthquakes, found here to be 0.101.

2.3. Multiple Case Studies of Nowcasting at Kīlauea

The initial application of the technique to the entire set of caldera collapse events did not produce a nowcasted set of events that agree with the actual recorded events (Figure 4c). To explore possible explanations the spatial, magnitude, and temporal constraints were varied across four cases. First, the spatial constraints are expanded to the whole island of Hawai'i to test if there was a significant part of the stress state missing by initially excluding the rift zone seismicity. Second, the magnitude constraints are also adjusted to $M_\lambda = 3.5$ to test the effect of violating and abiding by the GR Assumption.

- <u>Case S4.7</u>: Seismicity within 5 km of the summit caldera is used to nowcast $M_\lambda = 4.7$ events.
- <u>Case I4.7</u>: Seismicity from the whole island of Hawai'i is used to nowcast $M_\lambda = 4.7$ events.
- <u>Case S3.5</u>: Seismicity within 5 km of the summit caldera is used to nowcast $M_\lambda = 3.5$ events.
- <u>Case I3.5</u>: Seismicity from the whole island of Hawai'i is used to nowcast $M_\lambda = 3.5$ events.

where "S" indicates summit, "I" indicates the entire island, and the number indicates the value used for M_λ.

The volcanic system and structure also evolved as the sequence progressed. Therefore, to explore if the system's temporal evolution additionally affected the nowcasting results, Cases S4.7–I3.5 are each carried out over three different time-windows (indicated by the number 1, 2, and 3):

1. 17 May–2 August
2. 29 May–2 August
3. 14 June–2 August

These three time periods correspond to times when other observations indicate a change in the eruption sequence, which could correspond to changes in the stress state. Tepp et al. (2020) breaks the caldera collapse sequence into different phases that distinguish the shifts in behavior as the piston mechanism developed. The first collapse event on 17 May is proposed to be the start of a phase of decoupling of the magma reservoir and the roof of the magma chamber (the floor of the caldera). This phase encapsulates the first 12 collapse events, which were all explosive events. In late May, they identify the start of a new phase of activity as the collapse events become less explosive and the ring faults become more well developed. In early June, they propose that the final phase of the eruption begins when the ring fault reactivation and formation is terminated by the full development of the piston. They propose that for the rest of the sequence the piston continues to drop with the collapses in a more consistent behavior until it eventually slows down to the end of the sequence and final collapse event on 2 August. Therefore, subcases a, b, and c are chosen to have increasing delays in start time, aligning with these phases, but always end with the last collapse event. The details of the 12 subcases are summarized in Table 1. For comparison to case S4.7a, an unsuccessful case, the methods for case S4.7c, a successful case, are shown above in Figure 6. Note the linear natural time relationship (Figure 6a) in comparison to the nonlinear natural time relationship found in case S4.7a (Figure 4a).

3. Results

The results for the full analysis for all 12 subcases are provided in Figure 7 and the quantified results are summarized in Table 1 and Figure 8. A common occurrence across most of the subcases is that by the end of each respective timeline, the nowcast over-calculates the cumulative number of large events, despite under-calculating the number earlier in the timelines. There are some subcases that produce more successful nowcasts than others.

Table 1
This is a Summary Table of the Subcases Shown in Figure 6

Case #	subcase	Mags	Spatial	Temporal	Slope of natural time relation	NT b-value*	LS b-value +	Δ b-value	RMSD of CDF
S4.7	a	$M_\sigma = 2.5$ $M_\lambda = 4.7$	5 km radius of summit caldera	May 17 – August 2	0.0051	1.04	1.58	0.54	0.101
	b			May 29 – August 2	0.0040	1.09	1.60	0.51	0.057
	c			June 14 – August 2	0.0030	1.15	1.65	0.50	0.002
I4.7	a		Island of Hawai'i	May 17 – August 2	0.0048	1.05	1.58	0.53	0.094
	b			May 29 – August 2	0.0038	1.10	1.61	0.51	0.054
	c			June 14 – August 2	0.0028	1.16	1.65	0.49	0.002
S3.5	a	$M_\sigma = 2.5$ $M_\lambda = 3.5$	5 km radius of summit caldera	May 17 – August 2	0.0263	1.58	1.58	0.00	0.020
	b			May 29 – August 2	0.0263	1.58	1.60	0.02	0.023
	c			June 14 – August 2	0.0240	1.62	1.65	0.03	0.012
I3.5	a		Island of Hawai'i	May 17 – August 2	0.0261	1.58	1.58	0.00	0.021
	b			May 29 – August 2	0.0258	1.59	1.61	0.02	0.022
	c			June 14 – August 2	0.0237	1.63	1.65	0.02	0.014

Note. The column of NT *b*-value comes from the methods in the text using Equation 4 and the value in the "Slope of natural time relation" found during *Step 2* of the methods. The column of LS *b*-value comes from the methods in the text of applying GR relationship (Equation 1). The "Δ *b*-value Column" is the difference between the latter and former *b*-values for each subcase to illustrate the discrepancies in values arising from calculating the *b*-values in the two different ways. The RMSD of CDF values are how the success of nowcasting between subcases was quantified. See text for details. *Calculated from the Equation 4, slope of Natural Time figure value listed: $b = \log_{10}(\text{slope})/(M_\sigma - M_\lambda)$. +Linear least-squares fit of Gutenberg-Richter equation to binned magnitudes. Δ *b*-value = | "LS *b*-value" − "NT *b*-value."

Figure 8 summarizes these results by comparing the nowcasting fit to the data (RMSD of the CDF) with how well the GR Assumption was met (Δ *b*-values). The black star indicates where a case would plot if the nowcast fit the observed data perfectly and the GR Assumption was strictly followed. Cases S4.7 and I4.7 plot nearly identically to each other, as do Cases S3.5 and I3.5, indicating little to no spatial dependence of the method. For Cases S4.7 and I4.7 ($M_\lambda = 4.7$), there is a strong temporal dependence (subcases a, b, c) of nowcasting success, but not of Δ *b*-values. Collapse events are successfully nowcast for the latter portion of the eruption sequence, despite still violating the GR Assumption. In contrast, Cases S3.5 and I3.5 ($M_\lambda = 3.5$) show a negligible temporal dependence, but are overall better nowcasts relative to S4.7 and I4.7.
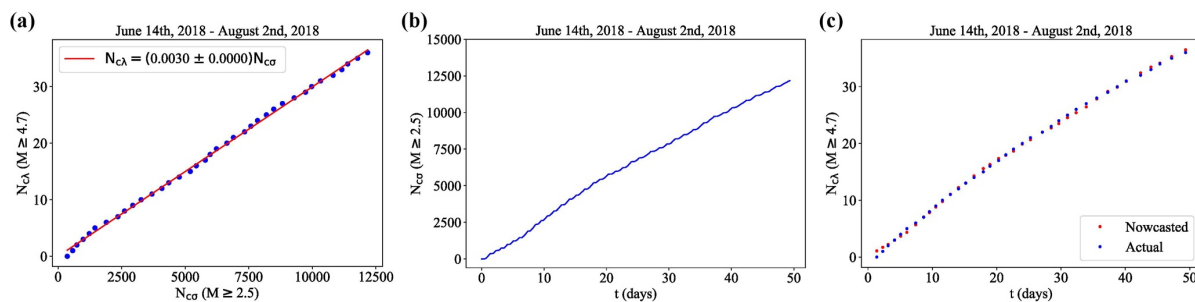
Figure 6. Nowcasting method for Subcase S4.7c. See Figure 4 for explanation. Note the improved agreement between the actual and nowcasted events.

22
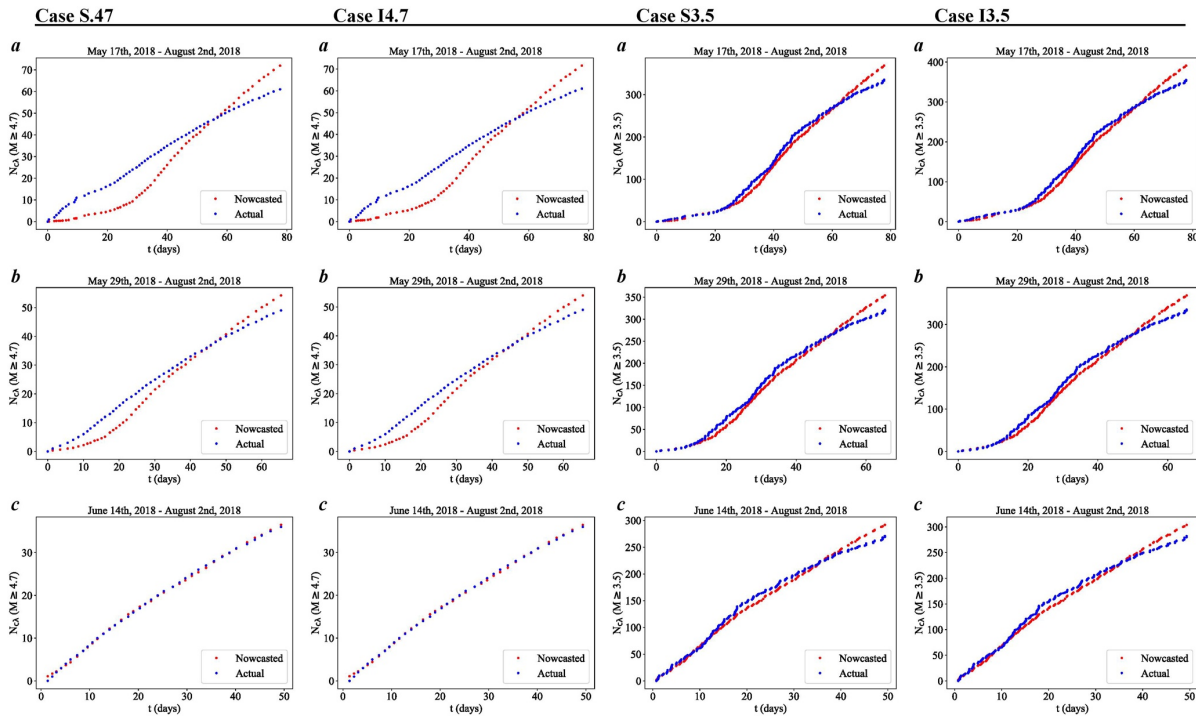
Figure 7. The nowcasting results for 12 test subcases using varying temporal, spatial, and magnitude constraints. Each of the 12 plots is to be read the same as Figure 4c. Each column (Case S4.7, Case I4.7, Case S3.5, and Case I3.5) represents a different combination of spatial and magnitude constraints. Each row represents the same time period over which the nowcast was done. Within a column, the nowcasts have the same magnitude and spatial constraints. Within a row, the nowcasts have the same temporal constraints. See both text and Table 1 for subcase descriptions.

Broadly, the trend of Δ b-values and RMSD values is found to be positively correlated as expected (Figure 8). For Cases S4.7 and I4.7, moving from subcases a to b to c, the RMSD value is decreasing and the Δ b-value is also slightly decreasing. The highest RMSD values belong to subcases S4.7a and I4.7a and these are the two subcases with the highest Δ b-values as well. However, there are some specific examples that contradict the expected positive correlation of RMSD values and Δ b-values. The overall lowest Δ b-values are found for S3.5a and I3.5a, but they do not have the lowest RMSD values. The lowest RMSD values belong to subcases S4.7c and I4.7c whose nowcasts align best with observed earthquakes, despite not having the lowest Δ b-values.
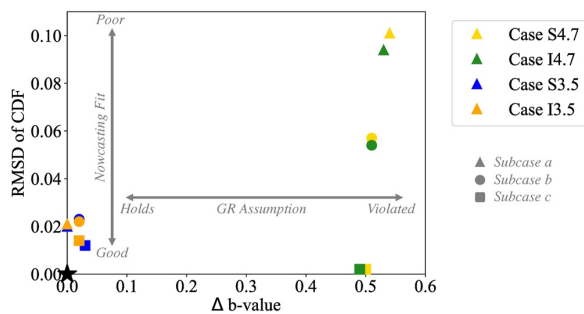
Figure 8. Distribution of nowcasting success results and Gutenberg-Richter (GR) Assumption compliance for the 12 subcases. The root-mean-square deviation of the cumulative distribution function of each subcase is plotted as a function of the Δ b-values. The black star indicates where a case would plot if the nowcast fit the observed data perfectly and if the GR Assumption was strictly followed.

4. Discussion

The original goal of this study was to use natural time to nowcast the full sequence of caldera collapse events at Kīlauea during the 2018 sequence: this goal was not met. However, the extended analysis conducted provides insight into the conditions and assumptions of the method. For the 12 subcases presented, some trials produce nowcasts in general agreement with actual recorded events, but many do not. Evaluating which case trials are successful together with other observations of the caldera collapse sequence provides more insight into when the nowcasting method may be applied in volcanic settings.

23

4.1. Challenges of Nowcasting an Active Volcanic Sequence

4.1.1. A Rapidly Evolving System

For cases focused on the later part of the collapse sequence (e.g., subcase S4.7c), the observed shift to a more linear natural time relationship (Figure 6a) and improved nowcasting of collapse events might be explained by a shift to a more consistent driving mechanism behind the stress state in the volcanic system. As discussed in Section 2.3, there were notable changes in the system during the eruption. Early in the sequence, caldera deformation was dominated by "down warping" and only a very small section of Halema'uma'u crater was collapsing (Shelly & Thelen, 2019). Shelly and Thelen (2019) detail that only after May, were larger fault structures around the caldera coherent and playing a role in the larger piston model generally used to describe caldera collapse events (e.g., Kumagai et al., 2001; Tepp et al., 2020). Segall et al. (2019) also note that the summit fault system was more established in late June and July and that the GPS signals indicated that pre-collapse inflation and post-collapse deflation became nearly equal such that they "canceled" each other out. These changes in physical structures and behavior suggest that the system was in a transitory stage early on, which then evolved into a more stable configuration (and stress state) as the fault system evolved to better accommodate the inflation-deflation process.

It is noteworthy that subcases analyzing activity starting in mid-June (S4.7c and I4.7c) exhibit the strongest agreement between the actual and nowcasted collapse events (Figures 7 and 8). This is significant because for this later phase of the eruption the natural time relationship had become linear (Figure 6a) even though the largest magnitude events used in these cases still do not follow the GR Assumption (Figure 8). This mid-June shift also corresponds to changes in small magnitude earthquake activity statistics including changes in the rates of seismicity preceding a collapse event, the length of seismic quiescence following collapse events, and the total number of earthquakes between collapse events (Fildes et al., 2020). These changes, and the ones identified in this present study, suggest that this later phase of the eruption represents a more stable, less transitory phase (i.e., stress state) of the eruption, which is also therefore better suited to the underlying assumptions of the nowcasting method. The general timing of this later phase of the eruption corresponds to when the piston and the ring fault structures became well-established. These results suggest that once the eruption reaches this more stable stress state, then a successful nowcast can be made even if the GR Assumption is not fully met. However, the poor nowcasting results for cases that include the earlier phases of the eruption (e.g., S4.7a and I4.7a) suggest that the continuous changes in the system limits the use of nowcasting early on in the eruption sequence. This poses a challenge for nowcasting similar caldera collapse events in real time, because it is difficult to decide when the system has stabilized enough for the method to be applied. This may limit the application of nowcasting caldera collapse sequences unless other data are available to identify when the system's underlying driving mechanism becomes more stable.

Although this study was focused on a relatively short-time scale during an active caldera collapse sequence, others have focused on longer-timescales for estimating hazard related to Kīlauea caldera collapses. Llenos and Michael (2022) used the probability distributions of recorded caldera collapse earthquakes from the last 114 years at Kīlauea to estimate their occurrence over the next 50 years. The results of their seismic hazard study was added into the Hawai'i National Seismic Hazard Model, updated in 2021 (Petersen et al., 2021). Expanding the nowcasting data set to the longer eruptive history of Kīlauea is a potential future direction to explore in seismic hazard assessment.

4.1.2. An Interconnected System?

An underlying assumption of the nowcasting method is that natural time provides a statistical measure of the state of the stress in a system. For this reason, how we define the system spatially is important; if the spatial extent of the study is too small a part of the full stress state will not be captured. Multiple studies have explored the connection in activity between Kīlauea's rift zones and summit (e.g., Anderson et al., 2015; Cervelli & Miklius, 2003; Eaton & Murata, 1960; Rowe et al., 2015; Swanson et al., 1976). More recently, the hydraulic-like connection of the East Rift Zone (ERZ) to the summit, has been confirmed with observing changes in either region influencing the other (Patrick, Dietterich et al., 2019; Patrick, Orr et al., 2019). The choice of spatial extent for the nowcasting analysis was tested in Cases I4.7 and I3.5 by expanding the study region from within 5 km of the summit caldera out to include the ERZ seismicity. However, there was no significant difference between the results for the smaller and larger analyzed regions (Figures 6 and 8). This is because although there was seismicity in the ERZ

24

associated with magma transport and the aftershock sequence of the 4 May M_w 6.9 event, most of this seismicity was below the lower magnitude cut-off of 2.5 (USGS Earthquake Catalog, 2019). Therefore, while other studies and observations show a clear connection between the ERZ and the summit, in terms of seismicity (within our magnitude threshold), analyzing only the summit region appears to sufficiently capture the stress state related to the caldera collapse events.

4.2. Comparison With Previous Nowcasting Studies

4.2.1. Geologic Setting

In the current nowcasting method, never applied to an active volcanic setting before, the linearity of natural time is expected from the Gutenberg-Richter relationship as evident in the methods. The violation and abidance of the GR Assumption in this study and its significance is discussed in the next section. The initial analysis in this study reveals a nonlinear natural time relationship (Figure 4a) which had not been dealt with in prior studies nor is accounted for in the existing nowcasting method. Previous nowcasting studies illustrate that a linear natural time relationship does not require a linear clock time behavior: natural time does not rely on constant levels of seismicity. One such previous study, focused on nowcasting induced seismicity, studies earthquakes with a nonlinear clock time behavior, but still finds linear natural time relationships (Luginbuhl, Rundle, Hawkins, and Turcotte, 2018). Not only does this study differ from ours in the linearity of the natural time relationship found, but the induced seismicity systems differ in terms of the mechanics driving the system. That study focuses on earthquakes associated with fluid injection and general tectonic stresses in the Geysers geothermal area of California and in Oklahoma. During their approximately 5-year study periods of each location the physical systems were generally consistent with no major changes in structural setting or drivers of the system noted.

In contrast, the analysis done here is focused on a dynamic volcanic system with changes in mechanisms and potential drivers behind the earthquake system. In our study, the hypothesized reason for the temporal dependence of nowcasting success found in this study is not that the clock time occurrences of collapse events became more linear. Instead, we interpret that the physical setting and underlying mechanisms and process (the piston and fault structure) became more consistent later in the sequence, and this in turn leads to a more linear natural time relationship, and therefore improved nowcasts.

If nowcasting is to be done on a sequence like these caldera collapse events, adjustments to account for the nonlinear natural time relationships may need to be developed. It is unclear though from this single study if and what adjustments should be made to the existing nowcasting model for volcanic seismicity. Further studies beyond this approximately 90-day sequence are needed to determine if the nonlinear natural time relationship is characteristic of these types of eruption events in general, or if it is unique to when the caldera collapse style changes mid-sequence as it did in 2018 at Kīlauea.

4.2.2. GR Assumption and *b*-Value Consistency

Not only is this the first test of nowcasting in a volcanic setting, but it also tests how strictly the GR Assumption needs to be followed in order to produce a successful nowcast. The linearity of natural time discussed above was hypothesized to vary with the varying abidance of the GR Assumption. In previous applications of nowcasting the GR Assumption was followed and both M_σ and M_λ plotted on the Gutenberg-Richter relationship fit to their data (Luginbuhl, Rundle, Hawkins, and Turcotte, 2018; Luginbuhl et al., 2018b). In this study, the RMSD values do indicate overall success of nowcasting when the GR Assumption holds, as expected (Figure 8). Unexpectedly, the RMSD values of the subcases violating the GR Assumption had a large range of nowcasting success, with two subcases even having the lowest RMSD values of all the cases (Figure 8). This raises questions about how strictly the GR Assumption needs to be followed. The linearity of natural time discussed is expected to vary with the varying abidance of the GR Assumption. Although case S4.7c demonstrates very linear natural time, it still has a high Δ *b*-value and violates the GR Assumption. As the natural time relationship (Equation 4) is derived directly from the Gutenberg-Richter relationship, it is very unclear as to why a case such as S4.7c, which violates the GR Assumption, would have such a linear natural time relationship.

The final assumption of the method to be addressed is that *b*-values are constant through time during the study period. This assumption is followed in all of the test cases as evident through the LS *b*-values only varying by ≤ 0.7 between subcases a, b, c of each case (Table 1). However, there is not a constant success level of nowcasting.

25

These conflicting results again require further investigation to better understand the assumptions conditions, such as the level of consistency of the b-values over time. One hypothesis is that there may be a minimum number of observed cycles of M_λ needed to calculate a relatively constant b-value. This sequence studied here was highly active compared to the background seismicity in the Kīlauea region as these events occur infrequently in recorded history. More observations of these cycles and sequences could lead to a better understanding of the dynamic sequence and the consistency or inconsistency of the frequency-magnitude distribution of events. Another possible explanation could be that the LS b-values need to vary by even less than they do here and there is a lower threshold for the Δ b-values.

The conflicting results of testing both of these assumptions may also be attributed back to the earlier discussion of the physical mechanisms and system drivers changing throughout the sequence and require further investigation. One such investigation, of an active system like Kīlauea, for example, could explore the changes in entropy of the system. The fluctuations in entropy have been used to identify when a system is approaching a dynamic phase change (e.g., Varotsos et al., 2021 and references therein). This has been applied, for example, in estimating the occurrence time of the 2011 M_w 9 Tōhoku earthquake in Japan (Varotsos, Sarlis, et al., 2020; Varotsos, Skordas, et al., 2020).

5. Conclusions

The original goal of this study was to evaluate the applicability of nowcasting to the seismic hazard of large caldera collapse events: Can the small magnitude earthquakes be used to estimate the occurrence of the next caldera collapse? This test produces poor results. The assumptions of the original nowcasting method are revisited through 12 subcases that vary the spatial, magnitude, and temporal constraints. In its current form, nowcasting is not a useful hazard assessment technique that could be utilized in this setting. Even though it shows success in nowcasting the collapse events later in the sequence, there was no distinctive single event that would've indicated a "good" start time for the analysis as the sequence was unfolding. We interpret this is to be due to the fact that for volcanic activity of this type, the intermittent nature of the magmatic forcing leads to transients that are not consistent with the underlying assumptions. In contrast, application of the method to tectonic earthquakes assumes that the underlying plate tectonic forcing is essentially "steady state" due to the ongoing plate motions.

In this application, the utility of the technique is stronger for identifying the changes in natural time relationships and therefore the system. It is significant that there is the above-described change in the success of nowcasting with time, and therefore a change in the natural time relationship. These changes correlate temporally with the changes in small seismicity behavior analyzed in Fildes et al. (2020) and may be related to the evolution of the better-defined ring fault structure and piston development (Shelly and Thelen, 2019; Segall et al., 2019; Tepp et al., 2020).

Observing more caldera collapse eruptive sequences at Kīlauea and other volcanoes could help better understand: (a) if the earthquake behavior observed during the 2018 Kīlauea sequence was atypical or not comparatively, (b) what assumptions should be made when using this technique if it is used with volcanic related seismicity, or (c) if these active volcanic systems are too dynamic to nowcast. Additionally, the investigation should be conducted in geologic settings beyond volcanic settings including places where the method has been implemented before (e.g., Geysers geothermal area), but with intentionally varying the abidance of assumptions, in particular the GR Assumption. These further investigations may help determine the necessity and strictness of the current method assumptions and if there are adaptions that could be made for applying nowcasting to future earthquake sequences associated with volcanic eruptions.

Conflict of Interest

The authors declare no conflicts of interest relevant to this study.

Data Availability Statement

Earthquake data (magnitudes, epicenter locations, dates and times) downloaded from USGS Earthquake Catalog. Earthquake data acquired on 8/21/2019 (summit focused data) and 11/22/2019 (whole island data) from the United States Geological Survey Earthquake Catalog. Nowcasting data analysis carried out with Python v 3.7 (https://www.python.org/) and the code and data files are available on Fildes (2022) (https://zenodo.org/record/6554579#.YoJ_mPPML0o). Maps were made using the National Map and National Elevation Data set (NED) provided by the U.S. Geological Survey (2018) and OpenTopography which acquired lidar data collected by NCALM, processed by CRREL, and funded by the USGS (accessed 02/26/2020) (USGS, 2018).

References

Anderson, K. R., Johanson, I. A., Patrick, M. R., Gu, M., Segall, P., Poland, M. P., et al. (2019). Magma reservoir failure and the onset of caldera collapse at Kīlauea Volcano in 2018. *Science*, *366*(6470), eaaz1822. https://doi.org/10.1126/science.aaz1822

Anderson, K. R., Poland, M. P., Johnson, J. H., & Miklius, A. (2015). Episodic deflation inflation events at Kīlauea volcano and implications for the shallow magma system. In *Hawaiian volcanoes* (pp. 229–250). American Geophysical Union (AGU). https://doi.org/10.1002/9781118872079.ch11

Butler, R. (2020). Volcanic earthquake foreshocks during the 2018 collapse of Kīlauea Caldera. *Geophysical Journal International*, *220*(1), 71–78. https://doi.org/10.1093/gji/ggz425

Cervelli, P., & Miklius, A. (2003). The shallow magmatic system of Kilauea Volcano. *In The Pu'u 'Ō'ō-Kūpaianaha Eruption of Kīlauea volcano, Hawai'i: The first 20 years* (pp. 149–164). U.S. Geological Survey.

Donnellan, A., Parker, J., Heflin, M., Lyzenga, G., Moore, A., Ludwig, L. G., et al. (2018). Fracture advancing step tectonics observed in the Yuha Desert and Ocotillo, CA, following the 2010 M_w7.2 El Mayor-Cucapah Earthquake. *Earth and Space Science*, *5*(9), 456–472. https://doi.org/10.1029/2017EA000351

Eaton, J. P., & Murata, K. J. (1960). How volcanoes grow. *Science*, *132*(3432), 925–938. https://doi.org/10.1126/science.132.3432.925

Fildes, R. (2022). Rfildes/NowcastingKilauea: KilaueaNowcastingCodes (Version v1). [Data Set and Code]. Zenodo. https://doi.org/10.5281/zenodo.6554579

Fildes, R. A., Kellogg, L. H., Turcotte, D. L., & Rundle, J. B. (2020). Interevent seismicity statistics associated with the 2018 quasiperiodic collapse events at Kīlauea, HI, USA. *Earth and Space Science*, *7*, e2019EA000766. https://doi.org/10.1029/2019EA000766

Gansecki, C., Lee, R. L., Shea, T., Lundblad, S. P., Hon, K., & Parcheta, C. (2019). The tangled tale of Kīlauea's 2018 eruption as told by geochemical monitoring. *Science*, *366*(6470), eaaz0147. https://doi.org/10.1126/science.aaz0147

Giannone, D., Reichlin, L., & Small, D. (2008). Nowcasting: The real-time informational content of macroeconomic data. *Journal of Monetary Economics*, *55*(4), 665–676. https://doi.org/10.1016/j.jmoneco.2008.05.010

Gutenberg, B., & Richter, C. F. (1954). *Seismicity of the earth and associated phenomena* (2nd edn.). Princeton University Press. Retrieved from https://onlinelibrary.wiley.com/doi/abs/10.1111/j.2153-3490.1950.tb00313.x

Kumagai, H., Ohminato, T., Nakano, M., Ooi, M., Kubo, A., Inoue, H., & Oikawa, J. (2001). Very-long-period seismic signals and caldera formation at Miyake Island, Japan. *Science*, *293*(5530), 687–690. https://doi.org/10.1126/science.1062136

Liu, C., Lay, T., & Xiong, X. (2018). Rupture in the 4 May 2018 MW 6.9 earthquake seaward of the Kilauea East Rift Zone fissure eruption in Hawaii. *Geophysical Research Letters*, *45*(18), 9508–9515. https://doi.org/10.1029/2018GL079349

Llenos, A. L., & Michael, A. J. (2022). Modeling the occurrence of $M \sim 5$ caldera collapse-related earthquakes in Kīlauea volcano, Hawai'i. *Geophysical Research Letters*, *49*, e2020GL092242. https://doi.org/10.1029/2020GL092242

Luginbuhl, M., Rundle, J. B., Hawkins, A., & Turcotte, D. L. (2018). Nowcasting earthquakes: A comparison of induced earthquakes in Oklahoma and at the Geysers, California. *Pure and Applied Geophysics*, *175*(1), 49–65. https://doi.org/10.1007/s00024-017-1678-8

Luginbuhl, M., Rundle, J. B., & Turcotte, D. L. (2018a). Natural time and nowcasting earthquakes: Are large global earthquakes temporally clustered? *Pure and Applied Geophysics*, *175*(2), 661–670. https://doi.org/10.1007/s00024-018-1778-0

Luginbuhl, M., Rundle, J. B., & Turcotte, D. L. (2018b). Natural time and nowcasting induced seismicity at the Groningen gas field in the Netherlands. *Geophysical Journal International*, *215*(2), 753–759. https://doi.org/10.1093/gji/ggy315

Luginbuhl, M., Rundle, J. B., & Turcotte, D. L. (2019). Statistical physics models for aftershocks and induced seismicity. *Philosophical Transactions of the Royal Society A: Mathematical, Physical & Engineering Sciences*, *377*(2136), 20170397. https://doi.org/10.1098/rsta.2017.0397

Neal, C. A., Brantley, S. R., Antolik, L., Babb, J. L., Burgess, M., Calles, K., et al. (2019). The 2018 rift eruption and summit collapse of Kīlauea Volcano. *Science*, *363*(6425), 367–374. https://doi.org/10.1126/science.aav7046

Pasari, S. (2019). Nowcasting earthquakes in the Bay of Bengal region. *Pure and Applied Geophysics*, *176*(4), 1417–1432. https://doi.org/10.1007/s00024-018-2037-0

Pasari, S., & Mehta, A. (2018). Nowcasting earthqaukes in the northwest Himalaya and surrounding regions. *The International Archives of Photogrammetry, Remote Sensing and Spatial Information Sciences*, *42*(5), 855–859. https://doi.org/10.5194/isprs-archivesXLII-5-855-2018

Pasari, S., & Sharma, Y. (2020). Contemporary earthquake hazards in the West-Northwest Himalaya: A statistical perspective through natural times. *Seismological Research Letters*, *91*, 3358–3369. https://doi.org/10.1785/0220200104

Pasari, S., Simanjuntak, A. V., & Sharma, Y. (2021). Nowcasting earthquakes in Sulawesi island, Indonesia. *Geoscience Letters*, *8*(1), 1–13. https://doi.org/10.1186/s40562-02100197-5

Patrick, M., Orr, T., Anderson, K., & Swanson, D. (2019). Eruptions in sync: Improved constraints on Kīlauea Volcano's hydraulic connection. *Earth and Planetary Science Letters*, *507*, 50–61. https://doi.org/10.1016/j.epsl.2018.11.030

Patrick, M. R., Dietterich, H. R., Lyons, J. J., Diefenbach, A. K., Parcheta, C., Anderson, K. R., et al. (2019). Cyclic lava effusion during the 2018 eruption of Kīlauea Volcano. *Science*, *366*(6470). https://doi.org/10.1126/science.aay9070

Petersen, M. D., Shumway, A. M., Powers, P. M., Moschetti, M. P., Llenos, A. L., Michael, A. J., et al. (2021). 2021 U.S. National seismic hazard Model for the State of Hawaii. *Earthquake Spectra*, *38*, 865–916. https://doi.org/10.1177/87552930211052061

Roberts, N. S., Bell, A. F., & Main, I. G. (2015). Are volcanic seismic *b*-values high, and if so when? *Journal of Volcanology and Geothermal Research*, *308*, 127–141. https://doi.org/10.1016/j.jvolgeores.2015.10.021

27

Rowe, M. C., Thornber, C. R., & Orr, T. R. (2015). Primitive components, crustal assimilation, and magmatic degassing during the early 2008 Kīlauea summit eruptive activity. In *Hawaiian volcanoes* (pp. 439–455). American Geophysical Union (AGU). https://doi.org/10.1002/9781118872079.ch20

Rundle, J. B., Giguere, A., Turcotte, D. L., Crutchfield, J. P., & Donnellan, A. (2019). Global seismic nowcasting with Shannon information entropy. *Earth and Space Science*, *6*(1), 191–197. https://doi.org/10.1029/2018EA000464

Rundle, J. B., Luginbuhl, M., Giguere, A., & Turcotte, D. L. (2018). Natural time, nowcasting and the physics of earthquakes: Estimation of seismic risk to global megacities. *Pure and Applied Geophysics*, *175*(2), 647–660. https://doi.org/10.1007/s00024-017-1720-x

Rundle, J. B., Luginbuhl, M., Khapikova, P., Turcotte, D. L., Donnellan, A., & McKim, G. (2020). Nowcasting great global earthquake and tsunami sources. *Pure and Applied Geophysics*, *177*(1), 359–368. https://doi.org/10.1007/s00024-018-2039-y

Rundle, J. B., Turcotte, D. L., Donnellan, A., Ludwig, L. G., Luginbuhl, M., & Gong, G. (2016). Nowcasting earthquakes. *Earth and Space Science*, *3*(11), 480–486. https://doi.org/10.1002/2016EA000185

Segall, P., Anderson, K. R., Johanson, I., & Miklius, A. (2019). Mechanics of inflationary deformation during caldera collapse: Evidence from the 2018 Kīlauea eruption. *Geophysical Research Letters*, *46*(21), 11782–11789. https://doi.org/10.1029/2019GL084689

Shelly, D. R., & Thelen, W. A. (2019). Anatomy of a caldera collapse: Kīlauea 2018 summit seismicity sequence in high resolution. *Geophysical Research Letters*, *46*(24), 14395–14403. https://doi.org/10.1029/2019GL085636

Swanson, D. A., Jackson, D. B., Koyanagi, R. Y., & Wright, T. L. (1976). *The February 1969 east rift eruption of Kilauea Volcano, Hawaii (USGS Numbered Series No. 891)*. US Government Printing Office. Retrieved from http://pubs.er.usgs.gov/publication/pp891

Tepp, G. (2021). Material failure and caldera collapse: Insights from the 2018 Kilauea eruption. *Earth and Planetary Science Letters*, *553*, 116621. https://doi.org/10.1016/j.epsl.2020.116621

Tepp, G., Hotovec-Ellis, A., Shiro, B., Johanson, I., Thelen, W., & Haney, M. M. (2020). Seismic and geodetic progression of the 2018 summit caldera collapse of Kīlauea volcano. *Earth and Planetary Science Letters*, *540*, 116250. https://doi.org/10.1016/j.epsl.2020.116250

U.S. Geological Survey. (2018). National Map and National Elevation Dataset (NED) [Data Set]. USGS. Retrieved from https://usgs.gov/core-science-systems/ngp/tnm-delivery/

U.S. Geological Survey. (2019). Earthquake catalog [Data Set]. USGS. Retrieved from https://earthquake.usgs.gov/earthquakes/search/

USGS. (2018). Kilauea volcano, HI July 2018 acquisition airborne lidar survey. U.S. Geological Survey (USGS) in collaboration with the State of Hawaii. Federal Emergency Management Agency, Cold Regions Research and Engineering Laboratory, and the National Center for Airborne Laser Mapping. Distributed by OpenTopography [Data Set] https://doi.org/10.5069/G9M32SV1

Varotsos, P. A., Sarlis, N. V., & Skordas, E. S. (2002). Long-range correlations in the electric signals that precede rupture. *Physical Review E*, *66*(1), 011902. https://doi.org/10.1103/PhysRevE.66.011902

Varotsos, P. A., Sarlis, N. V., & Skordas, E. S. (2011). *Natural time analysis: The new view of time: Precursory seismic electric signals, earthquakes and other complex time series*. Springer.

Varotsos, P. A., Sarlis, N. V., & Skordas, E. S. (2017). Identifying the occurrence time of an impending major earthquake: A review. *Earthquake Science*, *30*(4), 209–218. https://doi.org/10.1007/s11589-017-0182-7

Varotsos, P. A., Sarlis, N. V., & Skordas, E. S. (2020). Self-organized criticality and earthquake predictability: A long-standing question in the light of natural time analysis. *Europhysics Letters*, *132*(2), 29001. https://doi.org/10.1209/0295-5075/132/29001

Varotsos, P. A., Sarlis, N. V., Skordas, E. S., Nagao, T., & Kamogawa, M. (2021). The unusual case of the ultra-deep 2015 Ogasawara earthquake (MW7.9): Natural time analysis. *EPL*, *135*(4), 49002. https://doi.org/10.1209/0295-5075/135/49002

Varotsos, P. A., Sarlis, N. V., Tanaka, H. K., & Skordas, E. S. (2005). Some properties of the entropy in the natural time. *Physical Review E*, *71*(3), 032102. https://doi.org/10.1103/PhysRevE.71.032102

Varotsos, P. A., Skordas, E. S., & Sarlis, N. V. (2020). Fluctuations of the entropy change under time reversal: Further investigations on identifying the occurrence time of an impending major earthquake. *EPL*, *130*(2), 29001. https://doi.org/10.1209/02955075/130/29001

References From the Supporting Information

Utsu, T. (1965). A method for determining the value of "*b*" in a formula log n = a − bM showing the magnitude frequency relation for earthquakes. *Geophysical Bulletin of Hokkaido University*, *13*, 99–103.

28

Chapter 3

Re-investigating the Strain-rate Constraint Hypothesis for Deep Earthquake Occurrence in Subducting Lithosphere

3.1 Introduction of Chapter 3 Work

This chapter switches focus from volcanic earthquakes at the surface of the Earth, to earthquakes occurring >70 km deep in subducting lithosphere. The initial idea for this project came from Magali Billen, building on her previous work. After I joined her lab and this project, together we developed novel subduction modeling methods using ASPECT to improve deep earthquake investigation utilizing subduction modeling and integrating real world observations.

Abstract

Unlike shallow earthquakes that are understood to occur through brittle failure, deep (>70 km) focus earthquake failure mechanisms and conditions are not as well understood. Higher temperatures and pressures in subducting lithosphere at these depths require a different process for earthquake failure. Current hypotheses under investigation are dehydration embrittlement, transformational faulting, and thermal shear instability. In addition to temperature constraints for each of these mechanisms, strain-rate variability in the lithosphere has recently been proposed as a constraint on slab seismogenesis: that is, deep earthquakes occur in high strain-rate regions within cold subducting slabs. However, this strain-rate constraint hypothesis was based on non-location-specific visco-plastic subduction modeling, positing a challenge for direct comparisons to earthquake observations. Here we present updated subduction modeling methods to compare more directly with deep earthquake observations to evaluate the strain-rate constraint hypothesis. This method uses a novel approach of imposing present-day slab geometry but holding it static while advecting only the stress tensor forward in time. To demonstrate that this novel approach can reproduce the stress orientations and stress and strain-rate patterns from a fully time-dependent model we also present a Proof of Concept model using a 2D synthetic slab.

A location-specific 2D dynamic visco-elastic-plastic subduction model with low-temperature plasticity is built based on present-day slab geometry and ages for a 2D profile of the Kermadec subduction zone. This model (using the above described static method) is used to determine physical conditions (strain-rate, stress, temperature, pressure) in the subducting lithosphere. To then evaluate the strain-rate constraint hypothesis with the location-specific static modeling results of Kermadec, regions of high strain-rate in the modeled slab are directly compared to the Kermadec earthquake observations. This initial investigation reveals that the depths of higher modeled strain-rates do broadly correlate with observed depths of higher earthquake activity, which is consistent with the original strain-rate constraint hypothesis. In addition, we show that the orientation of stresses in the modeled slab agrees with

observations from focal mechanisms. These updated location-specific subduction modeling methods will be used to set up and investigate more profiles in Kermadec and in other subduction zones. Continuing to test the hypothesis will improve our understanding of physical constraints on where seismicity in the slab occurs. Additionally, better understanding the conditions expected in the deep slab is an important step to improving the understanding of how and where the proposed deep earthquake failure mechanisms might be viable. We propose a larger workflow to combine our subduction modeling with numerical modeling of thermal shear instability as a next step in our investigation of deep earthquakes.

1 Background

1.1 Deep Earthquakes

Intermediate (70-300 km) and deep (> 300 km) earthquakes occur in lithosphere sinking into the Earth's mantle (Figure 1). In some ways deep earthquakes (inclusive of intermediate and deep depths) appear to be similar to shallow earthquakes. Focal mechanism solutions (FMS) of deep earthquakes indicate that like shallow earthquakes they exhibit shear failure. However, the high temperatures and pressures at depth hinder brittle failure [*Griggs and Handin*, 1960]. In order for brittle failure to occur in the deep slab, some other mechanism is required to overcome the high normal stresses or to localize deformation in the material [*Griggs and Handin*, 1960; *Scholz*, 2019]. There have been multiple proposed hypotheses for how these failures occur (some dis-proven, some remaining), but there is still no consensus. The question of how deep earthquakes fail – under what conditions and by which failure mechanism? – is still an open problem that requires further investigation.

1.1.1 General Characteristics

Our understanding of deep earthquake behavior is based mainly on seismological observations, laboratory experiments that approximate mantle conditions, and numerical modeling. Here, I provide a short summary of key observations from some recent deep earthquake re-
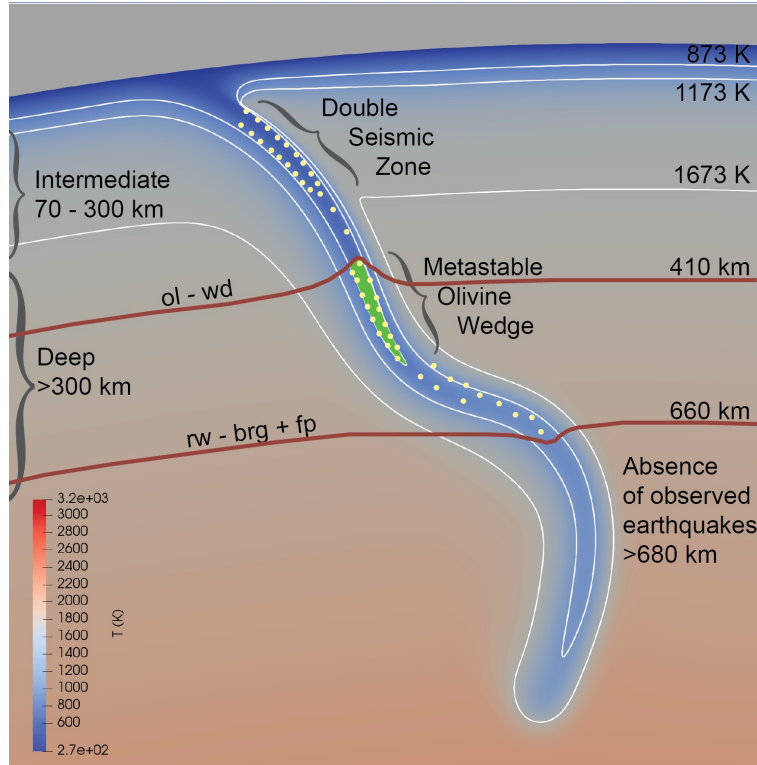
Figure 1: Schematic of deep earthquakes defined within a subducting slab. The conventional depth ranges for intermediate and deep earthquakes is labeled on the left side. The 410 km olivine (ol) to wadsleyite (wd) and 660 km ringwoodite (rw) to bridgemanite (brg) and (fp) phase transitions are indicated with the dark red lines. Note the respective elevation and depression of the 410 and 660 within the cold slab. White contours are temperature contours of where it is proposed metastable olivine would be possible (<873 K), where seismicity is possible (<1173 K), and as visual guide for slab shape (1673 K). The yellow dots represent earthquake hypocenters. See text for details of labeled double seismic zone and metastable olivine wedge. *Image by Rebecca Fildes and digitized by Magali Billen.*

views, but refer the reader to *Green and Houston* [1995], *Frohlich* [2006], *Houston* [2015], and *Zhan* [2020] for more complete descriptions.

For events of comparable magnitude, relative to shallow earthquakes, deep earthquakes are observed to exhibit faster (but more varied) rupture velocities and shorter rupture duration. Although static stress drops are challenging to measure accurately and may be heterogeneous across a fault plane, the estimates for deep earthquakes tend to be an order of magnitude larger than for shallow earthquakes. Deep earthquakes also have lower radiation efficiencies, especially larger magnitude events. These lower seismic efficiencies are hypothesized as evidence of melting or some other process resulting in energy dissipation near the

fault zone during the rupture process. Deep earthquakes, like shallow, are sometimes observed to be comprised of multiple subevents. Some deeper earthquakes though appear to have increased rupture complexity, which varies with depth. The production of aftershocks themselves is a shared property of both shallow and deep earthquakes along with the observation that they generally follow Omori's law of aftershock decay [*Utsu*, 1961]. However, it has been observed that there is a lack of aftershocks for events 350-550 km deep, which has been proposed to be related to the increased rupture complexity. The deepest events, found below 550 km, tend to be the simplest and have the shortest rupture duration despite their large magnitudes. These depth varying characteristics have been hypothesized to be signals of the depth constraints on where different earthquake failure mechanisms are active.

Statistical scaling laws are another way to characterize seismicity in a region and changes in how these laws are followed can provide insight into the physical process causing the changes. Both shallow and deep seismicity generally follow the Gutenberg-Richter frequency-magnitude scaling law

$$log_{10}(N_c \geqslant M) = a - bM \tag{1}$$

which quantifies the scaling between event magnitude, M, and the cumulative number of events occurring of that magnitude or greater, $N_c \geqslant M$ [*Gutenberg and Richter*, 1941]. The variable a is the total seismicity and b, termed 'b value', represents the scaling between small and large magnitude events. For both shallow and deep earthquakes b $\approx$ 1 when looking at the global data set. In contrast to shallow earthquakes, however, the b values for deep earthquake vary strongly between different subduction zones. They also vary with depth within individual subduction zones. The b value variations have been hypothesized to be thermally controlled and, similar to the above observations, potentially to be explained by changes in different failure mechanisms operating at different depths and temperatures [*Houston*, 2015; *Zhan*, 2017].

1.1.2 Proposed failure mechanisms

There are currently three main proposed mechanisms for initiating intermediate and deep earthquakes: dehydration embrittlement (DE), transformational faulting (TF) of metastable olivine, and thermal shear instability (TSI). Additionally, a very recent study by *Levitas* [2022] proposed strain induced phase transitions of olivine as a mechanism for deep earthquake initiation, which differs from the popular hypothesis of thermally induced TF (referred to as TTF in the remainder of this chapter). It has also been proposed that multiple mechanisms work together during rupture (e.g., *Frohlich* [2006]; *Houston* [2015]; *Zhan* [2017, 2020]).

Seismicity, the number of earthquakes greater than a given size, varies with depth in subducting slabs (Figure 2a)(*Zhan* [2020] and references within). Globally, there is a peak in intermediate depth seismicity around 100 km depth followed by a decay in earthquake activity down to 300 km. Observed double seismic zones (DSZ) (Figure 1) align with this tapering of activity and have been interpreted as two isotherms along which DE could occur (e.g., *Yamasaki and Seno* [2003]). From 300 km, a low in earthquake activity persists down to about 410 km depth before increasing again and coming to a peak around 600 km depth. This distribution of deeper activity is proposed to result from TTF within a metastable olivine wedge at these depths. Globally, earthquake activity is not observed below about 660 km. The deepest mainshock observation locates a M_w 7.9 at about 680 km depth in Bonin, but is thought to occur in upper mantle material above the locally depressed 660 phase transition (e.g., *Obayashi et al.* [2017]). This non-uniform depth distribution of earthquakes varies at regional scales between subduction zones (Figure 2b-d). Additionally, the maximum depth of seismicity is not consistent between subducting slabs. This observation has previously been interpreted as resulting from a nonlinear relationship between the maximum depth of earthquakes and the thermal parameter for a subduction zone ($\phi = V_{sub}A_{sub}$, where V_{sub} is the vertical sinking rate and A_{sub} is the age of the subducting lithosphere [*Gorbatov and Kostoglodov*, 1997; *Kirby et al.*, 1996; *Wiens and Gilbert*, 1996].
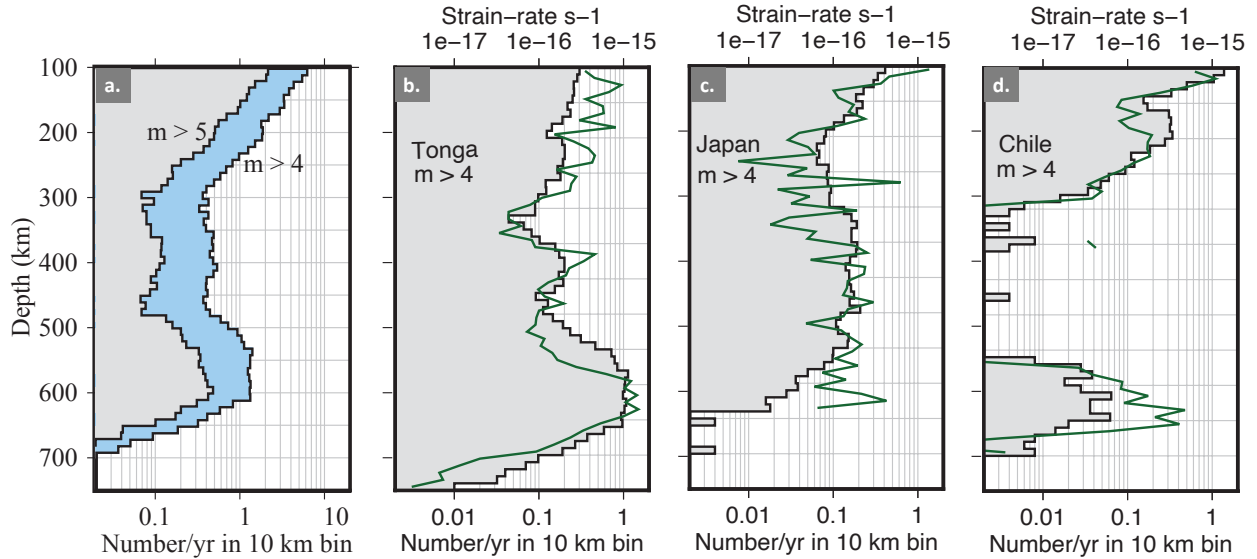
Figure 2: Global and regional variations in seismicity rate and strain-rate depth profiles. (a) Global depth distribution of events $M_W > 4$ *(blue histogram)* and events $M_W > 5$ *(gray histogram)*. **(b-d)**Regional seismicity rate of events $M_W > 4$ *(gray histogram)* and strain-rate *(green line)* as a function of depth in **(b)** Tonga, **(c)** Japan, **(d)** Chile. Earthquakes are from the ISC-EHB catalog for events from 1964-2014. *Modified images from Magali Billen.*

Dehydration embrittlement   DE is mainly proposed for intermediate-depth earthquakes (70-300 km), but it's depth extent are not fully known. In its original form this mechanism is thought to induce shear failure by increasing pore pressure at depth through dehydration of hydrous minerals (e.g., serpentine [*Raleigh and Paterson*, 1965; *Meade and Jeanloz*, 1991; *Gasc et al.*, 2017]). The increasing pore pressure counteracts the very high normal stresses and extends the depth over which brittle fracture can occur. A new variation on the DE mechanism for intermediate depths was recently proposed based on laboratory experiments: dehydration-driven stress transfer [*Ferrand et al.*, 2017]. Dehydration of mantle minerals is still necessary, but in this mechanism it is not fluid overpressure, but the stress changes during dehydration that leads to embrittlement.

There is debate as to whether or not there are sufficient fluids present to cause DE deeper than 300 km [*Houston*, 2015]. A recent study found evidence of fluids in diamond inclusions from the mantle transition zone, suggesting this as evidence for transport of mobile fluids deeper in the slab, which could then be related to deep earthquake triggering [*Shirey et al.*, 2021]. It was also recently suggested, based on seismological observations of the sinking

Pacific Plate, that the 2013 M_w 8.3 Sea of Okhotsk deep earthquake was a result of DE. *Zhang et al.* [2021] found that based on their seismic analysis, the subducting slab must still contain fluids in the transition zone, and therefore the deep earthquakes in this region could be a result of DE.

Thermally Induced Transformational faulting (TTF)   In the cold interior of slabs, metastable olivine may persist into the transition zone if the olivine to spinel (wadsleyite) reaction is kinetically hindered [*Rubie and Ross*, 1994]. Within this metastable olivine wedge (MOW) (Figure 1), lenses of metastable olivine may transition to spinel under enough stress and form anti-cracks of denser, superplastic spinel. Shear failure occurs when these anti-cracks grow and connect with each other due to the release of heat and volume collapse during the exothermic phase change [*Green and Houston*, 1995; *Kirby et al.*, 1996]. TTF in olivine has been observed in laboratory experiments (e.g., *Green and Burnley* [1989]; *Green and Zhou* [1996]; *Mosenfelder et al.* [2001]; *Alpert et al.* [2010]; *Gasc et al.* [2022]). *Incel et al.* [2017] also found TTF to occur in laboratory experiments during the transformation from lawsonite-blueschist to lawsonite-eclogite. Metastable olivine [*Tetzlaff and Schmeling*, 2009] and metastable pyroxene [*Agrusta et al.*, 2014] have been incorporated in subduction models, but better understood kinetics would improve the understanding of their potential effects.

TTF is observationally limited due to difficulties in seismically identifying MOWs in subduction zones other than Japan. Seismic heterogeneity in the shallower lithosphere obscures the signals coming through the deeper slab, making these suspected narrow wedges that may produce only small seismic perturbations harder to detect [*Koper et al.*, 1998]. Japan is unique in their extremely high density network of seismometers at the surface and a slab that hosts a lot of deep earthquakes. These conditions are essential for imaging these narrow zones of the metastable olivine. In Japan, *Shen and Zhan* [2020] used inter-source interferometry to seismically identify a 30 km wide MOW from about 410 km, narrowing

down to a terminus of about 580 km. As a note relating back to the DE description above, this seismic observation of a MOW implies that dehydration was completed at shallower depths as a hydrated slab would prevent the formation of a MOW. In contrast, seismological investigations of Tonga found that in order to fit the body-wave observations that traveled through the slab, they did not need to invoke a MOW [*Koper et al.*, 1998].

Even if it is assumed that a MOW exists in a slab, the standard explanation of how TTF occurs in deep slabs is still unable to explain the observed intermediate and deep depth distribution of seismicity. This is because TTF, which is a thermally-induced phase transition, is expected to produce a continuous zone of seismicity along the isothermal boundary of a MOW (Figure 1). However, several subduction zones such as in South America (Figure 2) and Java-Sumatra exhibit large gaps in seismicity between 400 and 550 km depth, but host large events deeper than 550 km. This suggests other constraints and/or mechanisms may be responsible for the discontinuous pattern of seismicity and deep, isolated earthquakes found in some regions.

Thermal shear instability   TSI has been proposed for both intermediate and deep earthquakes [*Griggs et al.*, 1969; *Ogawa*, 1987; *Hobbs and Ord*, 1988]. This ductile process induces slip through shear melting as a result of a steep, rapid increase in temperature (thermal runaway) in a localized shear zone. The temperature spike is a product of a positive feedback loop between viscous dissipation and thermal weakening of the rock (e.g., *Ogawa* [1987], *Kelemen and Hirth* [2007], *John et al.* [2009], *Thielmann et al.* [2015], *Thielmann* [2018]). Modeling results propose that thermal runaway can result from self-localization within a relatively thin, local zone of perturbed material (e.g., weaker material, finer grain size). Evidence of melting during rupture for large events is supported by low radiation efficiency and slower rupture speeds (e.g., *Kanamori et al.* [1998]). More recently, intermediate depth seismicity has been observed to initiate slow, very dissipative ruptures followed by a large drop in stress and amount of radiated energy [*Poli et al.*, 2016]. These observations were

interpreted as evidence of melting, specifically hypothesizing TSI to be involved in the rupture. Proposed geological evidence of shear melting and intermediate depth TSI are exhumed pseudotachylyte veins found in ductile regimes (e.g., mylonite) thought to have formed in the deep crust (e.g., $\sim$ 2 GPa and 650-700°C in *John et al.* [2009]; $\sim$ 1.5 GPa and 470°C in *Andersen et al.* [2008]). Experiments on dunite and harzburgite (wet and dry) conducted at shallow intermediate-depth temperature and pressure conditions showed localized heating could be induced and faulting occurred in experiments with background strain-rates from 1e-16 - 1e-13 s^{-1} [*Ohuchi et al.*, 2017].

TSI is favored in regions with low temperature, high stress, and high strain-rate conditions (e.g., the transition zone) [*Karato et al.*, 2001]. *Billen* [2020] showed that high strain-rates occur in regions of bending and unbending and calculated strain-rates in the cold slab similar to the range found experimentally to induce TSI at intermediate depths [*Ohuchi et al.*, 2017]. The numerical modeling of TSI at deep depths is a future direction of the work in this chapter, building on previous modeling efforts [*Thielmann et al.*, 2015; *Thielmann*, 2018]. The proposed methods and an example test model are shown in Appendix A.

1.2   Strain-rate Constraint Hypothesis

Previous distribution and depth extent explanations of deep earthquakes rely primarily on thermal constraints within the slab. Citing shortcomings in temperature being the sole factor determining where deep earthquake mechanisms are active, and pointing out that strain-rate had previously been shown to be an important constraint individually for TTF [*Burnley et al.*, 1991] and TSI [*Ohuchi et al.*, 2017], *Billen* [2020] proposes that strain-rate is an additional constraint. Variations in strain-rate within subducting slabs arise from rheology and buoyancy forces interacting, especially within the transition zone as the slab encounters multiple phase transitions. *Billen* [2020] used 2D numerical subduction modeling to create strain-rate depth profiles for subducting slabs and found broad correlations with seismicity depth profiles coming from earthquake observations (Figure 3). For a comparison of model

"snap-shots" with a slab shape similar to an observed present-day slab shape, depths with low strain-rates in the model corresponded to where there were large gaps in earthquake occurrence. Similarly, depths of high strain-rate in the model (e.g., bending and unbending regions) aligned with observed spikes in earthquake occurrence. The models also showed a sudden drop in strain-rate below 660 km, which agrees with the observed disappearance of earthquake activity below this depth.
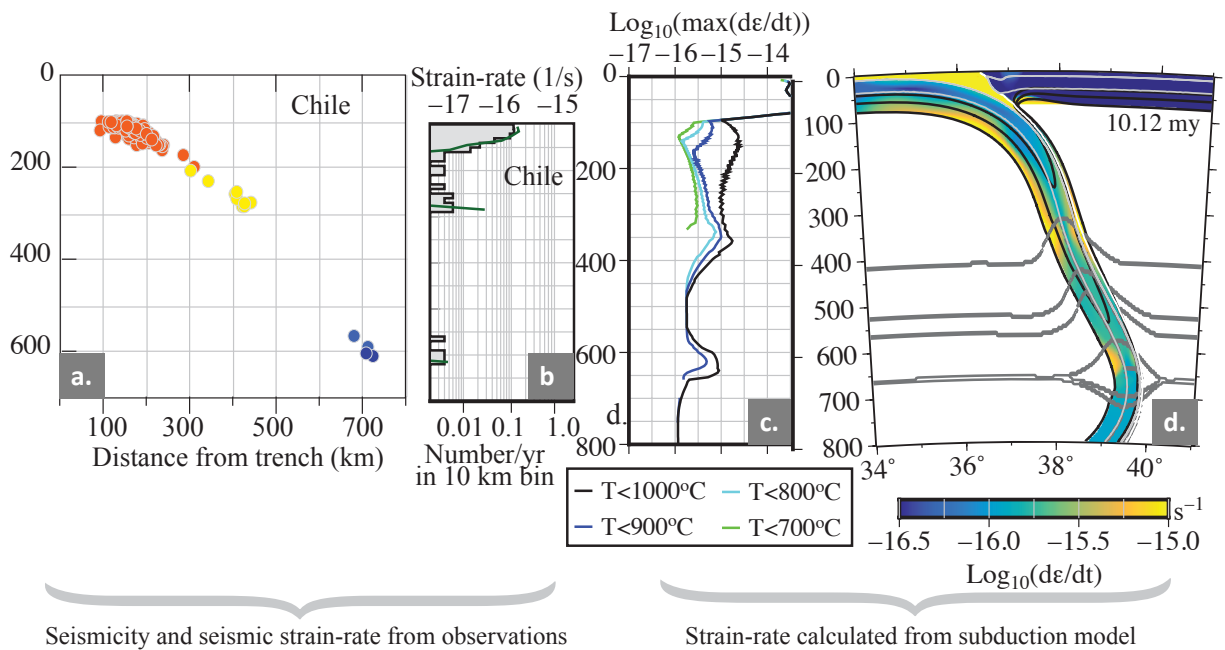
Figure 3: Similariaties between observed and modeled strain-rate profiles in Chile. (a) Cross section of earthquake distribution for for Profile 8 of *Billen* [2020] in Chile. Earthquakes are from the ISC-EHB catalog for events from 1964-2014. Colors indicate depth. **(b)** Regional seismicity rate of events $M_W > 4$ *(gray histogram)* and strain-rate *(green line)* as a function of depth for same profile as (a). **(c)** Maximum strain-rate measured below a specific slab temperature as a function of depth for model shown in (d). Lower temperature ranges correspond to the interior of the slab. **(d)** Cross-section of *Billen* [2020] Model 2 at 10.12 Ma. Colors are strain-rate within the $1000°$ C contour. *Modified images from Magali Billen*

The conclusions of *Billen* [2020] can be used to improve the understanding of slab conditions that lead to deep earthquakes and the testing of deep earthquake failure mechanisms, but first, new subduction models are needed to more rigorously test this new strain-rate constraint hypothesis. *Billen* [2020] used generic (non-location-specific) visco-plastic models to compare time-slices of strain-rate distributions with regional earthquake observations.

In their study they cite the importance of future models including elasticity and different plasticity formulations as well as building subduction models for specific locations. Visco-elastic-plastic models set up to run on shorter timescales for location-specific slab profiles are needed in order to 1) more accurately model the slab conditions and short-term evolution and 2) have a more direct comparison to observed earthquakes. We hypothesize that the new modeling methods developed in this chapter will verify and strengthen the general strain-rate constraints proposed in *Billen* [2020]. We also further propose their utility in a workflow to utilize these results to test specific deep earthquake failure mechanisms, focusing first on TSI.

1.3 Previous modeling

As with the models discussed in the prior section, subduction models are often set up to run for many millions of years and do not always include elasticity in their rheology. On the multi-million year timescale, deformation is dominated by viscous mechanisms and therefore elastic deformation is not as relevant. However, questions of earthquake behavior within slabs at both shallow and deep depths require investigating plate conditions and deformation on shorter, seismic timescales, which requires incorporating elasticity. It has been shown that including elasticity is not expected to affect development of long-term slab morphology (*Royden and Husson* [2006]; *Morra et al.* [2006]). *Farrington et al.* [2014] has shown though that incorporating elasticity into a viscous subduction model will affect stress magnitudes, spatial patterns and orientations. *Bessat et al.* [2020] illustrated the interplay between different deformation mechanisms (composite visco-elastic-plastic models, including Peierls creep and Drucker-Prager) and concluded that elasticity is important for reasonably calculating stresses and for how deformation is partitioned amongst the deformation mechanisms in numerical subduction models.

Visco-elastic and visco-elastic-plastic numerical subduction modeling in the context of earthquake behavior has been developed in previous studies. *Van Dinther et al.* [2013] and

Van Zelst et al. [2019] both tie together different numerical modeling methodologies to investigate processes of different temporal and spatial scales related to earthquakes and seismic cycles. These two studies focus on the shallow, megathrust interface as a region where the timescales of long-term subduction evolution and the short seismic timescale behavior of earthquakes need to come together. Linking these different timescales is key for understanding both processes better. The work done in this chapter builds on these previous methodologies of linking long-term subduction evolution with short-term seismic cycle behavior. Our methods will be focused on the deeper slab behavior and the conditions leading to deep earthquakes, but will similarly be trying to link long-term subduction evolution with seismic timescale behavior.

2 Goals and Motivation

The goal of this work is to develop subduction models specifically to investigate deep earthquake occurrence, build on the work of Billen (2020), and retest the strain-rate constraint hypothesis (Section 1.2). The models used in Billen (2020) were not built specifically to answer questions about deep earthquakes, but they did provide some primary goals for furthering the investigation of deep earthquakes as described above. They suggested future directions included updating the subduction model rheologies to include elasticity and low-temperature plasticity, and to build location-specific models to enable more direct comparisons to observations.

Low-temperature plasticity is an observed behavior of rocks (e.g., *Goetze et al.* [1978]; *Idrissi et al.* [2016]; *Mei et al.* [2010]) expected to occur in the colder, high stress areas of the subducting lithosphere. Low-temperature plasticity is expected to lead to higher strain-rates at higher stresses and could affect the morphology of the slab. We also know that lithospheric and mantle rocks behave elastically (e.g., earthquakes occur, the rocks can transmit seismic waves). Incorporating elasticity is not expected to affect the morphology of the slab, but is expected to affect the magnitude and locations of maximum stress in the slab, as well as the

orientation of principal stresses [*Farrington et al.*, 2014]. For example, the maximum stresses in a visco-elastic model will build in areas of maximum curvature, rather than in areas of maximum bending rates as occurs in viscous models. These stress properties have observable counter parts in the real world where deep earthquakes are occurring, so it is important to incorporate these elastic effects into our models.

The location-specific models as opposed to generic models are an important development for this investigation as well. The global seismicity depth profile (Figure 2a) is not representative of the seismicity depth profiles for each individual subduction zone. Although they all host deep earthquakes, Figures 2b-d illustrate the significant differences between the Tonga, Japan, and Chile seismicity depth profiles. The origin of these differences is not known, but could be related to plate age (temperature), subduction velocity, and shape of the sinking slab; all which vary between subduction zones and could affect the mechanism(s) leading to deep earthquakes. Therefore, creating location-specific models allows us to account for this variability between subduction zones. Additionally, different locations along strike within a single subduction zone, exhibit varying seismicity depth profiles. Since the models in this study will be 2D, multiple 2D profiles within a subduction zone should also be built for comparison. In order to more directly couple numerical subduction models with deep earthquake observations, models that incorporate these unique morphologies and temperature structures (result of age and velocities) are needed. Importantly, by building 2D subduction models for a specific location, we can directly compare to the observed deep earthquakes for that very same location in the real world to test our hypotheses.

Therefore, the main goals of this study are:

1. Incorporate elasticity and low-temperature plasticity into subduction models.

2. Build location-specific subduction models to approximate present-day slab conditions.

3. Demonstrate that the modeling approach is a valid method with a Proof of Concept workflow.

42

4. Retest the Billen (2020) strain-rate constraint hypothesis for deep earthquakes with the updated visco-elastic-plastic location-specific subduction models.

3   Subduction Modeling Methods

The 2D dynamic visco-elastic-plastic subduction models developed in this study build on the visco-plastic models of *Billen* [2020] discussed above to incorporate elasticity, low temperature plasticity, and to build location-specific models. This section overall describes the setup for a general dynamic model with an initial proto slab, pointing out where additional temperature and geometry information will need to be incorporated for the location-specific models. Section 4 below illustrates how to build the location-specific models informed by present-day observations in a detailed example 2D profile from the Kermadec subduction zone.

3.1   Numerical Methods

The subduction models are run using the finite element code ASPECT version 2.5.0-pre [*Kronbichler et al.*, 2012; *Heister et al.*, 2017; *Bangerth et al.*, 2023a, b]. The Geodynamic World Builder (GWB) version 0.5.0-pre [*Fraters et al.*, 2019; *Fraters*, 2020] is used with ASPECT to set up the initial conditions for composition (geometry) and temperature. These initial conditions are read into ASPECT, the code in which the numerical simulations are then carried out. The subduction model is dynamic in that subduction is driven only by buoyancy forces (i.e., we do not prescribe plate velocities).

The simulations are run using the extended Boussinesq approximation (EBA) to solve the conservation equations for mass, momentum, and energy. The EBA assumes incompressibility, but incorporates an initial adiabatic gradient, shear heating, and latent heat from phase transitions [*Christensen and Yuen*, 1985; *Ita and King*, 1994]. Under the incompressibility

assumption, the conservation of mass equation is:

$$\nabla \cdot \vec{\mathbf{u}} = 0 \tag{2}$$

where $\vec{\mathbf{u}}$ is the velocity vector. The conservation of momentum equation is:

$$\nabla \cdot \boldsymbol{\sigma} = \nabla \cdot \boldsymbol{\tau} - \nabla p = \vec{\mathbf{f}} \tag{3}$$

where $\boldsymbol{\sigma}$ is the total stress tensor $(\eta \nabla^2 \vec{\mathbf{u}})$, $\boldsymbol{\tau}$ is the deviatoric stress tensor and p is the pressure. $\vec{\mathbf{f}}$ is the buoyancy force term that accounts for density variations due to composition, temperature, and phase transitions. Recall the buoyancy forces (i.e., $\rho \vec{\mathbf{g}}$ where ρ is density and $\vec{\mathbf{g}}$ is gravitational acceleration) are the driving forces in this model.

Moresi et al. [2003] showed that for a visco-elastic-plastic rheology the deviatoric stress tensor can be approximated as

$$\tau^{t+\Delta t_e} = 2\eta_{eff}\varepsilon_D^{t+\Delta t_e}(\vec{\mathbf{u}}^t) + \check{\tau}\frac{2\eta_{eff}}{\mu \Delta t_e} \tag{4}$$

where Δt_e is the elastic time step. The elastic time step is a time step that tracks the stored elastic stress and is defined as greater than or equal to the computational time step. In our models we use a fixed time step throughout the model run. See Section 6.2.3 for test models of how varying the selection of this fixed value affects the results. The superscript t indicates the previous time step and $t + \Delta t_e$ indicates the current time step. $\varepsilon_D(\vec{\mathbf{u}})$ is the deviatoric strain-rate tensor, μ is the shear modulus, and $\check{\tau}$ is the stress history term that is advected and rotated into the current reference frame according to the velocity field ($\vec{\mathbf{u}}$). Here η_{eff} is the numerical viscosity, which accounts for both the visco-plastic and elastic components of the rheology:

$$\eta_{eff} = \frac{\eta \Delta t_e}{\Delta t_e + \alpha} \tag{5}$$

where η is the viscosity harmonically averaged from the viscous-plastic deformation mech-

anisms and α is the Maxwell relaxation time $(\frac{\eta}{\mu})$. Substituting equation 4 into equation 3, the conservation of momentum equation becomes

$$\nabla \cdot \left[2\eta_{eff}\varepsilon_D^{t+\Delta t_e}(\vec{\mathbf{u}}^t)\right] - \nabla\mathbf{p} = \vec{\mathbf{f}}^{t+\Delta t_e} - \mathbf{F}^{e,t} \tag{6}$$

The current timestep body forces are $\vec{\mathbf{f}}^{t+\Delta t_e}$. The second force term, $\mathbf{F}^{e,t}$, is an additional force term arising from the approximation used to incorporate the elasticity into the visco-plastic Stokes equation:

$$\mathbf{F}^{e,t} = -\frac{\eta_{eff}}{\mu\Delta t_e}\check{\tau}^t \tag{7}$$

This term accounts for the internal elastic stresses stored from initial conditions or the prior time step and advected with the flow, $\check{\tau}^t$. The origin of this term is demonstrated in the derivation of the visco-elastic-plastic rheology (Section 3.3).

The conservation of energy equation, under the EBA assumption accounts for advection, diffusion, shear heating, and latent heat related to phase transitions:

$$\left(\bar{\rho}C_p - \bar{\rho}T\Delta S\frac{\partial X}{\partial T}\right)\left(\frac{\partial T}{\partial t} + \vec{\mathbf{u}} \cdot \nabla T\right) - \nabla \cdot k\nabla T = 2\eta_{eff}\varepsilon_D(\vec{\mathbf{u}}) : \varepsilon_D(\vec{\mathbf{u}}) + \bar{\rho}T\Delta S\frac{\partial X}{\partial p}\vec{\mathbf{u}} \cdot \nabla\mathbf{p} \tag{8}$$

Here C_p is the isobaric heat capacity, ΔS is the change in entropy during the phase change, X is the fraction of material that has gone through the phase change, t is time, and k is the thermal conductivity. The background temperature follows an adiabatic gradient with potential temperature of 1573 K. The values implemented for the constant parameters can be found in Table 5 and the parameter file located in Appendix B.

3.2 Model setup

Domain The model domain is a 2D spherical slice 80° in longitude and 2,890 km deep extending from Earth's surface down to the core mantle boundary (Figure 4). The model uses adaptive mesh refinement to preserve resolution of about 0.94 km x 1.05 anywhere the

temperature is $\leqslant 1600$ K. The initial mesh coarsens with depth and radially away from the slab to a resolution of 60.2 km x 47.8 km in the lower most mantle (Figure 5). The adaptive refinement re-calculates the mesh every five time steps according to the new temperature solution refining areas that have become colder than 1600 K and coarsening areas that become warmer than 1600 K. This provides consistently high resolution throughout the slab independent of deformation.
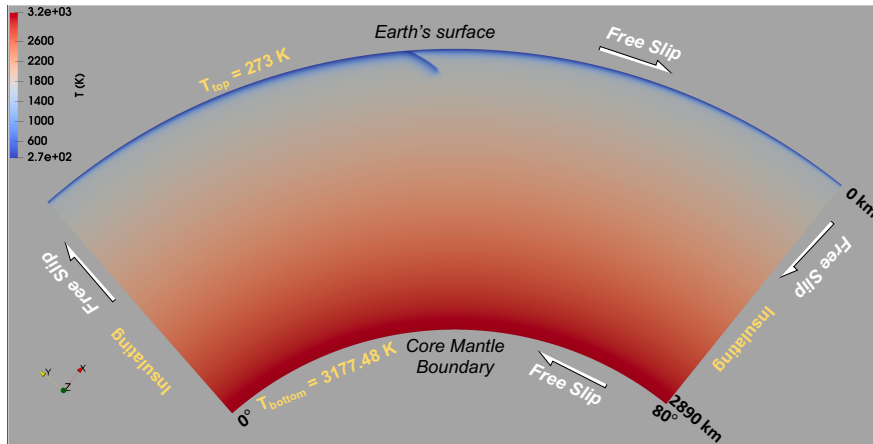
Figure 4: Full model domain with velocity and temperature boundary conditions noted. Colorbar indicates initial temperature field solution. Temperature and velocity boundary conditions described in text.
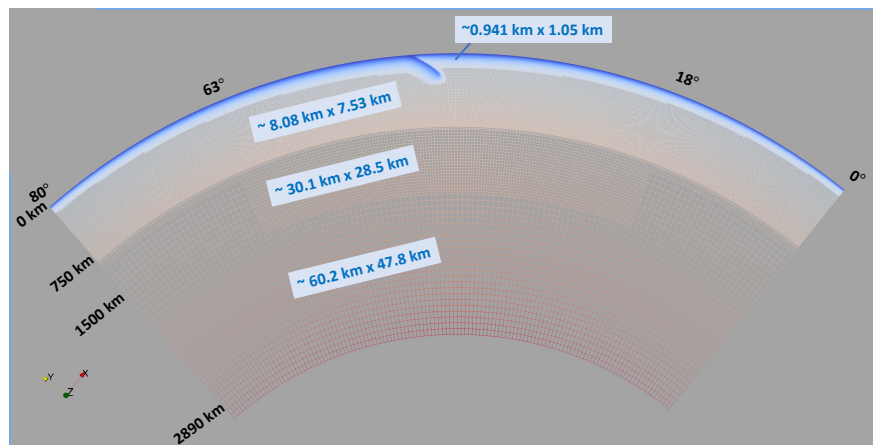
Figure 5: Initial model refinement for the whole whole model domain. Colorbar indicates initial temperature field solution. As described in text, the finest resolution is within a temperature contour of 1600 K. The rest of the mesh coarsens with increasing depth and width away from the slab. This mesh structure will change as the model runs according to the adaptive mesh strategy described in the text.

Plate Geometry and Composition: The initial composition and geometry conditions are set up in GWB and read into ASPECT.

Generic Model: The model consists of an overriding plate, subducting plate and slab. To fully decouple the plates from the sidewalls of the domain, two regions in the upper left and right corners of the domain are set to a prescribed constant numerical viscosity of ~1e20 Pa·s. These are numerical tools that allow the plates at the surface to move freely towards or away from the corners. The plates and slab are divided into layers defined by the initial composition [*Arredondo and Billen*, 2016, 2017; *Billen and Arredondo*, 2018]. The shallowest and thinnest layer is a 7.5 km thick basaltic crust (3000 kg/m^3). Below this is a 27.5 km thick harzburgite layer (3235 kg/m^3). The rest of the plates, slab and mantle are assigned the pyrolite composition (3300 kg/m^3) (Figure 6).

Location-specific: For these models the geometry is set up to be the present-day slab geometry and the simplified plate configuration at the surface based on observations. The simplified plate geometries are found in *Bird* [2003]. The slab geometry is calculated from the Slab 2.0 catalog, which contains depth to slab top data for all active subduction zones [*Hayes et al.*, 2018]. These depths are calculated from seismic observations including tomography and earthquakes. The depth to slab top data can be converted into a 2D continuous profile representative of the slab geometry that GWB can read in.

Temperature and Boundary Conditions: The initial temperature conditions are set up in GWB and read into ASPECT.

Generic Model: The initial thermal structure of the model as well as the temperature and velocity boundary conditions are illustrated in Figure 4. Thermal structures of the plates at the surface are calculated using a half-space cooling model based on plate age. The thermal structure of the slab is set up using a modified half-space cooling model, also assuming a plate age and rate of convergence. The thermal boundary conditions are insulating at both the left and right sides, while the top and bottom are held fixed to 273 K and 3177 K,

respectively. The bottom boundary temperature is set to match the adiabatic gradient at the core mantle boundary. All four domain boundaries have free-slip velocity conditions.

Location-specific: The plate and slab ages and velocities needed for the temperature models come from observations for the specific modeled location (e.g., ages from *Seton et al.* [2020] and velocities from MORVEL plate motion calculator [*DeMets et al.*, 2010]).

Phase Changes   This model accounts for seven equilibrium phase transitions, which are fully outlined in *Arredondo and Billen* [2016] and *Arredondo and Billen* [2017] (Figure 6). The olivine portion has three equilibrium phase transitions: olivine to wadsleyite at 410 km, wadsleyite to ringwoodite at 520 km, and at 660 km ringwoodite transitions to bridgmanite + ferropericlase. The phase transition of pyroxene to majoritic garnet beginning at about 300 km depth is not included in these models. At about 560 km, calcium-rich garnet and clinopyroxene transition to calcium-perovskite (and garnet). In the warm mantle, garnet changes to bridgmanite at 660 km, but within the cold slab, garnet changes to ilmenite first, then transitions into bridgmanite. Additionally, the weak basaltic crustal layer transitions to a stronger, denser eclogite layer (3540 kg/m^3) at 80 km depth [*Arrial and Billen*, 2013; *Arredondo and Billen*, 2016]. Tables 1 and 2 provides the phase transition values used for the models in this chapter.

The model incorporates the compositionally dependent equilibrium phase transitions using a field method that tracks the basalt, harzburgite, and pyrolite compositional fields. The Discontinuous Galerkin method with a bound preserving limiter is used to solve the advection equation for each compositional field [*He et al.*, 2017]:

$$\frac{\partial c_i}{\partial t} + \mathbf{u} \cdot \nabla c_i = q_i \tag{9}$$

where c is the fraction of composition i, t is time, $\mathbf{u}$ is velocity, and q_i is a reaction rate for the phase transition from one composition to another.
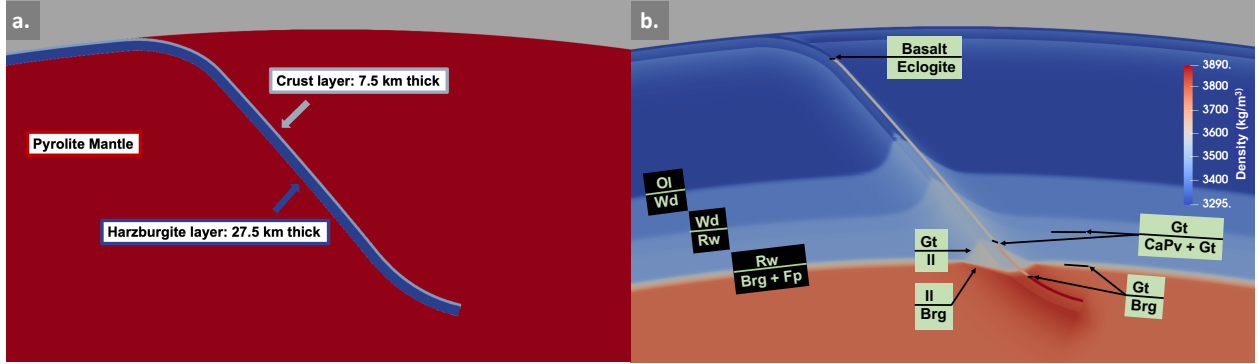
Figure 6: Compositional layering and density structure for phase transitions for a generic subducting slab. (a) Compositional layers described in text colored by composition type. **(b)** The seven equilibrium phase transitions (and eclogite transition) outlined in the text for a subducting slab and surrounding mantle, colored by density.

Phase Transition	Depth [km]	γ [MPa/K]	$\Delta\rho$ [%] *Pyrolite*	$\Delta\rho$ [%] *Harzburgite*	T range (K)
Ol → Wd	410	4	2.86	4.24	full
Wd → Rw	520	4.1	1.41	2.06	full
Gt → CaPv + Gt	560	4	0.32	0.00	full
Gt → Il	670	4	2.14	1.08	< 1662
Il → Brg	670	-3.1	2.26	1.17	< 1662
Rw → Brg + Fp	670	-2	4.66	6.82	< 1662
Gt → Brg	670	1.3	4.30	2.18	> 1662
Rw → Brg + Fp	670	-2	4.73	6.90	> 1662

Table 1: **Phase transition values implemented for Pyrolite and Harzburgite compositions.** The widths of all phase transitions listed is 5 km and the temperatures are 1662 K. γ is the Clapeyron slope. The references for γ are (in order): *Katsura et al. [2004]*, *Inoue et al. [2006]*, *Saikia et al. [2008]*, *Wang et al. [2004]*, *Fei et al. [2004]*, *Hirose [2002]*, *Litasov and Ohtani [2005]*. The density change is calculated as $\Delta\rho = \frac{\rho_B - \rho_A}{\rho_A}$ x 100 where ρ_A is the density above the phase transition and ρ_B is the density below the phase transition. The references for $\Delta\rho$ are (in order): *Yonggang et al. [2008]*, *Sinogeikin et al. [2003]*, *Yu et al. [2011]*, *Wang et al. [2004]*, *calculated to be consistent with two ilmenite transitions*, *Yu et al. [2011]*, *Saikia et al. [2008]*. The T range column lists the range of temperatures where each transition is applied. The full temperature range notation indicates no temperature restrictions are applied. Other references: *Ringwood [1991]*, *Ji and Zhao [1994]*, *Weidner and Wang [1998]*.

3.3 Rheology

The models are set up with a non-Newtonian composite rheology incorporating elasticity, viscous creep (diffusion and dislocation creep), low temperature plasticity (LTP, Peierls mechanism), and Drucker-Prager (DP) yielding. The total strain-rate is the sum of the elas-

Phase Transition	Depth [km]	γ [MPa/K]	T [K]	$\Delta\rho$ [%]	T range (K)
Basalt → eclogite	80	0	1173	18	full
Gt → CaPv + Gt	665	4.0	1662	2.06	full
Gt → Brg	720	1.3	1662	7.16	full

Table 2: **Phase transition values implemented for basaltic crust compositions.** The widths of all phase transitions listed is 5 km. The columns are the same as in Table 1. The references for γ are (in order): *Hacker and Bebout* [1996] and *Hacker et al.* [2003]; *Saikia et al.* [2008]; *Hirose* [2002]. The references of $\Delta\rho$ are (in order): *Hacker and Bebout* [1996] and *Hacker et al.* [2003]; *Saikia et al.* [2008], *Yu et al.* [2011].

tic, viscous, and plastic components:

$$\dot{\varepsilon} = \dot{\varepsilon}_{elastic} + \dot{\varepsilon}_{viscous} + \dot{\varepsilon}_{LTP} + \dot{\varepsilon}_{DP} \tag{10}$$

which can be rewritten as

$$\dot{\varepsilon} = \frac{\dot{\sigma}}{2\mu} + \frac{\sigma}{2\eta_{viscous}} + \frac{\sigma}{2\eta_{LTP}} + \frac{\sigma}{2\eta_{DP}} \tag{11}$$

where $\dot{\sigma}$ is the time derivative of the stress. To expand the $\dot{\varepsilon}_{elastic}$ term and better define $\dot{\sigma}$ the following derivation shows how the elastic time step and rotation of elastic stresses are factored into this term. First, a time derivative of the the elastic stress-strain relationship ($\sigma = 2\mu\varepsilon$) must be taken to solve for the elastic strain-rate:

$$\dot{\sigma} = 2\mu\dot{\varepsilon}_{elastic} \tag{12}$$

Since the elastic stress tensor can rotate, this needs to be accounted for with additional rotational terms. The material spin tensor, $\mathbf{W}$, tracks the stored stress tensor rotation as it is advected. Incorporating $\mathbf{W}$ and rearranging:

$$2\mu\dot{\varepsilon}_{elastic} = \dot{\sigma} + \sigma\mathbf{W} - \mathbf{W}\sigma \tag{13}$$

The right-hand side is the Jaumann stress-rate. Expanding $\dot{\sigma}$ into a finite difference over time steps of length Δt_e:

$$2\mu\dot{\varepsilon}_{elastic} = \frac{(\sigma^{t+\Delta t_e} - \sigma^t)}{\Delta t_e} + \sigma^t \mathbf{W}^t - \mathbf{W}^t \sigma^t \tag{14}$$

where $\sigma^{t+\Delta t_e}$ is the stress at the current time step, and σ^t is the stress at the previous time step. Next, multiplying both sides by Δt_e:

$$\Delta t_e 2\mu\dot{\varepsilon}_{elastic} = (\sigma^{t+\Delta t_e} - \sigma^t) + \Delta t_e(\sigma^t \mathbf{W}^t - \mathbf{W}^t \sigma^t) \tag{15}$$

After reordering and regrouping terms on the right-hand side, the first term is the stress at the current time step and the right most term, now grouped in brackets, represents the stress from the previous time step:

$$\Delta t_e 2\mu\dot{\varepsilon}_{elastic} = \sigma^{t+\Delta t_e} - [\sigma^t + \Delta t_e(\mathbf{W}^t \sigma^t - \sigma^t \mathbf{W}^t)] \tag{16}$$

The term in brackets, the stored and rotated stress from the previous time step, is simplified to $\check{\tau}_{el}^t$. The equation can be solved for the elastic strain-rate:

$$\dot{\varepsilon}_{elastic} = \frac{\sigma^{t+\Delta t_e} - \check{\tau}_{el}^t}{2\mu\Delta t_e} \tag{17}$$

Defining $\Delta t_e \mu$ as the elastic viscosity, $\eta_{elastic}$:

$$\dot{\varepsilon}_{elastic} = \frac{\sigma^{t+\Delta t_e}}{2\eta_{elastic}} - \frac{\check{\tau}_{el}^t}{2\eta_{elastic}} \tag{18}$$

After substitution and rearranging, equation 11 for the total strain-rate now takes the form:

$$\dot{\varepsilon} = \frac{\sigma^{t+\Delta t_e}}{2\eta_{viscous}} + \frac{\sigma^{t+\Delta t_e}}{2\eta_{LTP}} + \frac{\sigma^{t+\Delta t_e}}{2\eta_{DP}} + \frac{\sigma^{t+\Delta t_e}}{2\eta_{elastic}} - \frac{\check{\tau}_{el}^t}{2\eta_{elastic}} \tag{19}$$

which can be simplified as:

$$\dot{\varepsilon} = \frac{\sigma^{t+\Delta t_e}}{2\eta_{eff}} - \frac{\check{\tau}_{el}^t}{2\eta_{elastic}} \tag{20}$$

where the effective viscosity is given as

$$\eta_{eff} = \left(\frac{1}{\eta_{viscous}} + \frac{1}{\eta_{LTP}} + \frac{1}{\eta_{DP}} + \frac{1}{\eta_{elastic}} \right)^{-1} \tag{21}$$

Note that after the initial time step $\check{\tau}_{el}^t = \check{\tau}^t$, the full stress tensor from the previous time step as in equations 4 and 7.

The viscous viscosity $\eta_{viscous}$ is the harmonic average of the diffusion and dislocation creep viscosities. The viscous rheology uses wet olivine flow laws modified for a lower water content of 100 ppm appropriate to the slab interior. The flow law for diffusion and dislocation creep follow the form of Equation (22) and LTP follows the form of Equation (23):

$$\dot{\varepsilon}_{diff,dis} = 2Ad^{-m}\sigma^n \exp\left(-\frac{E+PV}{RT} \right) \tag{22}$$

$$\dot{\varepsilon}_{ltp} = A\,\sigma^n \exp\left(-\frac{E}{RT}\left(1 - \left(\frac{\sigma}{\sigma_p}\right)^p \right)^q \right) \tag{23}$$

where A is the pre-exponential constant, E is the activation energy, V is the activation volume, m is the grain size exponent, and n is the stress exponent. Additionally, in the LTP flow-law σ_p is the Peierls stress and p and q are empirical parameters. The values used for the constants of all three flow laws in our models can be found in Tables 3 and 4. Here, σ is the second invariant of the deviatoric stress tensor, temperature is T, pressure is P, grain size is d (set fixed to 0.5 cm), and R is the gas constant. As a note, in ASPECT the strain-rate dependent formulation of the rheology equations are used. The diffusion and dislocation creep equation can simply be solved for viscosity, but the LTP equation cannot be solved in this way. Instead an approximation of the LTP flow law with a temperature dependent power law exponent is used within ASPECT (M. Billen, personal comm following the approach

from *Kameyama et al.* [1999]). Dislocation creep and LTP are turned off in the lower mantle below 660 km because seismic anisotropy is not observed in the lower mantle. Both of these mechanisms are expected to to generate a lattice preferred orientation in bridgmanite which would lead to seismic anisotropy, contrary to observations.

	n	m	A* [Pa^{-n}m^{p}s^{-1}]	E [kJ/mol]	V[cm^3/mol]
Diffusion Creep	1	3	2.4536e-17	285	6.9
Diffusion Creep *Lower Mantle*	1	3	6.3318e-20	285	3
Dislocation Creep	3.5	0	3.5831e-17	502.4	12.48

Table 3: **Viscosity input parameters.** The values for n and m are taken from the wet olivine experiments of *Hirth and Kohlstedt* [2003]. The values of A* and E are modified from *Hirth and Kohlstedt* [2003]. The value of V for diffusion *Ohuchi et al.* [2012] and for dislocation *Karato and Jung* [2003] were also modified. They are modified from their original wet rheology values to account for a water correction [*Bell et al.*, 2003] and to convert to inputs for ASPECT to correctly incorporate water content [*Kohlstedt et al.*, 1996; *Keppler and Bolfan-Casanova*, 2006; *Ohuchi et al.*, 2015]. The values were recalculated to account for a lower water content of 100 pm and a grain size of 0.5 cm. The lower mantle Diffusion Creep A* value is calculated account for the 10-30x viscosity jump estimated at the upper to lower mantle boundary. The value of

	n	p	q	σ_p [Pa]	A [Pa^{-n}s^{-1}]	E [kJ/mol]	γ
LTP	2.0	0.5	1.0	5.9e9	1.49e-19	320	0.17

Table 4: **LTP input parameters.** These values are all taken from the experimental paper *Mei et al.* [2010]. Note: In the lower mantle below 660 km, the value of A is set to 1e-31 Pa^{-2}s^{-1}in order to restrict LTP to only be active in the upper mantle. In this table γ is a fitting parameter needed for the viscosity approximation formulation implemented in ASPECT described in the text.

In addition to Peierls creep as a plasticity mechanism, we also include a Drucker-Prager yield criterion (equation 24) to define a yield stress σ_y in the model at depths shallower than 200 km. Drucker-Prager is a commonly used yield criterion to account for the effects of distributed frictional fracture deformation (e.g., brittle cataclasis at shallow depths) which is pressure dependent.

$$\sigma_y = C\cos(\phi) + P\sin(\phi) \tag{24}$$

where C is cohesion, P is pressure, and ϕ is the angle of internal friction. Below 200 km depth, a constant yield stress of 1e12 Pa is set to turn off this linear plasticity and rely solely

on LTP in the deeper slab. If the viscous stress ($2\eta\dot{\varepsilon}_{ii}$) at a location becomes larger than σ_y the viscosity is reduced back to $\eta_y = \frac{\sigma_y}{2\dot{\varepsilon}_{ii}}$. The values used for the constants can be found in Table 5. The effect of restricting DP to depths $\leqslant$ 200 km is explored in test models found in Section 6.2.1.

Parameter	Value	
Cohesion	50e6 Pa	1e12 Pa
Internal Angle of Friction	25.0°	0.0°
Maximum yield stress	1e12 Pa	
Elastic shear modulus	1.2e11 Pa	
Elastic time step	2,000 years	
Grain Size	0.5e-2 m	
Adiabatic Surface Temperature	1573 K	
Minimum Viscosity	1e18 Pa·s	
Thermal diffusivity	1e-6 m^2/s	
Heat Capacity	1250 J/K/kg	
Thermal expansitivies	3.1e-5 K^{-1}	

Table 5: **Additional input parameters.** Cohesion and Internal Angle of Friction show two values. As described in the text, the yielding implementation changes at 200 km. The values on the left are used above 200 km, and the values on the right are used below. The left values when used in equation 24 lead to Drucker-Prager yielding while the right side values lead to a Von Mises criterion.

4   Location-Specific Modeling

The methods for building a location-specific model are straight-forward in that GWB is a well-developed code that can incorporate the observations for slab geometry and temperature structure as described above. An example of a location-specific setup built from present-day observations is shown for a 2D slice through the Kermadec trench (Figure 7a,b). However, there is a modeling challenge that arises from the need to preserve the present-day geometry of the subducting slab while at the same time build up the stresses and strain-rates to approximate what they would be in the present-day. In the real world, slabs subduct and evolve over millions of years to end up with their present-day stress and strain-rate conditions. Our understanding of subduction dynamics has not reached the stage in which we can set up a numerical model that starts from a proto slab and subducts millions of years to reproduce
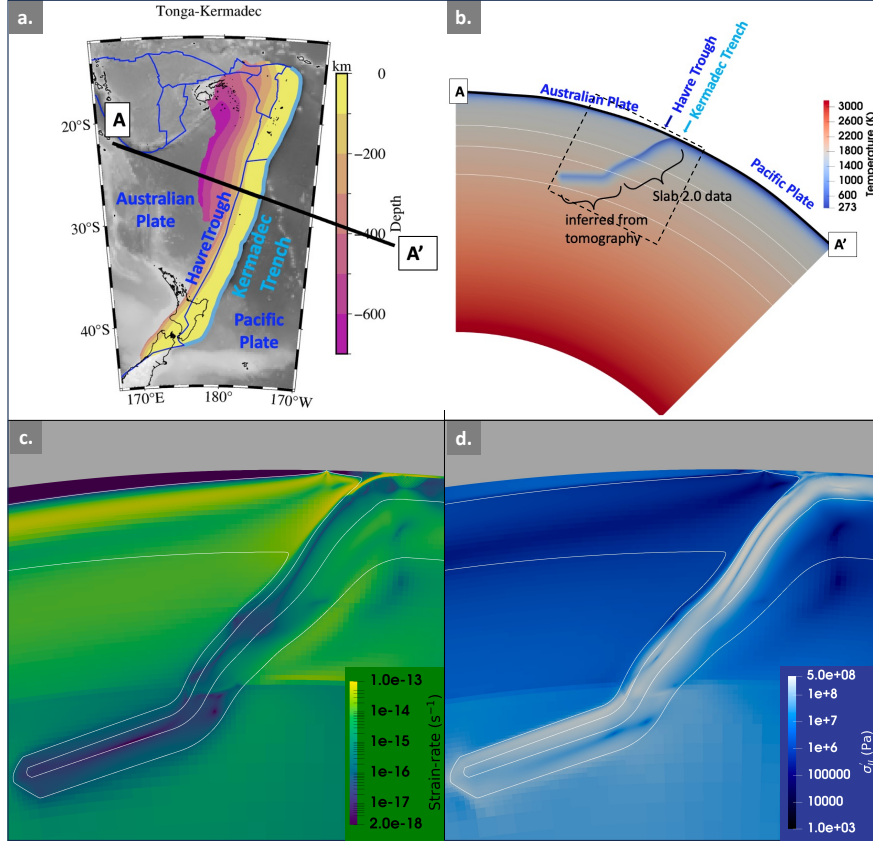
Figure 7: Location-specific Model setup for a 2D profile in the Kermadec region. (a) The colorscale shows the depth to slab data from the Slab2.0 catalog [*Hayes et al.*, 2018] over a grayscale bathymetry [*Uieda et al.*, 2023]. The royal blue lines are the simplified plate boundary geometries, with the light blue line indicating the Kermadec trench [*Bird*, 2003] The cross-section black line A-A' is the trench perpendicular profile line that the location-specific model setup shown in panel **(b)** corresponds to (Map made with PyGMT version 0.7.0 [*Uieda et al.*, 2023]). **(b)** The 2D initial temperature structure built for cross section A-A' in **(a)**. The geometry is built from the Slab2.0 data [*Hayes et al.*, 2018] and regional tomography data [*Fukao and Obayashi*, 2013]. The temperature structure is calculated using plate age (103.7 Ma Pacific Plate at the trench [*Seton et al.*, 2020]) and velocities (0.023 m/yr spreading rate at the Havre Trough [*Parson and Wright*, 1996]) in the thermal models described in Section 3.2. **c** The color scale shows the strain-rate solution after running the static model forward for 150,000 years for the 2D profile shown in (b).**d** The color scale shows the second invariant of the deviatoric stress after running the static model forward for 150,000 years for the 2D profile shown in (b). The white contours shown in (c) and (d) are the 1173 K (inner) and 1673 K (outer) temperature contours to provide a visual reference for the slab geometry that is held fixed.

the exact geometries of present-day subduction zones. Our location-specific models utilize present-day geometry and approximated temperature structures based on subduction history, but they do not include the stress and strain-rate resulting from the subduction history. Therefore, the goal was to develop a modeling workflow that allows us to preserve the

present-day geometry of the subducting slab, but also approximate the present-day stress and strain-rate magnitudes and spatial patterns within the slab.

The modeling methods developed to overcome this challenge use a short timescale model that is run forward from this initial present-day setup, as an essentially "static" model in which only the stress tensor is advected in time. That is, the geometry and driving forces remain fixed. For the remainder of the chapter, some models will be referred to as "fully dynamic" and others as "static". A fully dynamic model is run as described in the above sections where all compositional and temperature fields are solved for and advected throughout the model run. When a model is described as "static" this means that the components of the stress tensor (each of which is tracked as compositional fields in ASPECT) can advect, but all of the other compositional fields, as well as the temperature field are set to be static (i.e., are not advecting and remain constant in value and position). The Stokes flow is solved at each time step with iterations for the nonlinear rheology. Therefore the strain-rate and viscosity do evolve in time. This method of numerical simulation guarantees that the geometry and temperature structure of the slab is preserved. The model with the prescribed present-day geometry is run forward statically only for 150,000 years. This preserves the geometry and allows the stress and strain-rate solutions to develop. The results of this method applied to the Kermadec 2D profile are shown in 7c-d where there is a well resolved solution for both the stress and strain-rate.

Before taking these results from Kermadec and retesting the strain-rate constraint hypothesis (our primary goal), we first show the validity of our static modeling methods in approximating a fully dynamic solution. In the following section, we present a Proof of Concept model using a "synthetic" subduction zone to demonstrate that despite skipping the long dynamic subduction history in the location-specific static models, this modeling method provides a reasonable approximation for the deformation state that would have resulted from the fully dynamic solution.

5 Proof of Concept Modeling

5.1 Methods

To demonstrate that the location-specific static subduction modeling approach described above is a valid method, we present a Proof of Concept model. Here we will use a generic subduction model setup to demonstrate that we reproduce an accurate and complete model solution using the static method, which does not include the full history of slab deformation. To make this demonstration we will compare the stress and strain-rate from the final step of a fully dynamic model to the stress and strain-rate from a static model. The initial geometry, temperature, and composition for static model are taken from the final step of the fully dynamic slab. The workflow for the Proof of Concept model is shown in Figure 7. First in Phase 1, the model is set up to dynamically evolve to a "present-day" geometry with the history dependent stresses and strain-rates. We refer to the final geometry, temperature, and composition solutions of this model as Slab Geometry-P1. Next in Phase 2, the Slab Geometry-P1 is preserved, but the stress history that has evolved over time is removed. Finally in Phase 3, a short timescale model is set up to statically evolve the "present-day" stress and strain-rates when initiated with Slab Geometry-P1. The stresses and strain-rates of the final time step of Phase 1 and Phase 3 are then compared and evaluated for agreement. Each phase is described in more detail below. If the stress and strain-rate results from the static model (Phase 3) matches that from the final step of the fully dynamic model (Phase 1), then we have validated the static modeling approach for producing an accurate deformation result that captures the relevant time dependent stress evolution when applied to location-specific models.

5.1.1 Phase 1: Dynamic Method Approach to "Present-day" Slab Conditions

The goal of Phase 1 is to dynamically evolve "present-day" geometry and conditions in a subducting slab. The model setup described in Section 3 and shown in Figure 4 is used to
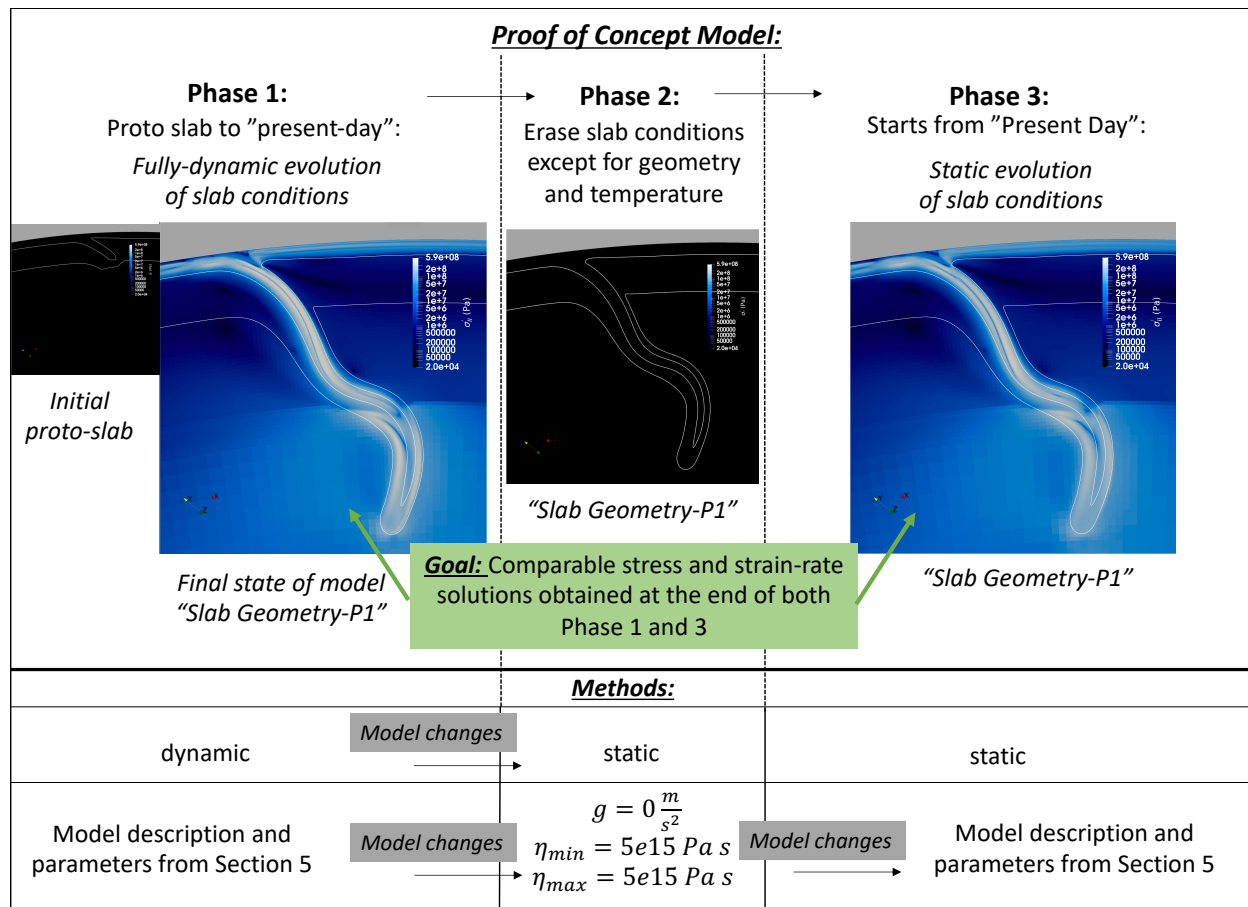
Figure 8: Schematic of Proof of Concept model workflow and methods description of each phase. See text for detailed description of Phase 1, 2, and 3 methods. The white contours indicate the 1173 K and 1673 K temperature contours. These will be used in figures through-out the chapter to provide visual references for slab geometry in various Phase 2 and 3 results and test models.

initiate this phase. Starting with a proto slab, the model is fully dynamic and runs for 10 million years to evolve its own geometry and slab conditions. Figure 9 shows the evolution from the proto slab to the final "present-day" slab (Slab Geometry-P1). Initially around 50,000 years as the slab begins to sink, there are relatively low stresses and strain-rates in the sinking portion, with higher stresses and strain-rates found at the hinge near the trench (9a,e). Yielding in the outer rise has developed as a result of DP (9e). As the slab continues to subduct through the mantle transition zone, higher stresses build up within the slab as it meets the resisting force of the higher viscosity lower mantle (9b). The density contrasts in the slab that evolve due to phase transitions lead to variable stresses and strain-rates within

the slab as it sinks through the transition zone. After penetrating the lower mantle, the regions of higher and lower strain-rates continue to evolve as more pronounced slab bending and unbending becomes visible throughout the transition zone (9f-h). Shear bands begin to develop by in the deeper slab has started by 2.5 My as well (9f). There is also significant trench retreat observed at the surface by 7.5 My (9h). By 10 My, a dynamically evolved slab geometry with spatially variable stress and strain-rate magnitudes has emerged including a well-developed neutral plane in the stress and strain-rate solutions (9d,h). Also note the presence of shear bands indicating localized yielding in the outer rise region and in the deep slab (9h). This final state of this model (9d,h) is now taken as the known history-dependent deformation state of the slab. This is the result that we want to be able to reproduce using the static model approach. Note that for real slabs we never know the true history-dependent deformation state. The white temperature contours in Figure 9d,h are representative of Slab Geometry-P1 which will be used to initiate Phase 2. A checkpoint is set at the end of this run-time that preserves the full solution in a way that a model can be restarted from this point.

5.1.2 Phase 2: Removing "Present-day" Stress State of the Slab

The goal of Phase 2 is to preserve the "present-day" geometry, temperature, and composition of the slab from Phase 1 (Slab Geometry-P1), but remove the stress history that has evolved over time. The result of this phase is then analogous to the initial conditions for the location-specific models (e.g., the Kermadec example in Section 4). Initially the Phase 2 model calls upon the checkpoint set at the end of Phase 1 that preserves all the results of the model run described in the above section. Unfortunately there is not an easy way to reset the stress tensor components to zero when restarting from a checkpoint in ASPECT. Therefore, to arrive at this initial condition for the Proof of Concept static model, we need to relax the stress back down to essentially zero, without changing anything else.

To relax the stresses we have developed an approach using physical principles and the
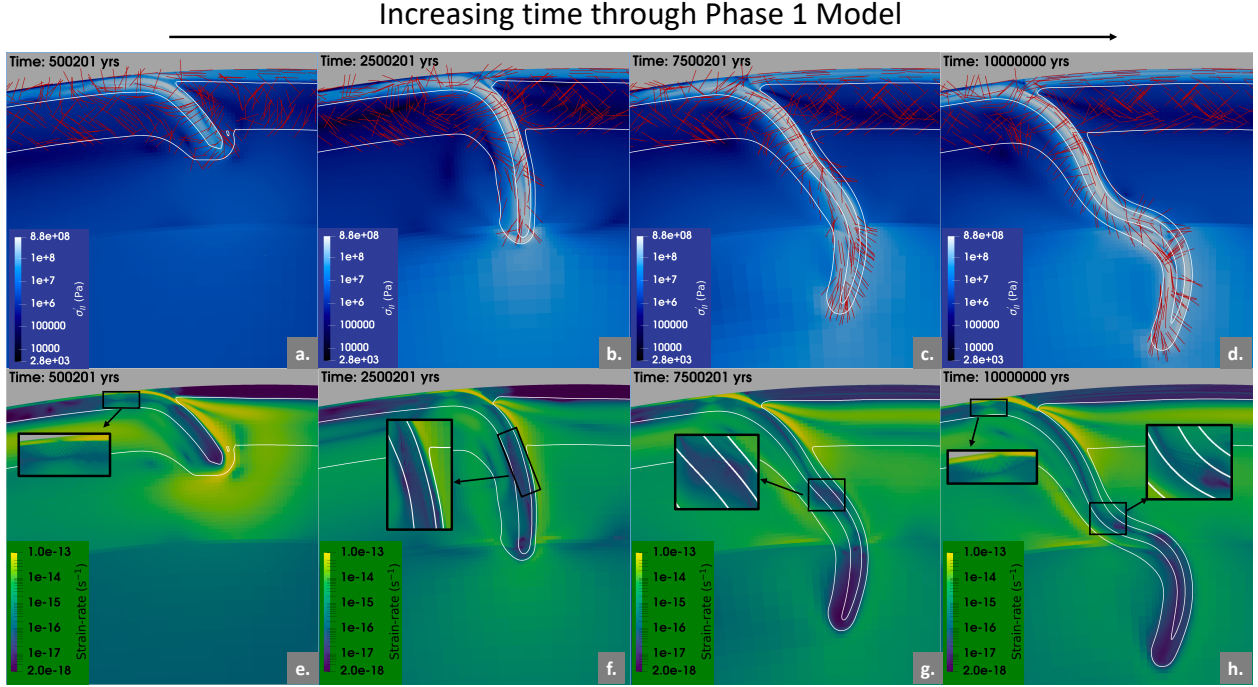
Figure 9: Evolution of geometry, stress, and strain-rate during Phase 1. Panels (a) - (d) show the second invariant of the deviatoric stress at the indicated time steps. The red lines are the computed principal tension axes, σ_3 axes. Panels (e)-(h) show the strain-rate at the indicated time steps. The black rectangles show the locations of the insets zooming in on where shear band development occurs. The white temperature contours are a visual guide for tracking slab geometry as it evolves during Phase 1.

"static" modeling approach. In order to reduce the elastic stresses to near-zero, we rely on two physical principles. The first is that elastic deformation is recoverable. When a force is applied to a perfectly elastic material, it only remains deformed and stores any accumulated stresses while the force is being applied or held. Once the force is removed, the deformation is recovered instantly. However, in a visco-elastic medium, some of the deformation is recovered immediately when a force is removed, but because there is a viscous component of the rheology, this is not instantaneous. We can make this relaxation process faster by using a lower viscosity (i.e., smaller Maxwell time $\alpha = \frac{\eta}{\mu}$). The second principle we rely on is that the subduction models are dynamic models, and that the driving forces are the buoyancy forces. In the equation 6, this is incorporated in $\vec{f}^{t+\Delta t_e}$, and is a product of density and gravity. If the gravitational acceleration in the model is changed from 9.81 m/s^2 to 0 m/s^2, the buoyancy force term is removed. We can use this second principle to remove the driving

60

force and allow visco-elastic relaxation to occur.
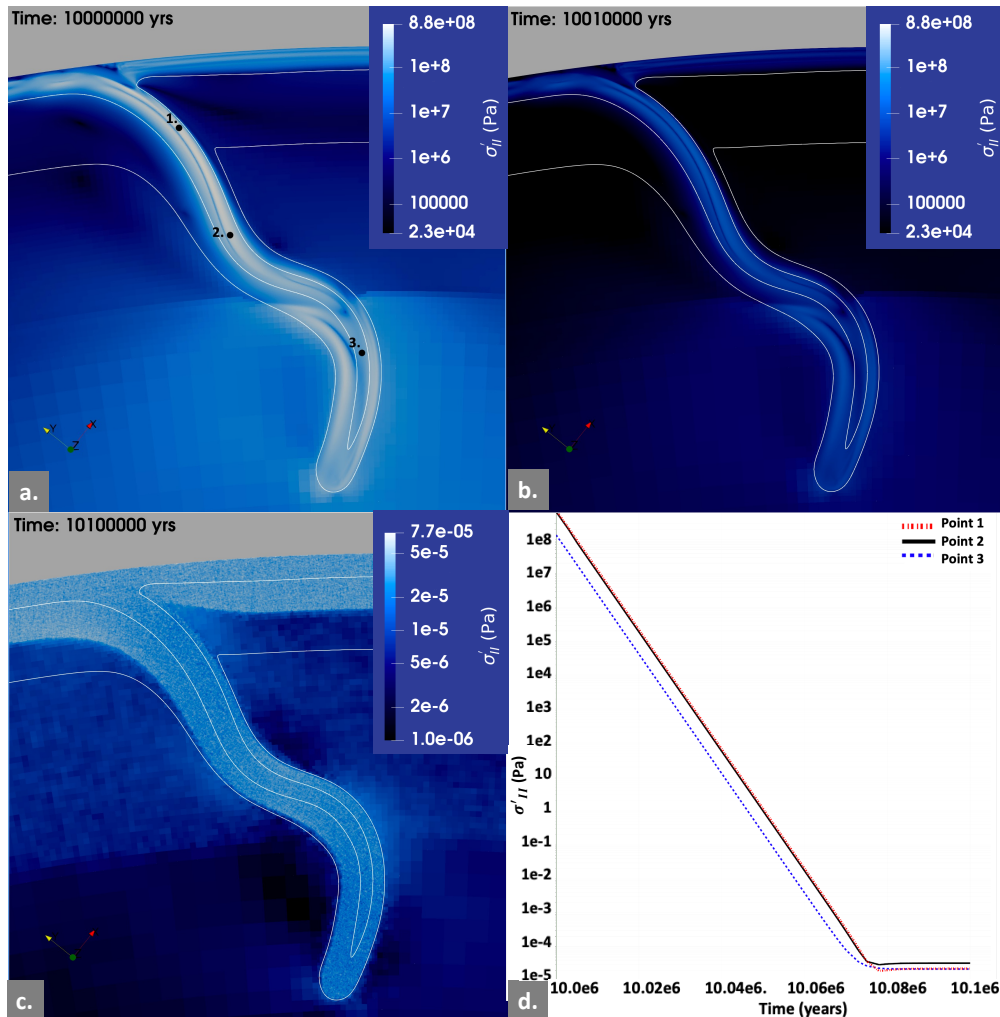
Figure 10: Phase 2: Relaxation of the visco-elastic stresses. The first three panels **(A-C)** each show a time step from Phase 2 of the second invariant of the deviatoric stress. Panel **(A)** is the starting stress solution that evolved during Phase 1. Panel **(B)** is the stress solution 1e4 years into the Phase 2 model run. Panel **(C)** is the stress solution at the end of Phase 2 (1e5 years of run time). The colorscale has been altered in this panel to highlight both the very low magnitude of stresses relative to **(A)** and **(B)** as well as the lack of any residual pattern in the stress solution that resembles the solution evolved during Phase 1 (compare with**(A)**). **(D)** The second invariant of the deviatoric stress as a function of time for three points within the slab (labeled in Panel A) showing the example decay behavior to a relatively constant low value on the order of 1e-4 Pa by the end of the model run.

Finally, putting these two principles together, we can run the model, with gravity off, using the static method to relax away the stored elastic stresses. In order to avoid numerical complications, we set the minimum and maximum viscosities of the model to be the same value of 5e15 Pa·s. This value allows for rapid visco-elastic relaxation while avoiding con-

61

vergence issues in the Stokes solver (See Section 6.2.2 for tests of different viscosity values implemented here). The model only needs to be run a short time to relax the elastic stresses down to essentially zero. Figure 10 shows how the stresses relax away during Phase 2 over 100,000 years. The initial stress inherited from Phase 1 is present at the start of Phase 2 (Figure 10a). Note the maximum stress of 8.8e8 Pa in the slab, and the minimum stress in the surrounding area of 2.3e4 Pa. After 10,000 years, the maximum stress in the slab is about 1.6e7 Pa and the minimum stress in the surrounding area is about 6.9e3 Pa (Figure 10b). Finally, after 100,000 years, the maximum stress in the slab has decreased to only 7.7e-5 Pa with the minimum stress in the surrounding area at 6.6e-7 Pa (Figure 10c). By the end of Phase 2 the spatial variability of the stress magnitudes within the slab appears random and contains none of the dynamically evolved stress pattern or structure from Phase 1. For example, there is no trace of the neutral plane or regions of high or low stress in the slab. A checkpoint is again set at the end of this phase allowing us to preserve the Slab Geometry-P1 solution (geometry, temperature, composition), but now with no initial stresses. We refer to this model state as P2.

5.1.3   Phase 3: Static Method Approach to Present-day Slab Conditions

The goal of Phase 3 is to run a short timescale model set up to statically evolve the "present-day" stress and strain-rates when initiated with a "present-day" geometry from Phase 2. Phase 3 is the identical approach used for the modeling of location-specific models (e.g., Kermadec in Figure 7b). The only difference is that we use the "synthetic" model state P2 to produce the initial conditions for the "present-day" location-specific slab. The Phase 3 model calls upon a checkpoint set at the end of Phase 2. As we want to continue to preserve Slab Geometry-P1, we again run this phase following the static setup described in Section 4. In contrast to Phase 2, we now want the elastic stresses to build back-up so we need to run a model where the buoyancy force term is nonzero. To do this we turn gravity back on by setting the gravitational acceleration in the model back to 9.81 m/s^2. Additionally, we

restore the minimum and maximum viscosity values back to their original values from the Phase 1 model setup.
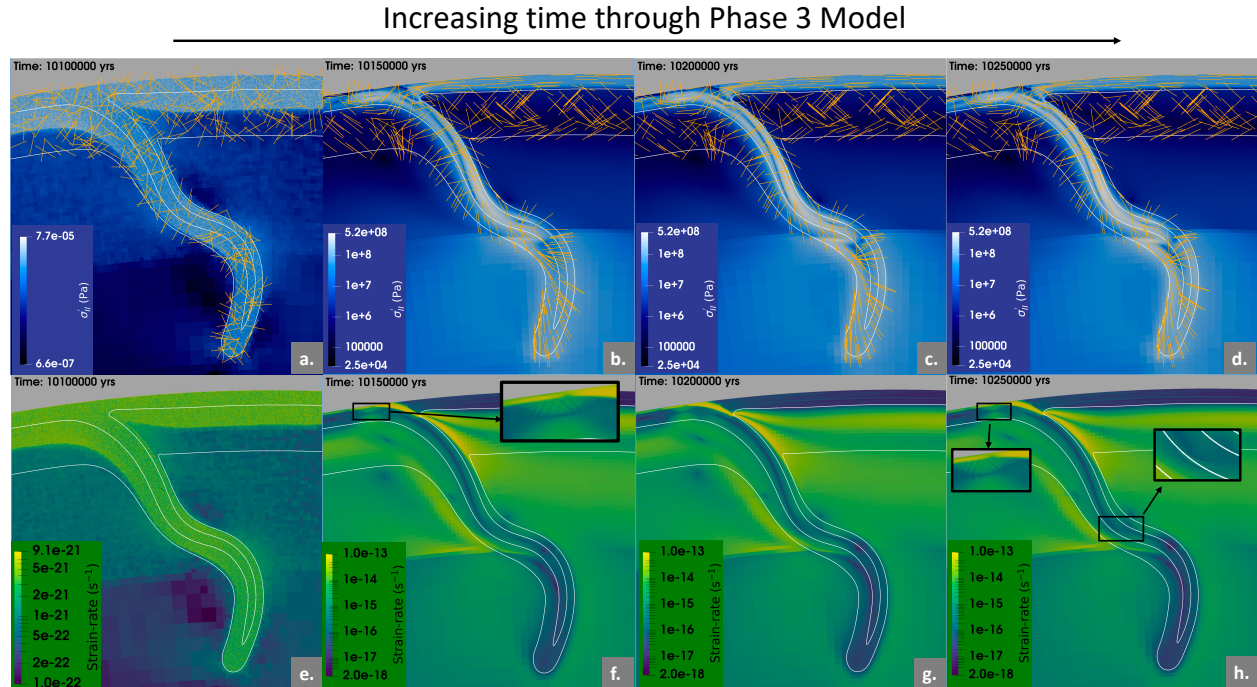
Figure 11: Evolution of stress and strain-rate during Phase 3. Panels (a) - (d) show the second invariant of the deviatoric stress at the indicated time steps. The orange lines are the computed σ_3 axes. Note the color scale is different in (a), but the same for (b-d). Panels (e)-(h) show the strain-rate at the indicated time steps. Note the color scale is different in (e), but the same for (f-h). The black rectangles show the locations of the insets zooming in on where shear band development occurs. The white temperature contours are a visual guide for showing the slab geometry that stays fixed during Phase 3.

The Phase 3 model is run for 150,000 years to build up the "present-day" stresses and strain-rates as shown in Figure 11. After running statically for only 50,000 years the stresses have already increased to values on the order of 100 GPa in some locations within the slab and there is also a noticeable neutral plane forming (11b). The σ_3 axes orientations have noticeably changed as well between (11a) and (11b). Within these first 50,000 years the development of shallow shear bands at the surface has already occurred as well (11f). At this time step the strain-rate solution already also reveals some of the expected high and low regions based on where the slab is bending and unbending through the mantle transition zone (11f). This continues to develop and become more defined over the next 50,000 years (11g). The pattern of stress magnitude also becomes more refined (11c). The boundaries

63

between high and low stress, particularly visible along the neutral plane, become sharper and areas of high stress appear to continue to increase (11c). By the final time step shear bands have begun to develop in the transition zone in a region of lower strain-rate (11h). The stress continues to evolve minimally, and the high-low stress region boundaries continue to sharpen (11d). The σ_3 axes orientations also shifted slightly going from (11c) to (11d), but have become fairly stable in orientation direction.

Overall, the biggest change in stress magnitude happens within the first 50,000 year window between (11a) and (11b). After this, the stress magnitudes change more slowly with the main changes occurring where the boundaries between high and low stress regions sharpen. The σ_3 axes also become considerably stable at this point and don't change much between the last two panels.
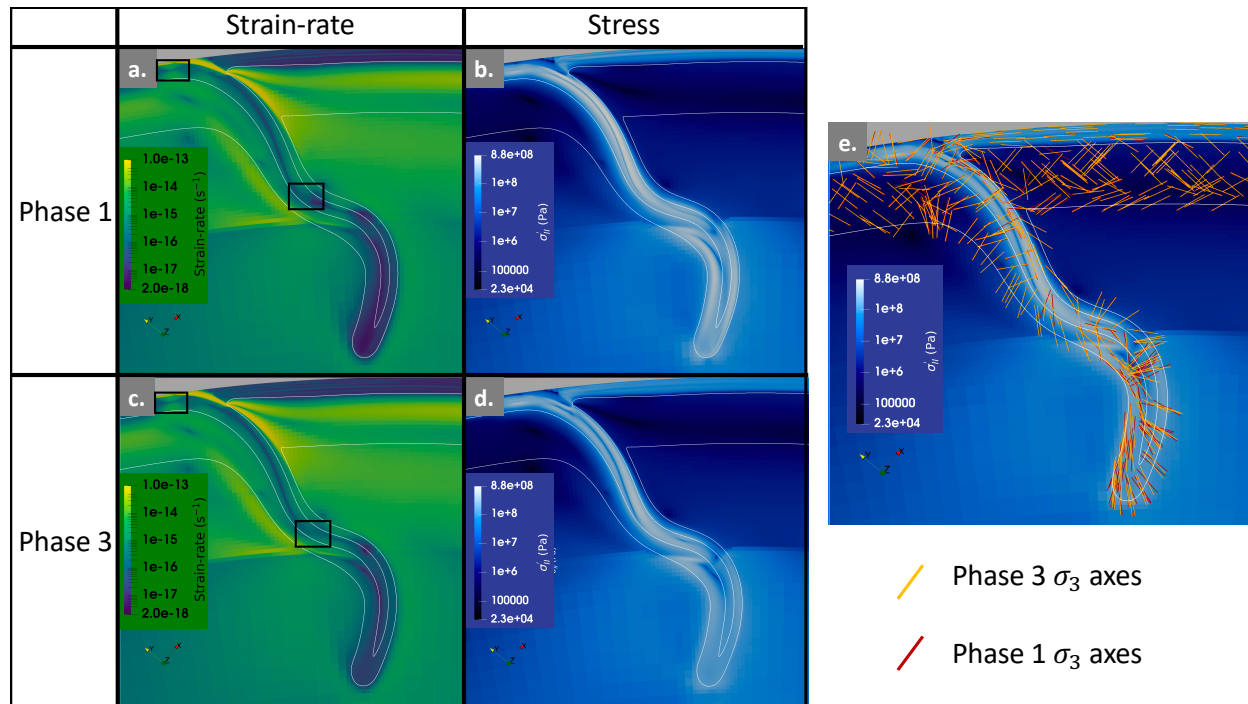
Figure 12: Agreement between strain-rate and stress solutions of Phase 1 and Phase 3. Strain-rate solution at the ends of **(a)** Phase 1 and **(c)** Phase 3. The black rectangles highlight regions of shear band development (See Figures 9h and 11h for insets). second invariant of the deviatoric stress solution at the ends of **(b)** Phase 1 **(d)** Phase 3. **(e)** The computed σ_3 axes at the end of Phase 3 *(orange)* and those computed at the end of Phase 1 *(red)* plotted on top of the image from (d). The σ_3 axes are only shown inside of the 1673 K contour (focuses on the slab).

64

5.2   Results: Comparing Phase 1 and Phase 3

Returning to the goal of the Proof of Concept model, the stress and strain-rate solution fields as well as principle stress orientations at the end of Phase 3 are compared to those calculated at the end of Phase 1. The comparison of Phase 1 and Phase 3 does reveal good agreement between their stress and strain-rate solutions (Figure 12), indicating the validity of our present-day geometry static modeling methods. The broad spatial patterns of high and low strain-rate regions that evolved through time in Phase 1 (Figure 12a) is reproduced in the short time that Phase 3 is run (Figure 12c). Some smaller scale features such as shear bands visible in the strain-rate solutions in the shallow outer rise region and in the transition zone are also reproduced. Similarly, the broad spatial pattern of stress magnitudes at the end of Phase 1 (Figure 12b) are reproduced in Phase 3 (Figure 12d). Finally, principal stress orientations are compared between the two phases by overlaying the computed principal tension directions (σ_3 axes) for Phase 1 and 3 (Figure 12e). Within the upper mantle, there is very good agreement between the σ_3 axes of Phase 1 and 3, with the orientations being identical in most locations throughout the transition zone. There is some disagreement in the lower mantle, but that area is not a focus for these models because there are no observations from seismicity in the lower mantle with which to compare model results.

This agreement shows that the method proposed for location-specific modeling using present-day slab geometries and static modeling methods is valid for calculating present-day slab conditions even when missing the subduction history of the slab. The present-day shape and density structure of the slab are a product of this history (relies on the slab morphology and temperature structure), and drive the force balance, so it is expected that these can be used to reasonably approximate the stresses. This is illustrated very clearly in Figure 13 which shows how the density and density differences (driving the model) are the same between the two phases. As a result, the velocity vectors at the end of Phase 1 and Phase 3 are almost identical. In addition, the fact that agreement between Phase 1 and Phase 3 is reached in ~150,000 years demonstrates that for the material properties and driving

forces present in the subduction models, the present stress-state is only sensitive to recent deformation on these short time scales and does not depend on the earlier history.

5.3 Discussion

5.3.1 Phase 3 results:

The observed stress and strain-rate evolution during Phase 3 is expected based on the visco-elastic-plastic rheology outlined in Section 3.3. In equation 21 the effective viscosity is shown as the harmonic average of the visco-plastic and elastic viscosities. The elastic viscosity is $\sim 1e21$ Pa·s, which is smaller than the visco-plastic viscosity ($> 1e23$ Pa·s), making it the dominant (weaker) deformation mechanism. Therefore, the initial stress state in the slab of the first time step (dt=1000 years) is primarily due to the elastic response. Due to the static nature of the model, the density structure, and therefore the driving buoyancy forces, does not change (Figure 13). This means that the applied stress in each time step does not change. However, the advected and rotated stress tensor components do evolve as part of the static method. The stress calculated at the end of each time step in a location in the model is based on both this stress from the current applied forces (not changing) and the stresses from the previous time step (equation 19). The deformation state after the initial elastic response then evolves as the visco-plastic components deform and the elastic stresses are advected. In each time step, there is a redistribution of deformation among the viscous, elastic, and plastic mechanisms.

The changes in the stress field seen in Figures 11a-d are due to how the deformation is partitioned between the deformation mechanisms (viscous, elastic, plastic) and the spatial variability in the stress-state. This process leads to increasing stresses in some areas and decreasing stress in others, as well as an overall sharpening of the high and low stress regions. This behavior is expected due to the nonlinear visco-plastic rheology. If LTP is the dominant visco-plastic mechanism in the slab, it will lead to higher stresses in a region with higher strain-rates and lower stress in a region with lower strain-rates. It is also expected with a shift

in time from elastic to elastic-plastic deformation as the model runs, that the boundaries between high and low stress regions should become steeper/sharper based on analytical solutions to the elastic-perfectly plastic bending beam problem [*Turcotte et al.*, 1978].
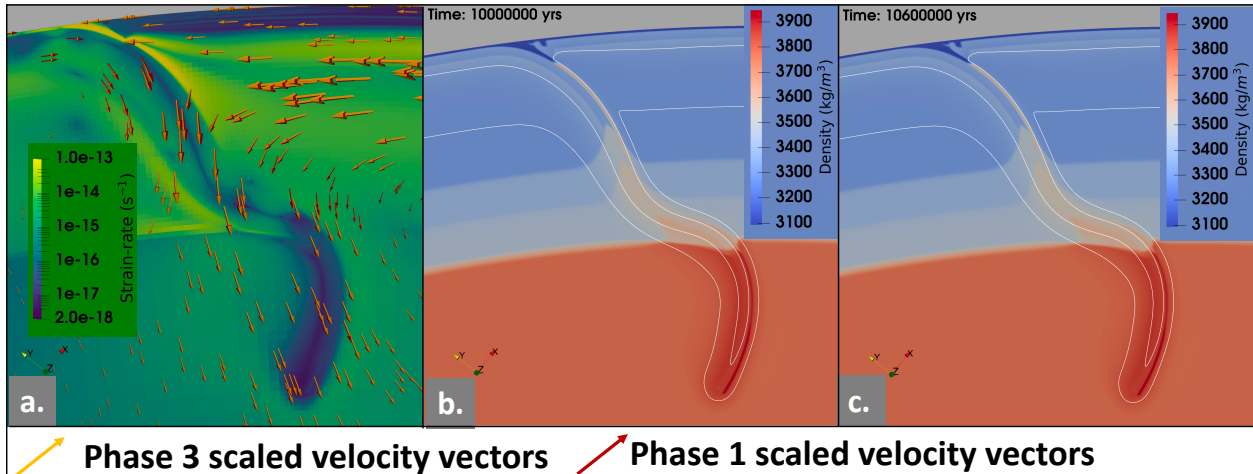
Figure 13: Matching density structures and flow field solutions between Phase 1 and Phase 3. (a) The scaled velocity vectors indicating the flow field at the end of Phase 3 *(orange)* and at the end of Phase 1 *(red)* illustrating the almost identical velocity solutions. The background is the image from Figure 12a. Panels **(b)** and **(c)** are showing preservation of the slab morphology throughout the proof of concept from the end of Phase 1 **(b)** through to the end of Phase 3 **(c)** leads to identical density structures, which are driving the force balance within the numerical simulation.

5.3.2   Length of a Static Model Run

The fact that the full history of subduction is not needed to reproduce the deformation state from Phase 1 in Phase 3 is expected from previous models and the fact that the slab is deforming slowly. First, for the highly viscous slab, as previously stated the elastic component has a lower "elastic viscosity". Therefore the elastic component responds immediately to any changes in the overall stress-state while the viscous component deforms more slowly. This means that at each time-step, any changes in the stress-state are accommodated immediately so we do not need a long history to evolve and capture the present-day stress state. However, there are regions in the slab at its boundaries where the visco-plastic components move at a similar rate to the elastic component. The increasing temperatures near the slab edges lead to lower visco-plastic viscosities (i.e., decreasing the difference between η_{visc} and $\eta_{elastic}$ and increasing the role visco-plastic deformation contributes). In these places we need to
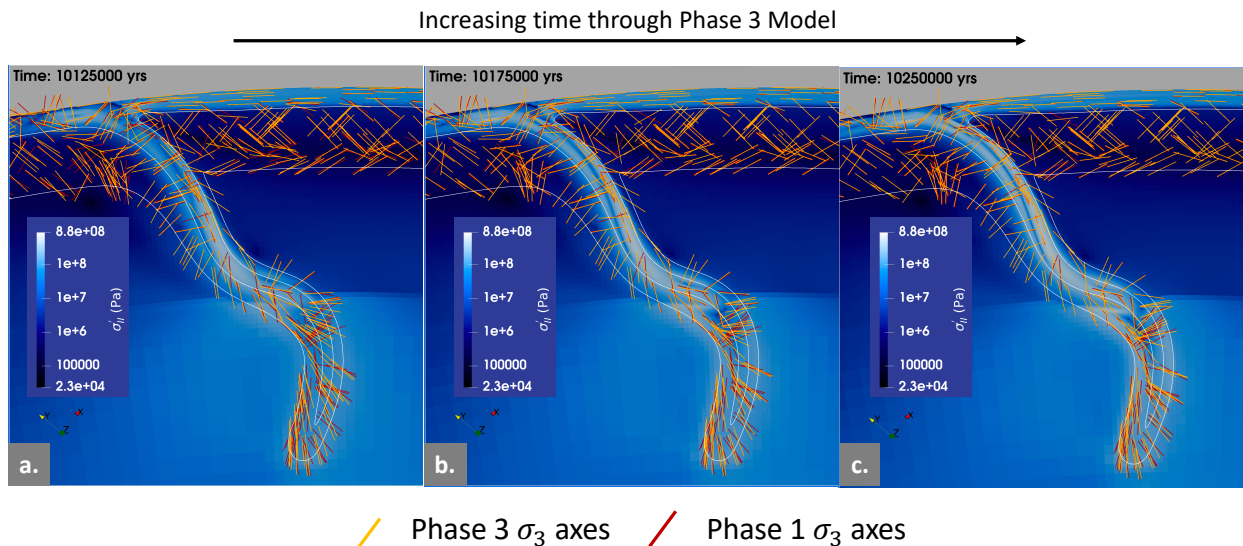
Figure 14: Convergence of σ_3 axes Phase 3 and Phase 1 solutions. In all three panels the σ_3 axes for Phase 3 are plotted at the time step indicated on-top *(orange)* of the σ_3 axes that were computed at the final time step of Phase 1 *(red)*. These are plotted on top of the second invariant of the deviatoric stress solution calculated at the indicated time step of Phase 3 in each panel. The σ_3 axes orientation comparisons at are done during Phase 3 at **(a)** 25,000 years into the run, **(b)** 50,000 years into the run, and finally at **(c)** 150,000 years (the end of Phase 3). Note: The times indicated in the panels are cumulative run times and Phase 3 began at time 10,100,000 years.

account for the deformation accommodated by viscous components and how that affects surrounding regions. The Proof of Concept model shows that an an appropriate timescale for these considerations is about 150,000 years.

The decision to run the static models for 150,000 years is based on a few different observations of model behavior and how the visco-elasticity is implemented in ASPECT as described in Sections 3.3 and 5.1.3. The length of time the static Phase 3 model needs to run is a balance between 1) the time for the visco-plastic deformation to occur and 2) the distance the stress tensor is advecting. Therefore, the choice of run time is a balance of needing to run the models long enough to allow for visco-plastic flow, but not so long that the solution is advected too far spatially relative to the fixed slab geometry. Section 5.2 already showed that by 150,000 years of run time, the overall spatial pattern of high and low strain-rates and stress magnitudes has emerged from the instantaneous elastic solution (Figure 12). The temporal evolution of the Phase 3 σ_3 axes orientations in comparison to the Phase 1 σ_3

axes is shown in Figure 14. There is progressive improvement in the agreement between the two solutions by 150,000 years. This is expected following the description of the static visco-elastic behavior described in Section 5.1.3. Initially in Figure 14a, the first graphical output shows some misalignment between the Phase 1 and Phase 3 σ_3 axes. It is known that elastic, visco-elastic, and viscous calculated principle stresses are not expected to be coaxial. The Phase 1 σ_3 axes are a product of dynamic visco-elastic-plastic deformation. In Phase 3, at this first graphical output, the model is still in phase of redistributing deformation among visco-plastic deformation mechanisms. Moving forward through Phase 3 (Figure 14a-c) the solution is progressively moving from σ_3 axes calculated from dominantly elastic deformation, to the σ_3 axes calculated from visco-elastic-plastic distributed deformation. By the time 150,000 years of run time is reached, the very good orientation agreement of the σ_3 axes between the fully dynamic and static solutions suggest that a reasonable distribution amongst the visco-elastic-plastic deformation mechanisms has been reached in the static model (Figure 14c).

Most of the changes we observed in the stress and strain-rate solutions as well as the σ_3 axes orientations beyond 150,000 years occur in the lower mantle. These observations are expected based on the description of the static visco-elastic behavior described in Section 5.1.3. The viscosity is higher in the lower mantle, and the strain-rates lower, so the redistribution of deformation among all of the deformation mechanisms would occur at a slower rate. This region needs more time to "equilibrate" to a steady solution than that the more quickly deforming upper mantle portion of the slab. Due to the lack of observed deep earthquakes in the lower mantle portion of the slab we are not as interested in the conditions in this region and do not plan to use these computed lower mantle stress orientations in our analyses. Qualitatively, all of these reasons suggest that running the model 150,000 years is sufficiently long for the purposes of our study.

A specific point by point comparison helps illustrate quantitative details of the static slab evolution and this decision. The dashed lines in Figure 15c represent the stress magnitude
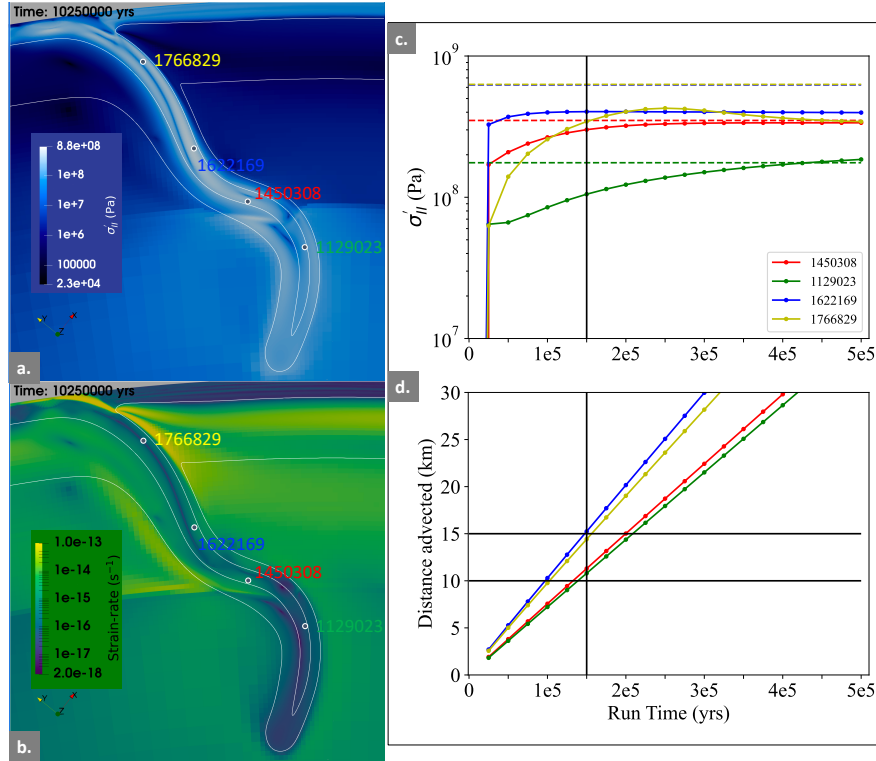
Figure 15: Individual point evolution of stress in Phase 3 and illustrating the cut-off time choice for Phase 3 static methods. Panels **(a)** and **(b)** show the second invariant of the deviatoric stress and strain-rate solutions, respectively, at the end of Phase 3. **(c)** The evolution of the second invariant of the deviatoric stress as a function of run time during Phase 3 for four selected points plotted in (a) and (b) (solid colored lines). For each point, in it's matching color, we have also plotted the value of the second invariant of the deviatoric stress at the end of Phase 1 (dashed colored lines). **(d)**Distance advected as a function of time for each of the same four points plotted in (c). See text for more details on how this is calculated. The horizontal black solid lines are just for reference at 10 km and 15 km distance values. The vertical black solid line in (c) and (d) indicates a run time of 150,000 years, where we decided to cut-off the Phase 3 model and pull results from.

that was reached for four different points in the slab at the end of Phase 1. In the corresponding color but shown with solid lines, the build up of stress during the Phase 3 is shown for the same points. This illustrates two key things. The first, is that the stresses build up to a relatively "steady" value of stress in the static solution fairly quickly. Recall, the initial large stress build-up is elastic, followed by smaller changes according to the redistribution of deformation amongst all of the visco-elastic-plastic components. The initial large stress increase due to the elastic response locks in the larger pattern we see in the stress solution field and sets the magnitude of stress in the slab (Figure 11). The second, is that within

150,000 years, for each individual point, we get within almost half an order of magnitude of the Phase 1 stress value during Phase 3 with some points being within a factor of 2. This is also a more quantitative validation of the Section 5.2 argument that the static modeling method (Phase 3) is a valid approximation for a fully dynamic solution (Phase 1). However, it does point out that the stress magnitudes at this point are lower bounds, and could be a factor of 2-5 times higher.

As described in the static modeling methodology, the stress tensor, components tracked as compositional fields are the only variables that are allowed to advect while the slab geometry is held fixed. This brings up the concern that in our static methods we would be building up stresses in one location, but advecting them to another location. Figure 15d shows distance advected as a function of time for the same four points analyzed in the stress comparison. The plot shows that as time increases, so does the distance material is advected. The velocities at these points in the slab are representative of the range of velocities found in the slab. By stopping the Phase 3 model at 150,000 years, advection of the stress tensor is limited to $\sim$ 10-15 km at a maximum, which is comparable to the upper bound of location errors for observed intermediate and deep earthquakes (e.g., Global Centroid-Moment Tensor (CMT) project [*Ekström et al.*, 2012; *Dziewonski et al.*, 1981; *Ekström and Nettles*, 1997; *Huang and Okal*, 1998; *Chen et al.*, 2001]. Therefore, we conclude that for the purposes of comparing to observations the method is sufficiently accurate with respect to location, but also the results should not be over-interpreted at length scales less than 10-15 km.

We have now shown and discussed that the methods proposed for location-specific modeling using present-day slab geometries and static modeling methods are valid and provide an accurate representation of the stress and strain-rate in a visco-elastic-plastic slab. Therefore, they will be used moving forward in retesting the strain-rate constraint hypothesis in Section 7 where we return to the Kermadec modeling results shown in Section 4. The following section (Section 6) first goes into the details of the static modeling method choices.

6   Test models: Exploring modeling decisions and parameter choices

6.1   Dynamic versus Static Model (Phase 3)

As described in the methods section above Phase 3 is run using the static method. Recall, this is also the method that will be used for future location-specific models. Here we show an example of a Phase 3 run using a fully dynamic model compared to the static modeling method. Although it is only run for 150,000 years, the morphology of the slab in the dynamic model does begin to change. Figure 16 shows the offset between temperature contours plotted for the dynamic slab compared to the static slab. The scaled velocity vectors for both the static and the dynamic models are also plotted in Figure 16. As expected for the dynamic slab, the flow field has begun to deviate from the static model flow field (larger effects of this highlighted in red boxes). As the slab dynamically subducts, the density structure and force balances change from what they are at present day and will change the stress and strain-rate calculations. The effects of running the model dynamically versus statically for this short timescale are relatively small. Importantly, using the static method guarantees that that slab morphology does not change from the present-day, making comparison to present-day observations easier to interpret.
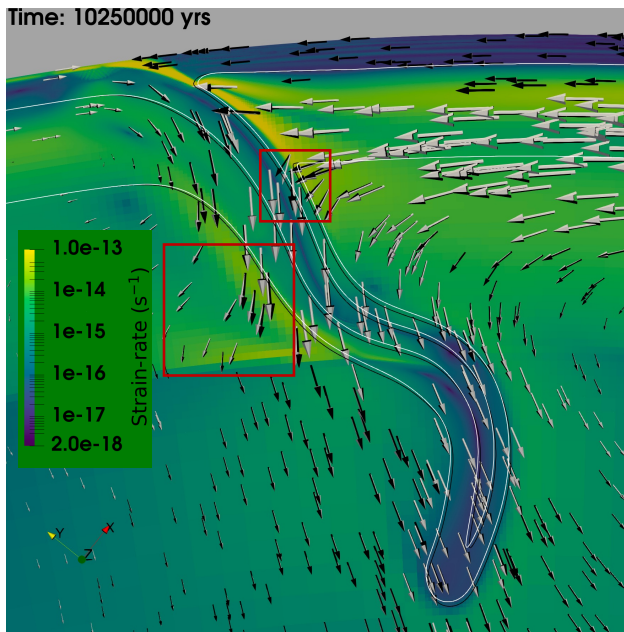
Figure 16: Comparison of Dynamic Phase 3 and Static Phase 3 modeling methods. The white temperature contours and white scaled velocity vectors are calculated for the Phase 3 static reference model. The black temperature contours and black scaled velocity vectors are calculated for the Phase 3 dynamic test modesl. As in all other figures, the temperature contours are 1173 K and 1673 K. These are plotted on top of the static model strain-rate solution at the indicated time. See text for descriptions of red boxes.

6.2 Testing model parameter choices

All of the static models in this section are run to 500,000 years to simplify the comparison of test models by removing the effects of variable model run time. The fully dynamic models are run for 5 My.

6.2.1 Tests of Yielding Implementation (Phases 1 and 3)

In their visco-plastic models, *Billen* [2020] used Byerlee's law at shallow depths up at 80 km, and then used a constant yield stress of 1 GPa for the deeper the slab. They hypothesized that the incorporation of LTP rather than a constant yield stress or yield criterion would lead to higher strain-rates in the high stress, cold regions of the slab and could also affect how the slab deforms as it subducts. As described above the rheology implemented here includes both Drucker-Prager (DP) yielding as well as a Peierls low-temperature plasticity (LTP). Each mechanism leads to yielding under different conditions and is relevant in different portions of the slab. Because DP is used to capture pressure-dependent brittle deformation it is expected to be the dominant (weakest) yielding mechanism at shallower depths. LTP is expected to be dominant in the cold, interior of the slab as it is subducting. To ensure the proper implementation of DP (shallow) and LTP (deep) we ran several models to determine if DP needed to be explicitly limited in depth.

In this section we present a suite of models to show how including or not including these two plasticity criterion affects the model behavior focusing on changes to slab morphology (Phase 1) and strain-rate magnitudes and patterns (Phase 1 and 3). LTP is simply turned on or off, and DP is either on, off, or only on at depths shallower than 200 km. Table 6 describes how these options are combined in six different models which are all identical except for how their yielding mechanisms are implemented. When DP is listed as "off", a Von Mises yield criterion of $\sigma_y = 1e12$ Pa is implemented at all depths of the model. This effectively removes a yield stress as we do not expect the stress in the model to ever reach this high value. Additionally, in the models where DP is only on at depths $\leqslant 200$ km, this same Von Mises

Model name	DP	LTP	P1 Results	P3 Results
Ref Model	depths $\leqslant$ 200 km	on	-	S/D shear bands
YT1	all depths	off	lowest slab $\dot{\varepsilon}$, strong slab	S/D shear bands
YT2	all depths	on	highest slab $\dot{\varepsilon}$, weakest slab	S/D shear bands
YT3	off	on	highest slab curvature (no S yielding)	D shear bands
YT4	depths $\leqslant$ 200 km	off	failed: too stiff slab, too high $\vec{\mathbf{u}}$	S/D shear bands
YT5	off	off	failed: too stiff slab, too high $\vec{\mathbf{u}}$	no shear bands

Table 6: **Yielding Tests carried out for Phase 1 and Phase 3 models.** Table indicates how DP and LTP are implemented in each test. The P1 Results column notes the significant finding for each test in relation to the Ref Model. The P3 Results column indicates the significant findings for each test in terms of the shear band development at shallow (S) and deep (D) depths. Red text color indicates that the shear bands in this depth regime should not have developed based on our physical understanding of the implemented DP/LTP set up for that test (See text for details and corresponding red boxes in Figure 19e).

criterion is used in the remaining depths of the model. Ref Model is the model used in the Proof of Concept section described above and is the preferred yielding implementation for future models. The same five test models (YT1-YT5) are run for Phase 1 and Phase 3.

Phase 1   The Phase 1 yielding tests reveal important effects of different yielding implementations. The test models in this section are run for 5 My and compared to the Phase 1 Ref Model time step at ~5 My. YT1 compared to the Ref model illustrates the effect of solely implementing a yield criterion like DP instead of LTP. The morphology of the Ref Model and YT1 slabs are relatively similar (Figure 17a,d). The Ref Model shows higher strain-rates in the high stress, cold region of the slab, verifying the hypothesized effect of implementing LTP rather than a yield criterion at depth [*Billen*, 2020]. Models YT2 and YT3 compared to the Ref model illustrate the effect of changing the DP implementation (they both have LTP on).

When DP is turned on at all depths (YT2), there is a very different morphology compared to the Ref Model (Figure 17a,b). The combination of DP and LTP leads to an overall weaker slab that is yielding by both mechanisms. When DP is turned off at all depths (YT3), there is also a different morphology compared to the Ref Model (Figure 17a,c). Despite LTP being on, the subducting plate at the surface does not yield as much without DP turned on since it is not a region where LTP would be the dominant deformation mechanism. The absence of shear bands in YT3 compared to the Ref Model (and other test models) as indicated by the black box, shows this lack of DP yielding in the outer rise. This absence of shear bands contradicts observations of outer rise faulting in subduction zones. This supports the implementation of DP at shallow depths in the slab. The effect of changing LTP (on or off) on affecting the morphology of the slab was expected based on prior studies that have tested different yield strength criterions in comparison to LTP and found LTP to lead to weaker slabs [*Garel et al.*, 2014].
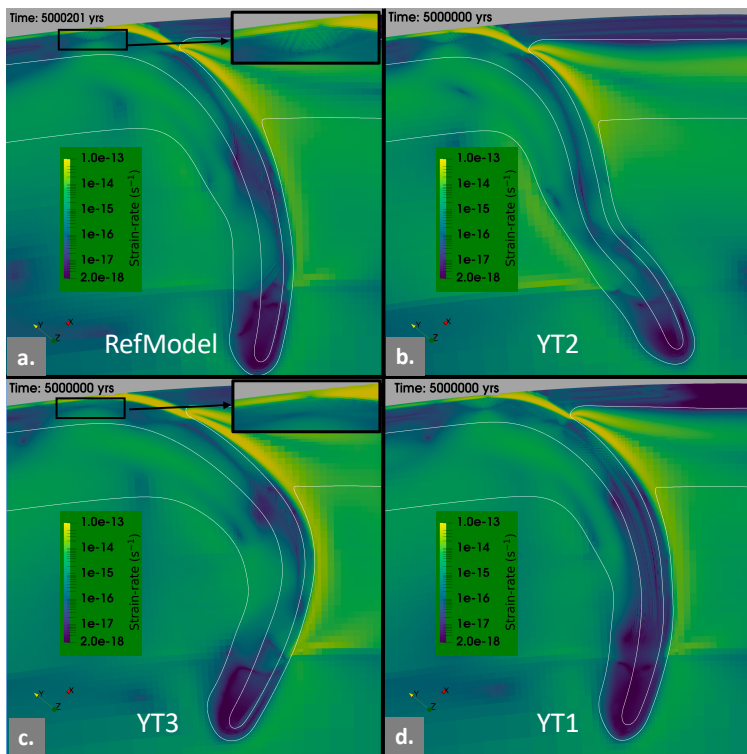
Figure 17: Phase 1 test results of varying yielding criterion implementation. In each panel the white labels indicate the name of the test model that each result corresponds to Table 6 and the color bar is scaled by strain-rate magnitude. The black rectangle in (c) is highlighting the absence of shear band development in YT3 in a region where shear bands develop in the black rectangle in (a), the Ref Model (and other models).

Two of the models were not able to be compared to the Ref Model as completely. The velocities of the sinking plate in Model YT4 reached about 50 cm/yr at the last graphical
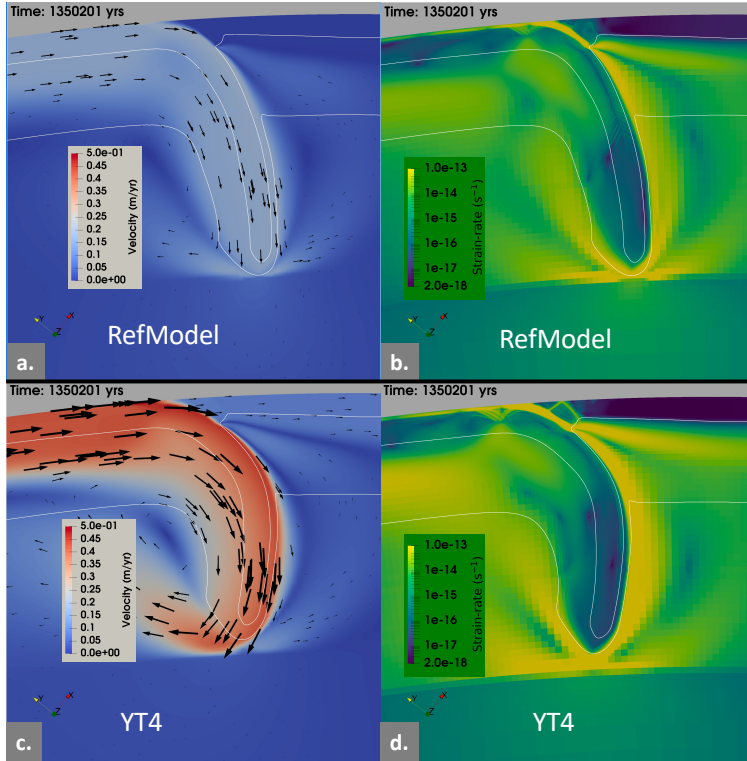
Figure 18: Comparison of Ref Model and Model YT4 showing unrealistic velocities developing in the test model. The Ref Model **(a)** and **(c)** YT4 solution for velocity magnitude (color scale) with flow field (black vectors scaled by the velocity). Note the much higher velocities in YT4 compared to the Ref Model. The Ref Model **(b)** and YT4 **(d)** solution for strain-rate magnitude (color scale). The time step shown here was the last graphical output of YT4 before the model failed.

output (Figure 18). This model reached very fast velocities (max velocity of 167e2 cm/yr) at ∼ 1.4e6 years causing the model to fail due to a lack of numerical convergence. Model YT5 does not have any results shown. This model resulted in even higher, extremely fast velocities (max velocity of 837 cm/yr) that led to numerical problems and model failure even earlier than Model YT4. A slab descending into the mantle has two ways of using its potential energy: internal deformation and pulling the upper plate at the surface along with it. Model YT4 included only DP in the shallowest 200 km of the slab, and no LTP. Without a yielding criterion, the sinking slab was very stiff and strong, and not able to deform internally as much. This led to more of the potential energy getting used for the slab pull force, which led to the very high plate velocities and eventual model failure. The slab was even stiffer and stronger in YT5 where no yielding was ever reached (DP and LTP off everywhere). This allowed less internal deformation and caused the velocities of the sinking slab to become non-physical within 5,000 years. The observed relationship in these models between slab rheology, slab stiffness, and subducting and sinking velocities is expected based on previous

work [*Billen and Arredondo*, 2018]. Additionally, visco-plastic models (e.g., *Čížková et al.* [2002], *Billen and Arredondo* [2018]) typically implement a maximum viscosity limit of 1e24 Pa·s, but we do not set a limit. A maximum viscosity limit tends to act like a yielding mechanism.
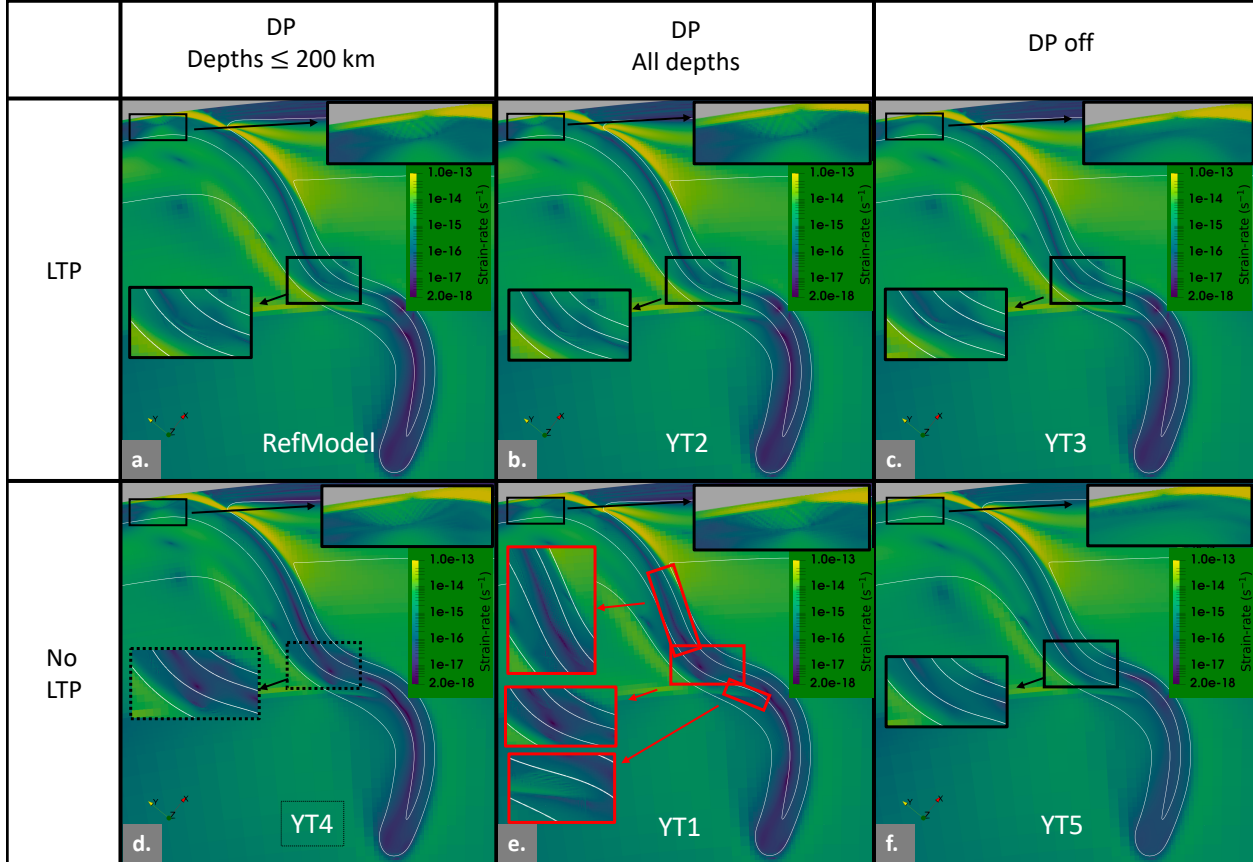
Figure 19: Phase 3 test results of varying yielding criterion. The table of results of the test models are arranged such that the models in the same row as each other have the same LTP implementation, and the models in the same columns as each other have the same DP implementation. The white labels indicate the name of the test model that each result corresponds to Table 6. The color bar is scaled by strain-rate. The solid rectangles are highlighting the two regions in the slab where the observance of shear bands was compared among tests. The black rectangles indicate regions where the yielding in the model was physically realistic: 1) DP on causing shallow shear bands or DP off leading to the absence of shallow shear bands 2) Deep shear bands only occurring when LTP is on. The red solid boxes indicate regions where there was yielding observed that was not physically realistic for the yielding mechanisms implemented in that model (e). The dotted black box in (d) is highlighting regions of yielding that occurring in YT4 where a stress of 1e12 Pa must have been reached. See text for details.

Phase 3   As these models are run with the static method, the focus here is not on how the yielding mechanisms affect the morphology of the slab, but just how it affects the short-term strain-rate magnitudes and spatial patterns. DP is expected to be the dominant (weakest) yielding mechanism at shallower depths, while LTP is expected to be dominant in the cold, interior of the slab. Figure 19 shows the effects on the strain-rate solutions when LTP is turned on and off. The top row of models (a-c) all include LTP and show generally higher strain-rates in the interior of the slab compared to the bottom row of models (d-f), none of which include LTP. Comparing two models where the only difference is turning LTP on or off, the maximum strain-rates decrease from $\sim$ 2.1e-14 s^{-1} in the Ref Model down to $\sim$ 7.9e-15 s^{-1} in YT4 within the mantle transition zone region of the slab. In both of these models, the deformation in the slab is dominated by the "elastic" viscosity, but the visco-plastic viscosity also contributes to how the slab internally deforms. In considering the distribution of deformation among mechanisms, the visco-plastic viscosity that includes dislocation, diffusion creep, and LTP (Ref Model) is expected to lead to higher strain-rates at the same stress when compared to a model that only has diffusion and dislocation creep contributing to the visco-plastic viscosity (YT4). These test model results agree with that strain-rate relationship.

The testing of turning DP on and off and imposing depth restrictions was to ensure that DP was not activated in the deep mantle where pressure-dependent brittle processes should not occur. The main observation in the models used to test this was whether shear bands developed or not at both shallow and deep depths. As shown in Figures 19a-c, this does have an effect on the pattern of strain-rates, particularly shear band development. Test Model YT2 which has DP on at all depths and LTP on shows shear band development at both shallow and deep depths (solid black rectangle). Models YT1 and YT3 test DP and LTP, respectively, individually to isolate the source of the shear bands seen in YT2. Based on the physical understanding of these mechanisms, only shallow shear bands are expected to develop in YT1 and only deep shear bands are expected to develop in YT3. Test Model

78

YT1 that has DP on at all depths with no LTP shows a different shear band development than YT2, but does show shear bands in the deeper slab (red boxes). The development of the deeper shear bands even when LTP is off is problematic because we do not expect the DP mechanism to be active at these depths. Model YT3 which has DP off at all depths and LTP on, shows shear band development only at deeper depths, and lacks shallow shear band development. These results indicate that DP is being activated in the deep slab beyond the depths where it should be. These observations support the decision to numerically restrict DP to depths shallower than 200 km and the interpretation that the deep shear bands observed in the reference model are a result of LTP, and not DP. Restricting the DP mechanism to shallow depths in the reference model and future models ensures numerically that these yielding mechanisms are occurring in the physically appropriate regions of the models.

Note Model YT4 did show very slight deep shear band development with LTP turned off and DP restricted to shallow depths (dotted black box in Figure 19d). This suggests that stress reached the Von Mises criterion of 1e12 Pa. This stress is not expected to be reached in the models that incorporate LTP, which would lead to a weaker slab and failure before that point.

6.2.2   Testing Viscosity Variations (Phase 2)

As described in the Phase 2 methods section above, we set the viscosity of the model to be constant everywhere by setting the minimum and maximum viscosities of the model to be equal at 5e15 Pa·s. We tested a few different values of viscosity to determine the effect of this value on 1) the residual stress field left after the relaxation stage and 2) the time it took to relax the majority of the stresses. The additional values tested were 1e16 Pa·s, 1e17 Pa·s, and 1e18 Pa·s. We could not test values lower than 5e15 Pa·s because at lower viscosities we ran into numerical issues. The viscosity value choice had negligible effects on the magnitude of the stress relaxation (Figure 20b-e), the pattern of stress relaxation in the lithosphere (Figure 20c-e), and the time to relax the stresses (Figure 20b). This validates
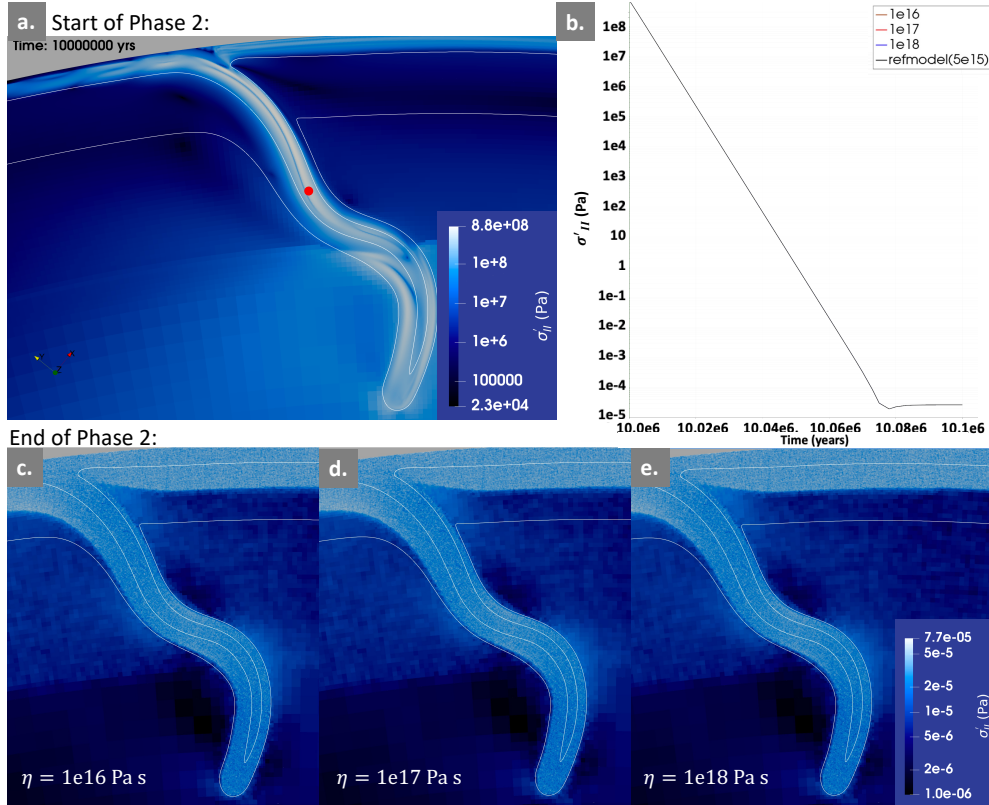
Figure 20: Phase 2 test results of varying the constant viscosity value implemented. **(a)** The solution field for the second invariant of the deviatoric stress at the end of Phase 1/Start of Phase 2. **(b)** The second invariant of the deviatoric stress plotted as a function of time for the location marked by the red point in **(a)** There are four lines plotted, one for the reference model (black), and then for each of the three tests of different viscosity tests. Note, the lines all plot on top of each other. **(c-e)** The end of Phase 2 for the three test models of using a constant velocity of 1e16 (c), 1e17 (d), and 1e18 (e) Pa·s. Note the colorscale shown in e applies to both c and d as well.

our usage of 5e15 Pa·s in the Proof of Concept Phase 2 model.

6.2.3 Testing the Elastic Time Step Implementation (Phase 3)

The implementation of elasticity in ASPECT uses an approximation to incorporate elasticity through an "elastic" viscosity and requires the choice of an elastic time-step, Δt_e. As a note, for the implementation in ASPECT, the numerical time step cannot be greater than Δt_e. The value of $\Delta t_e = 2,000$ years was chosen for the reference model. We ran multiple tests for Phase 3 of different Δt_e values to show the effect this parameter choice has on the static solution, in particular on the stress magnitude and spatial patterns. Models were run

with Δt_e values of 1e4, 1e5, and 1e6 years. The results found in this series of tests are shown in Figure 21. Overall as Δt_e value is increased, the magnitude of stress that is reached in the slab decreases and the spatial pattern of stress within the slab becomes less refined and more diffuse.

The initial choice of Δt_e =2,000 years is motivated by previous visco-elastic studies investigating Δt_e [*Farrington et al.*, 2014]. The results of the tests shown in this section can be explained by their work and by the static modeling visco-elastic-plastic deformation behavior described earlier (Section 5.3.1). For a simple visco-elastic loading and relaxation problem *Farrington et al.* [2014] showed that as the Δt_e value is decreased, the solution becomes closer to the analytical solution with higher peak stresses. They also showed that at longer Δt_e values, a model will capture the viscous deformation dynamics, but under resolve the stored stresses [*Farrington et al.*, 2014]. Therefore, an elastic time step should be chosen just long enough to capture the relevant timescales of the problem.

We are focused on the deep earthquake problem, but are not interested in modeling actual earthquakes or seismic timescales (i.e., 100-500 years). Therefore, decreasing Δt_e below 2,000 years is not necessary for this modeling. The Δt_e should be short enough to capture changes in elastic loading related to the time scale for changes in deformation of the slab. Since the slab sinks at 10-15 cm/yr, we need to capture the redistribution of stress between deformation mechanisms within this time frame. A priori it is not obvious whether 2,000 years is the best choice or if a longer time scale of 1e4 years would work just as well. The results of testing Δt_e = 2,000 years compared to 10,000 years shows that both implementations lead to similar results (Figure 21a,b). For an example point in the slab, both models reach comparable maximum stress levels within 100-150,000 years (Figure 21e).

Increasing Δt_e higher leads to clearer changes in the results. Longer Δt_e values of 100,000 years and 1 My clearly under predicts the initial build up of elastic stress (as predicted by *Farrington et al.* [2014]) (Figure 21c,d,e). This behavior in visco-elastic-plastic models can be understood by comparing the relative values of the "elastic viscosity" for each Δt_e with the
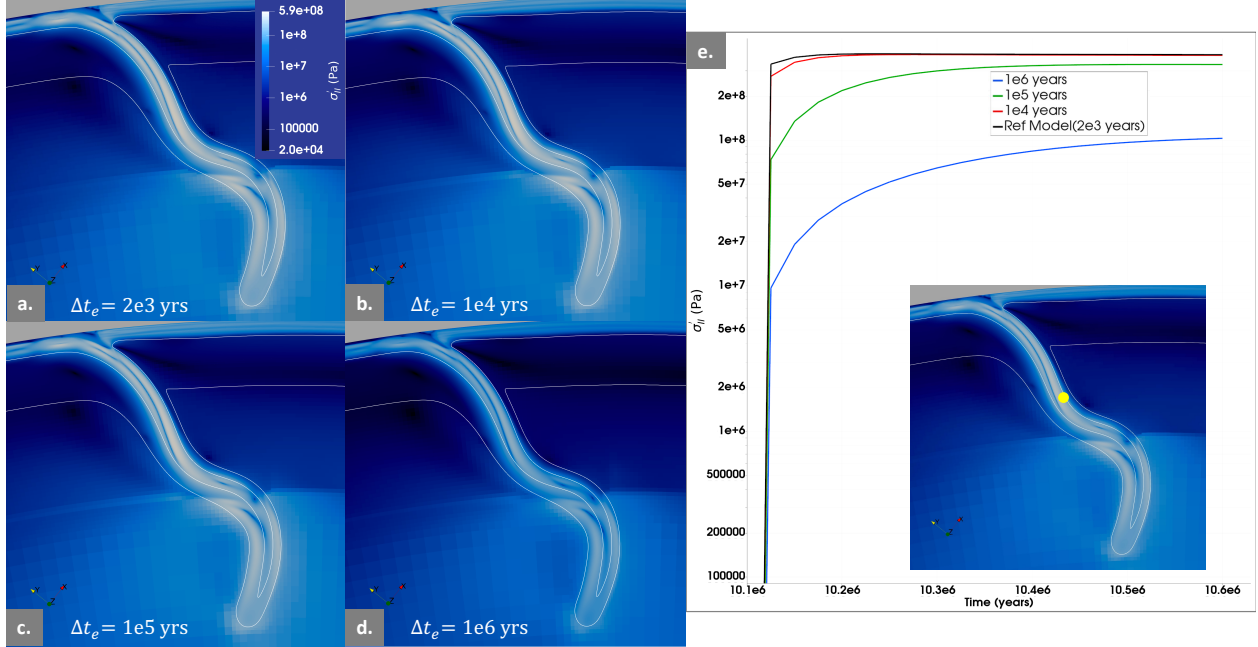
Figure 21: Phase 3 test results of varying the elastic time step parameter. **(a)** The second invariant of the deviatoric stress plotted for the reference model. Panels **(b)**, **(c)**, and **(d)** show the second invariant of the deviatoric stress plotted for test models identical to the reference model except for the choise of Δt_e changing to 1e4 years, 1e5 years, and 1e6 years, respectively. The colorbar in **(a)** corresponds to **(b)**,**(c)**, and **(d)**. **(e)** The second invariant of the deviatoric stress as a function of time for the red point in the inset slab. This is plotted for each of the four models shown in **(a)**, **(b)**, **(c)**, **(d)**.

visco-plastic viscosity expected for the cold slab interior (Table 7). The maximum viscosity in the model is set to 1e28 Pa·s to allow the "elastic viscosity" to naturally limit the numerical viscosity. Therefore, for $\Delta t_e = 2,000$ years, $\frac{\eta_{elastic}}{\eta_{VP}} < \frac{7.6e21Pa}{1e28pa} < 7.6e-7$ whereas for $\Delta t_e = $ 1e6 years, $\frac{\eta_{elastic}}{\eta_{VP}} < 3.8e-4$. The ratio of $\frac{\eta_{elastic}}{\eta_{VP}}$ increases by 3 orders of magnitude, moving closer to 1 ($\eta_{elastic} = \eta_{VP}$) when increasing Δt_e from 2,000 to 1 My. A smaller $\frac{\eta_{elastic}}{\eta_{VP}}$ ratio leads to a more dominant elastic component. In the $\Delta t_e = 2,000$ years case the "elastic" element deforms rapidly building up elastic strain and stress before any motion in the visco-plastic element can take place. In contrast, for the the $\Delta t_e = 1e6$ years case the elastic and visco-plastic elements respond on more similar timescales preventing the elastic strain and stress from building up before visco-plastic flow occurs. This explains the more diffuse stress pattern observed when Δt_e is longer and $\eta_{elastic}$ is higher. The initial elastic strain and stress build up is lower. The contrasts between the high and low stress regions remain lower and

more diffuse as the elastic and visco-plastic elements respond on these closer timescales. In the shorter Δt_e models the initial elastic stress build-up is what establishes the stress pattern early and the high-low stress boundaries sharpen as the visco-plastic elements distribute the deformation.

Elastic time step, years	"Elastic Viscosity", Pa
2,000	7.6e21
10,000	3.8e22
100,000	3.8e23
1,000,000	3.8e24

Table 7: **Increasing "Elastic Viscosity" as the elastic time step is increased.** Recall the elastic viscosity is the product of the elastic time step and rigidity.

7 Returning to Kermadec

7.1 Retesting the Strain-Rate Hypothesis

Now that we have demonstrated the validity of our static modeling methods, we can return to analyze the results of our location-specific model for Kermadec shown in Section 4. Recall that our main goal is to retest the strain-rate constraint hypothesis proposed in *Billen* [2020] that stated high strain-rate is an important general conditional requirement on the location of deep earthquakes. This was based on comparisons between numerical models and earthquake observations: depths of modeled high strain-rate correlate with higher deep earthquake activity and depths of modeled lower strain-rate correlate with lower deep earthquake activity. Here we show the same sort of comparison in Figure 22. There is general agreement between the Kermadec specific subduction model (*left*) and the Kermadec specific earthquake observations (*right*). The alignment of higher strain-rate regions in models with calculated seismic strain-rates from observations supports the proposed role of strain-rate in deep earthquake occurrence [*Billen*, 2020]. In the cold core of the slab (< 1173 K and below 100 km), maximum strain-rates reached $\sim$ 3e-15 s^{-1}. This is comparable (slightly faster) to the strain-rates calculated within this temperature contour in *Billen* [2020]. A direct comparison is challenging since the Kermadec slab in this work has a very different

morphology than the slabs presented in that study, but they found maximum strain-rates within this cold region to be generally between 1e-16 s^{-1} and 1e15 s^{-1} for their generic models. More models will be done in the future to strengthen this argument, but this first example demonstrates the utility of this modeling method and the workflow that will be used.
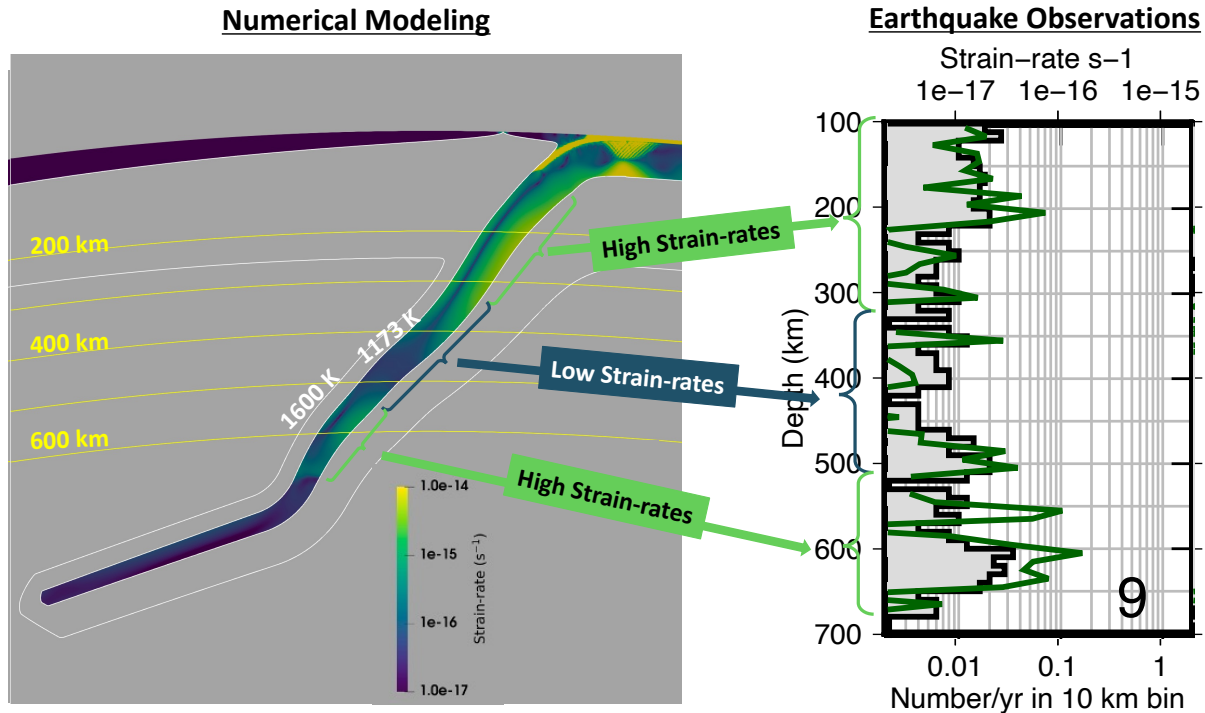
Figure 22: General agreement of spatial distribution of strain-rates between subduction model and earthquake observations. The left portion shows the strain-rate solution inside the cold-core of the slab where seismicity would occur. The yellow contours indicate depth. The right portion shows seismicity rate of events $M_W > 4$ *(gray histogram)* and strain-rate *(green line)* as a function of depth for a corresponding profile in Kermadec. (*Image modified from Magali Billen*). Earthquakes within $\pm$ 100 km of the profile are incorporated. Earthquakes are from the ISC-EHB catalog for events from 1964-2014.

7.2   Validating our results with observations

In addition, we now have stress magnitudes and orientations that can be compared with observations because these new models include the contributions from elastic deformation. We will focus on comparing the principal compression orientations which are represented by σ_1 in the models and by the P-axes in observations. Figure 23 shows the location-specific
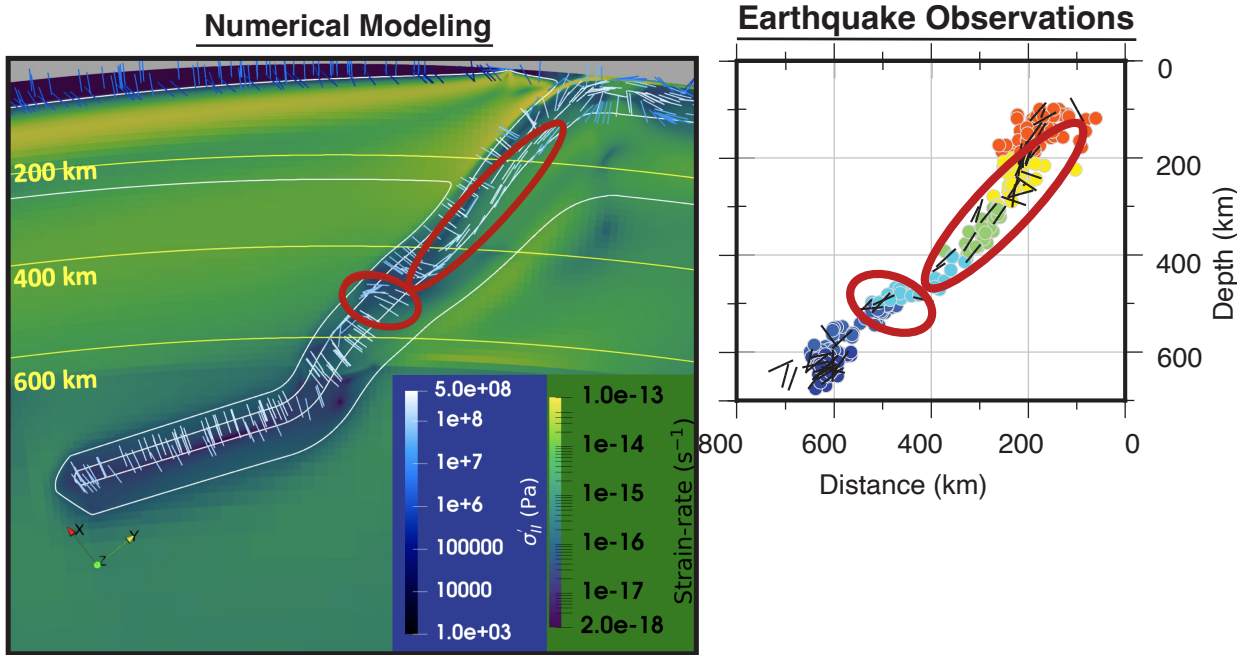
Figure 23: Comparison of principal tension orientations between subduction model and earthquake observations. The left side shows un-scaled computed σ_1 axes colored by the second invariant of the deviatoric stress overlain on top of the strain-rate solution. The σ_1 axes are only plotted for the portion of the slab within the 1173 K contour. The right side shows the cross section of observed earthquake distribution for this location. The colors indicate depth and the black lines are the P-axes (*Image modified from Magali Billen*). Earthquakes within $\pm$ 50 km of the profile are included. The red ovals highlight two particular sections of agreement where down-dip compressional or extensional regions align well between observations and the model. Ignore the grey ovals, they will be removed in final submitted version.

comparison of strain-rate, stress magnitude, and stress orientation, highlighting some specific regions of agreement between the numerically modeled σ_1 axes (*left*) and the P-axes from focal mechanism solutions of observed earthquakes (*right*).

The observed earthquakes exhibit down-dip compression throughout most of the slab from $\sim$ 100 - 500 km (long red oval). There are deviations from down-dip compression around 500 km to 600 km at depths where there are distinct changes in the morphology of the earthquake profile (smaller red oval). These general stress orientation patterns have been observed before in intermediate and deep earthquake FMS studies. The down-dip compression within the core of the slab has been observed for slabs with this general morphology that have begun to penetrate the lower mantle [*Isacks and Molnar*, 1971]. The changes in stress orientations

in areas of bending and buckling has been previously noted as well [*Myhill*, 2013]. In their analysis of multiple subduction zones, it was found that in bending or buckling regions, down-dip compression was observed within the inside of a bend and down-dip extension was observed on the outside of a bend.

The numerically modeled σ_1 axes plotted on top of the strain-rate magnitudes are also shown in Figure 23. These σ_1 axes show down-dip compression within the colder core of the slab from ~ 100 km down through 500 km (long red oval). This is followed by a switch to down-dip tension in the colder portion of the slab, with some down-dip compression on the topside (smaller red oval). Note the slab at this depth is transitioning from a concave up to a concave down bend.

The σ_1 axes from the numerical model show agreement with the observations of stress orientations in down going slabs [*Isacks and Molnar*, 1971; *Myhill*, 2013]. Specific to this profile in Kermadec, the red ovals highlight regions where the numerical model shows good agreement with the FMS observations for this specific location. The agreement of both location-specific and slab morphology specific P-axes orientations help validate the results of our models in that we are reproducing stress orientations during numerical simulations that are observed in the real subducting lithosphere. Figure 23 also shows that the decrease in earthquake activity and area with the lowest seismic activity between ~ 400-500 km in the observations aligns with the depth of lowest strain-rates between ~ 400-500 km in the numerical model. This is another observation that supports the strain-rate constraint hypothesis. Future work will analyze the principal stress orientations in more detail beyond this initial qualitative investigation. The same method of comparison will be carried out for all future profiles analyzed in the continued testing of the strain-rate constraint hypothesis.

As a note, it is not expected that every σ_1 axes in the model will agree with each observation. First, the observed earthquakes have location errors that could shift the locations of compression or extension slightly. Second, the numerical model can calculate the stress tensor throughout it's whole mesh, but the observed P-axes are only available where deep

earthquakes have already occurred. Therefore it is expected to have spatial gaps in our comparison. These may be filled in as more deep earthquakes occur and more observations become available.

8 Discussion

8.1 Utility of the Model in Investigation Deep Earthquakes

As mentioned above, *Billen* [2020] was focused on conditions that lead to deep earthquake failure, but did not further investigate specific mechanisms for how these earthquakes would occur. With the expectation that the future location investigations continue to validate the strain-rate constraint hypothesis, these updated modeling methods presented here will be used as a part of a larger workflow to investigate TSI specifically and its viability as a deep earthquake failure mechanism. This mechanism is advantageous to study in the deep slab because a physical failure model exists for this mechanism and does not for the other proposed mechanisms. Also TSI is the only mechanism that is likely to occur at all depths. TSI has been investigated previously, mostly for intermediate depth earthquake conditions and for specific events (e.g., *Kelemen and Hirth* [2007], *John et al.* [2009], *Thielmann et al.* [2015], *Thielmann* [2018]), but this future study will extend the depth and condition ranges explored. Appendix A describes how we will build on the work of *Thielmann* [2018] and goes into the details of the state of the TSI numerical model.

A brief overview of the workflow is that from the subduction modeling results, areas of high strain-rate, high stress, and low temperature can be identified as regions that could lead to deep earthquakes. The values of these conditions can then be used to set up the separate numerical model that simulates the initiation of TSI [*Thielmann et al.*, 2015; *Thielmann*, 2018]. The outputs of the subduction model become the inputs/initial conditions for the TSI model. This model then tests whether TSI will initiate or not under a particular set of conditions. In the TSI model we use the same rheology as in the subduction models. This approach is a way to zoom in spatially and focus on smaller time scale processes at a specific

location in the model. This extension of TSI investigation to deeper depths in the slab will help clarify where TSI may or may not be viable within subducting slabs.

A similar workflow of taking the subduction model outputs and using them as inputs in a different model could be used similarly to investigate DE, TTF, and strain-induced TF, if water contents and metastable olivine were taken into account in the models. In this way, conditions from our subduction models can be selected using the lens of the retested strain-rate constraint hypothesis to further the investigation of deep earthquake failure mechanisms.

8.2   Limitations of the Model

Although the methods in this study worked to address some of the limitations outlined in *Billen* [2020], there are still more limitations to consider when evaluating our new results. As described in Section 1.1.2, TTF relies on the presence of a MOW. For subduction modeling in general the presence of a MOW would be an important feature to consider. Its presence would change the density variation within the slab and therefore the forces in the slab driving and resisting slab pull, which could lead to changes in slab dynamics. The effect of metastable olivine [*Tetzlaff and Schmeling*, 2009] and metastable pyroxene [*Agrusta et al.*, 2014] have been incorporated in subduction models previously, but that is beyond the scope of this project. Additionally, there is not evidence of a MOW in all subduction zones, so it is still debated whether a MOW is a "global" feature within subducting slabs.

These models use a constant value of the elastic shear modulus (120 GPa) throughout the model domain. The Preliminary Reference Earth Model (PREM) calculated an increasing shear modulus with depth that ranged from ∼67-123 GPa from ∼120-670 km depth [*Dziewonski and Anderson*, 1981]. Future models could include a depth dependent shear modulus. Not only would changing the shear modulus affect the response of the elastic component of deformation individually, but this would also change the the "elastic viscosity" (equation 18-19). A change in the "elastic viscosity", as seen in Section 6.2.3, would affect how the deformation is partitioned among the visco-elastic-plastic deformation mechanisms.

At shallower depths where a lower shear modulus value relative to our Reference model would be used, the "elastic viscosity" would decrease. This would make the elastic component even weaker than in the current models and the initial elastic response more dominant. At deeper depths where a higher shear modulus would be used, the "elastic viscosity" would be slightly higher, but very close to the value implemented in the current models, and thus a similar partitioning between elastic and visco-plastic deformation mechanisms would be expected.

The rheology of the model could also be improved with respect to the viscosity and LTP flow laws that are used. The incorporation of newer flow laws for LTP [*Hansen et al.*, 2019] or for transition zone minerals [*Ritterbex et al.*, 2020] could effect the slab deformation behavior. Also a contributor to the rheological behavior, these models do not track any sort of fluids or dehydration reactions within the subducting slab. A constant water concentration is used throughout the model. Varying water content does affect the viscous behavior of rocks and causes it to become weaker. Incorporating dehydration behavior is important specifically for studying the viability of DE and TTF. DE depends on either the stress changes due to dehydration reactions or excess fluids leading to a high enough overpressure. Also important for TTF, if it is found that the deep slab stays hydrated, this would prevent the formation of a MOW. Although dehydration and fluid mobility has been incorporated in subduction models before (e.g., *Faccenda et al.* [2012]), this is not currently implemented in ASPECT. Another relevant parameter for the rheology and strength of the rocks would be incorporating a grain-size evolution model as these models only use a constant grain size. This is likely more important to incorporate because it would create a "memory effect" of past deformation that could lead to changes in rock strength (e.g., grain-size reduction, dynamic recrystallization).

These models are incompressible. As *Billen* [2020] points out in their models (also incompressible), this does not allow the model to track the deformation [*Nishi et al.*, 2013; *Zhan*, 2020] or pressure changes [*Houston*, 2015] related to phase transitions. The deformation and pressure changes could locally affect the phase transition depths and increase/decrease the down-dip compressional stresses in the slab that result from volume contraction when

transitioning from olivine to higher pressure phases [*Vallée*, 2013].

A final limitation to highlight is that these models are only 2D. Multiple 2D profiles will be done along a subduction zone in future work to look at along-strike variability, but this still does not incorporate the 3D structure of the slab into the simulations. Investigating how the force-balance that leads to the calculated slab stresses and strain-rates could change when the full 3D slab is being modeled and would be a future step to gain a more complete insight into deep earthquake behavior.

9 Conclusions

In this chapter we have presented two main results. The first, is an updated framework for investigating deep earthquake failure conditions in subducting slabs. Using our Proof of Concept model the static modeling method was demonstrated to be appropriate and accurate for modeling the stress and strain-rate in a visco-elastic-plastic slab model. The second, is the initial positive result of the retesting of the strain-rate constraint hypothesis of *Billen* [2020]. We verified that the strain-rate constraint hypothesis is consistent with the results of a location-specific model using a more appropriate visco-elastic-plastic rheology. The initial location-specific model for Kermadec demonstrated the workflow and applicability of our methods. This was just one profile example, but the future work will include more profiles for Kermadec, as well as developing similar location-specific models for profiles in other subduction zones. It will be important to apply our methods to slabs with varying morphologies, thermal parameters, and observed deep earthquake depth profiles (e.g., Chile, Japan, Tonga). These updated visco-elastic-plastic location-specific subduction models are a key step forward in investigating the conditions of strain-rate, stress, temperature, and pressure that promote or inhibit deep earthquake failure. As described in the Discussion section, these models will also be utilized in the larger framework of investigating deep earthquake failure mechanisms and trying to improve our understanding of how these earthquakes occur. Linking timescales within subducting slab evolution to investigate long-term slab deforma-

tion and how it relates to deep-focus earthquake occurrence is a crucial step towards better understanding these processes individually as well as the system as a whole.

Appendix A: Numerical Modeling of TSI

Modeling Thermal Shear Instability

A future direction of the deep earthquake investigation is the testing of individual deep earthquake failure mechanisms. This section describes how this will be done for the TSI mechanism. The initial conditions for setting up the TSI model (e.g., temperature, pressure, stress, strain-rate) will be determined through the subduction modeling and selected according to the strain-rate constraint hypothesis (i.e., high strain-rate, high stress, low temperature). Figures 24a-b shows a schematic of selecting conditions from an example region and using them to initiate the TSI model.

The numerical model to simulate grain size assisted thermal runaway and was developed by Marcel Thielmann [*Thielmann et al.*, 2015; *Thielmann*, 2018]. The model is currently set up for intermediate depth conditions so part of the proposed research is to modify this to deep slab conditions. The model relies on grain size reduction as a weakening mechanism that leads to TSI initiation. *Thielmann et al.* [2015] showed that incorporating grain size evolution can notably decrease the previously modeled critical stress required for thermal runaway [*Kelemen and Hirth*, 2007; *John et al.*, 2009]. In its current form (Figure 24b) a 1D incompressible model considers a block of dry olivine of thickness $L = 100$ km and infinite length. The initial temperature T_0, initial grain size $\mathscr{R}_0$, and initial stress are prescribed in the model setup. Located in the center of the block is a perturbed zone of thickness $h = 100$ m in which the material parameters are perturbed by both increasing the rheological prefactors, A_{pert} and by inhibiting grain growth. The 1D mesh has variable refinement, with increasing resolution moving from the edges to the perturbed zone. Within the perturbed zone is a fine, uniform mesh size of 1 cm. The block has a nonlinear visco-elastic Maxwell rheology.

The block deforms under simple shear assuming uniform stress though-out, which is implemented by setting a uniform background strain-rate everywhere in the block. **Note:**
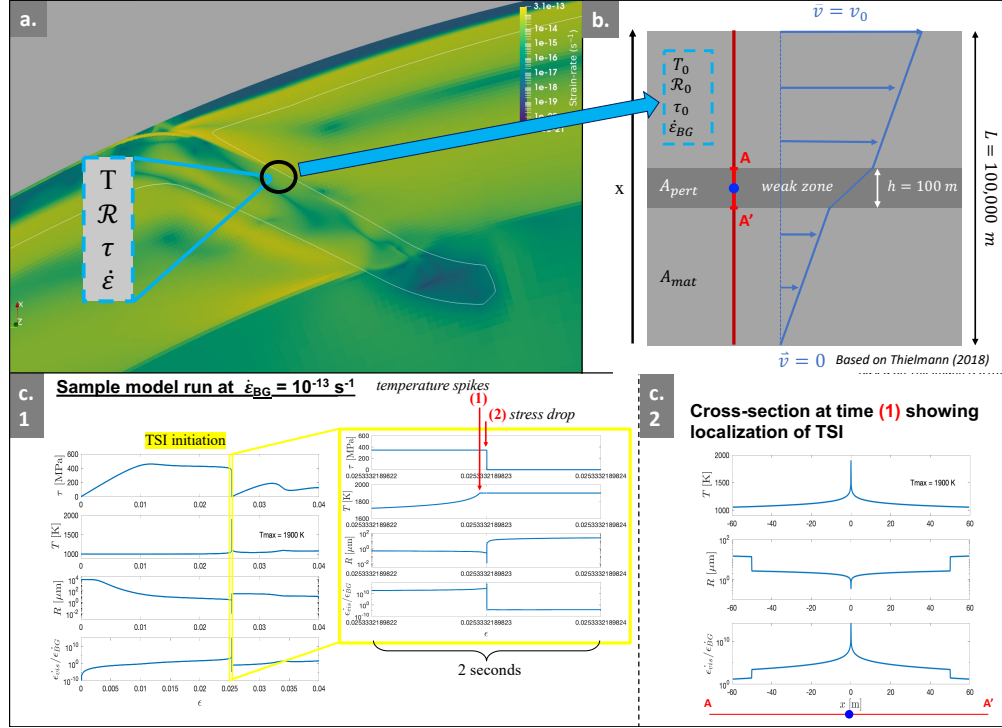
Figure 24: Workflow between subduction modeling and TSI modeling with a sample TSI model run result. (a) A synthetic example slab with a strain-rate solution shown by the colorscale. The temperature (T), grain-size ($\mathscr{R}$), stress (τ), and strain-rate ($\dot{\varepsilon}$) are associated with the region inside the black circle. This region would be chosen based on having high strain-rates, high stresses, and low temperatures. These conditions are then used as the initial conditions in the TSI model. **(b)** A schematic of the the TSI model domain with initial conditions, T_0, $\mathscr{R}_0$, τ_0, and $\dot{\varepsilon}_{BG}$ coming from the subduction model results. The model is a 1-D profile through a block of olivine with thickness L and infinite length with a perturbed zone of thickness h. Simple shear deformation of the block is a result of an applied velocity v_0 on the top boundary with a fixed zero velocity at the the bottom. The blue and red profiles illustrate, respectively, the velocity and flow law pre-factors (A_{mat}, A_{pert}) variations in the x-direction.**(c)** Example of a simulation I ran that produced a TSI using $\dot{\varepsilon}_{BG} = 13^{-1}$ s^{-1} and only dislocation and diffusion creep. **(c1)** Stress, grain size, temperature, and normalized strain-rate is plotted versus strain. The yellow rectangle is highlighting when TSI is initiated in this model run with the inset zooming in over a timescale of 2 seconds to emphasize the temperature, stress and grain size observations at the point of TSI initiation. **(c2)** Cross section A - B **(a)** extending just beyond the perturbed zone of grain size, temperature, and normalized strain-rate at the time-step where the maximum temperature is reached **(b)**. Note how localized the TSI process is.

This appendix describes the current rheology of the model as described in *Thielmann* [2018]. This rheology will be updated to match the visco-elastic-plastic rheology implemented in the subduction model described in the main text (e.g., removal of disGBS, update of LTP and viscous parameters/formulations). The current rheology of the model is set up such that the

total shear strain-rate $\dot{\varepsilon}_{xy}$ (notation simplified to $\dot{\varepsilon}$) is given by:

$$\dot{\varepsilon} = \frac{\partial v}{\partial x} = \frac{1}{\mu}\frac{\partial \tau}{\partial t} + \sum_{i=1}^{4} \dot{\varepsilon}_i \tag{25}$$

The indices of $i = 1 - 4$ of $\dot{\varepsilon}_i$ correspond to individual strain-rates of, in order, diffusion creep, dislocation creep, disGBS, and LTP, and μ is the shear modulus. For the dry olivine setup, the creep laws for diffusion and dislocation creep and disGBS [*Hirth and Kohlstedt*, 2003; *Kameyama et al.*, 1999] is:

$$\dot{\varepsilon}_i = A_i \exp\left(-\frac{E_i + PV_i}{RT}\right) \mathscr{R}^{-m_i}\tau^{n_i} \tag{26}$$

Here A_i is the preexponential constant, E_i is the activation energy, V_i is the activation volume, m_i is the grain size exponent, and n_i is the stress exponent. Temperature is T, pressure is P, grain size is $\mathscr{R}$, and R is the gas constant. The pressure term in (22) is not included in *Thielmann* [2018], but we add it here since we will be analyzing deeper conditions. We will be updating the model's current LTP flow law [*Goetze et al.*, 1978] to an updated LTP flow law [*Idrissi et al.*, 2016; *Kumamoto et al.*, 2017] to align with the LTP implementation in ASPECT:

$$\dot{\varepsilon}_{ltp} = A \exp\left(-\frac{Q}{RT}\left(1 - \left(\frac{\sigma}{\sigma_0}\right)^p\right)^q\right) \tag{27}$$

In this form A, σ_0, p, and q are empirical parameters and Q is the activation energy.

The model runs as the system of equations calculating the evolution of stress (28), grain size (29), and temperature (30) are solved as the block is deformed ($\dot{\varepsilon}_{BG}$). The equation for the evolution of stress is:

$$\frac{\partial \tau}{\partial t} = \mu\left[\dot{\varepsilon}_{BG} - \frac{1}{L}\int_{-\frac{L}{2}}^{\frac{L}{2}}\sum_{i=1}^{4}\dot{\varepsilon}_i\, dx\right] \tag{28}$$

Here $\dot{\varepsilon}_{BG} = v_0/L$ is the background strain-rate (an initial condition that will be prescribed according to the values of strain-rate found in the subduction modeling). This equation is derived by using the previously mentioned assumption of incompressibility and integrating

94

equation (25) with respect to x. The grain size evolution function is given by:

$$\frac{\partial \mathcal{R}}{\partial t} = \frac{\mathcal{G}}{p\,\mathcal{R}^{p-1}} - \frac{\lambda F_{\mathcal{R}}}{\gamma}\mathcal{R}^2\tau\sum_{i=2}^{4}\dot{\varepsilon}_i \qquad (29)$$

where $\mathcal{G} = k_0\exp(-Q_g/RT)$. This is a temperature-dependent growth factor where k_0 is a prefactor, Q_g is the activation energy, p is the growth exponent, λ is the partitioning coefficient, and γ is the surface tension. $F_{\mathcal{R}} = \frac{\lambda_3}{3\lambda_2}$ is a reduction factor where $\lambda_i = \exp(0.5i^2\sigma_{\mathcal{R}}^2)$ which varies based on $\sigma_{\mathcal{R}}$, the half-width of the lognormal grain size distribution. This equation is based on *Rozel et al.* [2011] and *Ricard and Bercovici* [2009] and assumes a single-phase rock with a few other assumptions. The first is that grain growth and grain size reduction depend only on surface energy decrease and increase. The second is that the distribution of grain sizes is lognormal and self-similar and therefore, changes to the grain size distribution can be represented in changing the mean grain size $\mathcal{R}$. It is also assumed that grain size reduction is only related to dislocation creep, LTP, and disGBS and that they all affect grain size reduction in the same way (equal fraction of deformational work that goes into grain size reduction regardless of creep type). Olivine grain growth parameters are used in the block, except in the perturbed zone where a forsterite-enstatite mixture is used. The final equation in the system of equations is the evolution of temperature:

$$\frac{\partial T}{\partial t} = \frac{k}{\rho c}\frac{\partial^2 T}{\partial x^2} + \frac{(1-\lambda)}{\rho c}\tau\sum_{i=2}^{4}\dot{\varepsilon}_i + \frac{\tau\dot{\varepsilon}_1}{\rho c} + \frac{\gamma\mathcal{G}}{\rho c p F_{\mathcal{R}}\mathcal{R}^{p+1}} \qquad (30)$$

Here, k is the diffusion coefficient, ρ is the density of the material, and c is the specific heat capacity. This equation accounts for thermal conductivity (term 1), visco-plastic strain-rate (terms 2 and 3), and grain size (term 4), which all affect temperature.

This system of equations (28, 29, 30) is solved over the whole mesh as the block is being deformed. An implicit ODE solver is used with an adaptive time-step based on the progression of the solution. This model is set up to explore the initiation of a TSI, not the full thermal runaway. The model is considered "stable" before runaway occurs, but crosses

into the "unstable" regime, once the localization process begins. This distinction between regimes is observed most clearly in the temperature growth rate or the gradient in stress. An example model run illustrating the grain-size reduction, spike in temperature, and drop in stress at the onset of TSI initiation is shown in Figure 24c.

Once the runaway initiates, the physics changes, and the model assumptions are no longer valid to simulate the evolution of the system. For example, the effects of the melting that would occur are not incorporated, so the extent of the evolution of the shear zone cannot be modeled. As it is 1D, the lateral propagation of the melting that would occur is not estimated either. Therefore the focus of this part of the workflow is not to examine the temporal or spatial extent of the thermal runaway process, but to focus on the onset of the process and when TSI can initiate given the specified background conditions of pressure, temperature, stress, strain-rate and rheology.

As noted above, the model is currently set up for intermediate depth conditions using creep parameters from *Hirth and Kohlstedt* [2003], *Hansen et al.* [2011], and *Goetze et al.* [1978] and neglecting pressure. We will modify it by adjusting the rheology to have depth appropriate creep parameters, remove disGBS, and updating the LTP equation above (23). The initial conditions for setting up the model (e.g., temperature, pressure, stress, strain-rate) will be determined through the subduction modeling and selected according to the strain-rate constraint hypothesis. Suites of TSI models with combinations of these properties will be run to see which of these conditions lead to a TSI initiation and which do not.

Appendix B: ASPECT Parameter File

Parameter file for the Phase 1 Reference Model begins on the following page.

```
set Dimension                                            = 2
set Use years in output instead of seconds   = true
set Start time                                               = 0
#set Resume computation                                              =true
set End time                                             =10e6
set Maximum first time step                              = 100
set Maximum relative increase in time step  = 30
set Maximum time step                                    = 1000
set Pressure normalization               = surface
set Surface pressure                    = 0
set Adiabatic surface temperature             = 1573
set Output directory                                     = /group/billengrp-mpi-
io/rfildes/Outputs/ThesisModels/vepprotoFS8060WC20DPon_output
set Nonlinear solver scheme                    = single Advection, iterated Stokes
#set Nonlinear solver scheme                   = no Advection, no Stokes #if using this
turn off elasticity
set Max nonlinear iterations               = 100
set Max nonlinear iterations in pre-refinement  = 0
set Nonlinear solver tolerance             = 1e-2
set World builder file                    = vep_proto8060WC.wb

subsection Formulation
  set Formulation = custom
  set Mass conservation = incompressible
  set Temperature equation = reference density profile
  set Enable elasticity = true
end

subsection Solver parameters
    set Composition solver tolerance = 1e-12
    set Temperature solver tolerance = 1e-12
    subsection Stokes solver parameters
        set Number of cheap Stokes solver steps = 200
        set Linear solver tolerance          = 1e-4
    end
end


# Chooses whether to use DG and limiter for composition
subsection Discretization
    set Composition polynomial degree = 2
    set Stokes velocity polynomial degree = 2
    set Temperature polynomial degree = 2
    set Use discontinuous composition discretization = false
    subsection Stabilization parameters
      set Use limiter for discontinuous composition solution = false
      set Global composition maximum = 75.0e9 ,75.0e9 ,75.0e9 ,1, 1, 1, 1, 1, 1
      set Global composition minimum = -75.0e9 ,-75.0e9 ,-75.0e9, 0, 0, 0, 0, 0 , 0
    end
end

subsection Geometry model
    set Model name = chunk
    subsection Chunk
        set Chunk inner radius = 3.481e6
        set Chunk outer radius = 6.371e6
        set Chunk minimum longitude = 0.0
        set Chunk maximum longitude = 80.0
        set Longitude repetitions =8
      set Radius repetitions = 3
    end
end

subsection Boundary velocity model
    set Tangential velocity boundary indicators =  bottom, top, west, east
end


subsection Heating model
```

```
    set List of model names = adiabatic heating, latent heat, shear heating
end

subsection Initial temperature model
    set List of model names = world builder
end

subsection Initial composition model
    set Model name = world builder
end

subsection Temperature field
      set Temperature method = field  # change this to field in non-static models/static in
static models
end

subsection Boundary temperature model
    set Fixed temperature boundary indicators = bottom, top #east and west are insultating since
they are not listed
    set List of model names = initial temperature
end

subsection Boundary composition model
    set Fixed composition boundary indicators =  #top, bottom, east and west are insulating since
they are not listed
end

subsection Compositional fields
   set Number of fields = 9
   set Names of fields = ve_stress_xx, ve_stress_yy, ve_stress_xy, \
       spcrust, spharz, opcrust, opharz, rdgcrust, rdgharz
   set Compositional field methods = field, field, field, \
       field, field, field, field, field, field        #change these all to field in non-static
model/static in static modelss
end

subsection Material model

    set Model name = visco plastic

    set Material averaging = harmonic average only viscosity

    subsection Visco Plastic

        set Include viscoelasticity = true
        set Include Peierls creep = true
        set Viscous flow law = composite
        set Viscosity averaging scheme = harmonic

        set Elastic shear moduli      = 1.2e11
        set Fixed elastic time step    = 2.0e3
        set Use fixed elastic time step = true

         set Reference temperature = 273
         set Reference strain rate = 1e-15

         set Minimum viscosity = 1e18
         set Maximum viscosity = 1e28

         set Phase transition depths = background:200e3|410e3|520e3|560e3| 670e3|670e3|670e3|
670e3|670e3, \
                 spcrust:80e3|200e3| 665e3|720e3, spharz:200e3|410e3|520e3|560e3|
670e3|670e3|670e3| 670e3|670e3

         set Phase transition widths = background:5e3|5e3|5e3|5e3| 5e3|5e3|5e3| 5e3|5e3, \
                 spcrust:5e3|5e3| 5e3|5e3, spharz:5e3|5e3|5e3|5e3| 5e3|5e3|5e3| 5e3|5e3

         set Phase transition temperatures = background:1662.0|1662.0|1662.0|1662.0|
1662.0|1662.0|1662.0| 1662.0|1662.0, \
```

```
                 spcrust:1173.0|1662.0|  1662.0|1662.0, spharz:1662.0|1662.0|1662.0|1662.0|
1662.0|1662.0|1662.0| 1662.0|1662.0

      set Phase transition temperature lower limits = background:-1e31|-1e31|-1e31|-1e31| -
1e31|-1e31|-1e31| 1662.0|1662.0, \
                 spcrust:-1e31|-1e31| -1e31|-1e31, spharz:-1e31|-1e31|-1e31|-1e31| -1e31|-1e31|-
1e31| 1662.0|1662.0

      set Phase transition temperature upper limits = background:1e31|1e31|1e31|1e31|
1662.0|1662.0|1662.0| 1e31|1e31, \
                 spcrust:1e31|1e31|  1e31|1e31, spharz:1e31|1e31|1e31|1e31| 1662.0|1662.0|1662.0|
1e31|1e31

      set Phase transition Clapeyron slopes = background:0.0|4e6|4.1e6|4e6| 4e6|-2e6|-3.1e6| -
2e6|1.3e6, \
                  spcrust:0.0|0.0|  4e6|1.3e6, spharz:0.0|4e6|4.1e6|4e6| 4e6|-2e6|-3.1e6| -
2e6|1.3e6

      set Thermal diffusivities = 1.0e-6
      set Heat capacities = 1250.0
      set Thermal expansivities = 3.1e-5

      set Yield mechanism = drucker
      set Angles of internal friction = background:25.0|0.0|0.0|0.0|0.0|0.0|0.0|0.0|0.0|0.0, \
             ve_stress_xx:0.0, ve_stress_yy:0.0, ve_stress_xy:0.0, \
             spcrust:25.0|25.0|0.0|0.0|0.0|, \
             spharz: 25.0|0.0|0.0|0.0|0.0|0.0|0.0|0.0|0.0|0.0, \
             opcrust:25, opharz:25, \
             rdgcrust:25, rdgharz:25

      set Cohesions = background:50.0e6|1e12|1e12|1e12|1e12|1e12|1e12|1e12|1e12|1e12, \
              ve_stress_xx:0.0, ve_stress_yy:0.0, ve_stress_xy:0.0, \
              spcrust:50.0e6|50.0e6|1e12|1e12|1e12|, \
              spharz: 50.0e6|1e12|1e12|1e12|1e12|1e12|1e12|1e12|1e12|1e12, \
             opcrust:50.0e6, opharz:50.0e6, \
             rdgcrust:50.0e6, rdgharz:50.0e6

    set Maximum yield stress = 1e12

      set Densities = background:3300.0|3300.0|3394.4|3442.1|3453.2| 3527.1|3691.45|3774.7|
3616.45|3772.0, \
             ve_stress_xx:0.0, ve_stress_yy:0.0, ve_stress_xy:0.0, \
             spcrust:3000.0|3540.0|3540.0| 3613.0|3871.7, \
             spharz:3235.0|3235.0|3372.3|3441.7|3441.7| 3478.7|3716.1|3759.4| 3679.1|3759.4, \
             opcrust:3000.0, opharz:3235.0, \
             rdgcrust:3000.0, rdgharz:3235.0

      set Grain size = 0.5000e-02

      set Prefactors for diffusion creep = \
             background:2.4536e-17|2.4536e-17|2.4536e-17|2.4536e-17|2.4536e-17|2.4536e-
17|6.3318e-20|6.3318e-20|6.3318e-20|6.3318e-20, \
             ve_stress_xx:1.0000e+00, ve_stress_yy:1.0000e+00, ve_stress_xy:1.0000e+00, \
             spcrust:5.0000e-21|2.4536e-17|2.4536e-17|6.3318e-20|6.3318e-20, \
             spharz:2.4536e-17|2.4536e-17|2.4536e-17|2.4536e-17|2.4536e-17|2.4536e-17|6.3318e-
20|6.3318e-20|6.3318e-20|6.3318e-20, \
             opcrust:2.4536e-17, opharz:2.4536e-17, \
             rdgcrust:5.0000e-21, rdgharz:5.0000e-21

      set Grain size exponents for diffusion creep = \

      background:3.0000e+00|3.0000e+00|3.0000e+00|3.0000e+00|3.0000e+00|3.0000e+00|3.0000e+00|3
.0000e+00|3.0000e+00|3.0000e+00, \
             ve_stress_xx:0.0, ve_stress_yy:0.0, ve_stress_xy:0.0, \
             spcrust:0.0000e+00|3.0000e+00|3.0000e+00|3.0000e+00|3.0000e+00, \

      spharz:3.0000e+00|3.0000e+00|3.0000e+00|3.0000e+00|3.0000e+00|3.0000e+00|3.0000e+00|3.000
0e+00|3.0000e+00|3.0000e+00, \
             opcrust:3.0000e+00, opharz:3.0000e+00, \
```

```
            rdgcrust:0.0000e+00, rdgharz:0.0000e+00

        set Activation energies for diffusion creep = \

        background:2.8500e+05|2.8500e+05|2.8500e+05|2.8500e+05|2.8500e+05|2.8500e+05|2.8500e+05|2
.8500e+05|2.8500e+05|2.8500e+05, \
                ve_stress_xx:0.0, ve_stress_yy:0.0, ve_stress_xy:0.0, \
                spcrust:0.0000e+00|2.8500e+05|2.8500e+05|2.8500e+05|2.8500e+05, \

        spharz:2.8500e+05|2.8500e+05|2.8500e+05|2.8500e+05|2.8500e+05|2.8500e+05|2.8500e+05|2.850
0e+05|2.8500e+05|2.8500e+05, \
                opcrust:2.8500e+05, opharz:2.8500e+05, \
                rdgcrust:0.0000e+00, rdgharz:0.0000e+00

        set Activation volumes for diffusion creep = \
                background:6.9000e-06|6.9000e-06|6.9000e-06|6.9000e-06|6.9000e-06|6.9000e-
06|3.0000e-06|3.0000e-06|3.0000e-06|3.0000e-06, \
                ve_stress_xx:0.0, ve_stress_yy:0.0, ve_stress_xy:0.0, \
                spcrust:0.0000e+00|6.9000e-06|6.9000e-06|3.0000e-06|3.0000e-06, \
                spharz:6.9000e-06|6.9000e-06|6.9000e-06|6.9000e-06|6.9000e-06|6.9000e-06|3.0000e-
06|3.0000e-06|3.0000e-06, \
                opcrust:6.9000e-06, opharz:6.9000e-06, \
                rdgcrust:0.0000e+00, rdgharz:0.0000e+00

        set Prefactors for dislocation creep = \
                background:3.5831e-17|3.5831e-17|3.5831e-17|3.5831e-17|3.5831e-17|3.5831e-
17|5.0000e-32|5.0000e-32|5.0000e-32|5.0000e-32, \
                ve_stress_xx:1.0e+00, ve_stress_yy:1.0e+00, ve_stress_xy:1.0e+00, \
                spcrust:5.0000e-32|3.5831e-17|3.5831e-17|5.0000e-32|5.0000e-32,\
                spharz:3.5831e-17|3.5831e-17|3.5831e-17|3.5831e-17|3.5831e-17|3.5831e-17|5.0000e-
32|5.0000e-32|5.0000e-32|5.0000e-32, \
                opcrust:3.5831e-17, opharz:3.5831e-17, \
                rdgcrust:5.0000e-32, rdgharz:5.0000e-32

        set Stress exponents for dislocation creep = \

        background:3.5000e+00|3.5000e+00|3.5000e+00|3.500e+00|3.5000e+00|3.5000e+00|1.0000e+00|1.
0000e+00|1.0000e+00|1.0000e+00, \
                ve_stress_xx:1.0e+00, ve_stress_yy:1.0e+00, ve_stress_xy:1.0e+00, \
                spcrust:1.0000e+00|3.5000e+00|3.5000e+00|1.0000e+00|1.0000e+00, \

        spharz:3.5000e+00|3.5000e+00|3.5000e+00|3.5000e+00|3.5000e+00|3.5000e+00|1.0000e+00|1.000
0e+00|1.0000e+00|1.0000e+00, \
                opcrust:3.5000e+00, opharz:3.5000e+00, \
                rdgcrust:1.0000e+00, rdgharz:1.0000e+00

        set Activation energies for dislocation creep = \

        background:5.0240e+05|5.0240e+05|5.0240e+05|5.0240e+05|5.0240e+05|5.0240e+05|0.0000e+00|0
.0000e+00|0.000e+00|0.000e+00, \
                ve_stress_xx:0.0, ve_stress_yy:0.0, ve_stress_xy:0.0, \
                spcrust:0.0000e+00|5.0240e+05|5.0240e+05|0.0000e+00|0.0000e+00, \

        spharz:5.0240e+05|5.0240e+05|5.0240e+05|5.0240e+05|5.0240e+05|5.0240e+05|0.0000e+00|0.000
0e+00|0.0000e+00|0.0000e+00, \
                opcrust:5.0240e+05, opharz:5.0240e+05, \
                rdgcrust:0.0000e+00, rdgharz:0.0000e+00

        set Activation volumes for dislocation creep = \
                background:1.2480e-05|1.2480e-05|1.2480e-05|1.2480e-05|1.2480e-05|1.2480e-
05|0.0000e+00|0.0000e+00|0.0000e+00|0.000e+00, \
                ve_stress_xx:0.0, ve_stress_yy:0.0, ve_stress_xy:0.0, \
                spcrust:0.0000e+00|1.2480e-05|1.2480e-05|0.0000e+00|0.0000e+00, \
                spharz:1.2480e-05|1.2480e-05|1.2480e-05|1.2480e-05|1.2480e-05|1.2480e-
05|0.0000e+00|0.0000e+00|0.0000e+00|0.0000e+00, \
                opcrust:1.2480e-05, opharz:1.2480e-05, \
                rdgcrust:0.0000e+00, rdgharz:0.0000e+00

        # Parameters for Idrissi Low Temperature Plasticity
```

```
        set Peierls creep flow law = viscosity approximation

        set Peierls fitting parameters = 0.17

        set Peierls glide parameters p = 0.5

        set Peierls glide parameters q = 1.0

        set Stress exponents for Peierls creep = 2.0

        set Peierls stresses = 5.9e9

        set Prefactors for Peierls creep = background:1.4e-19|1.4e-19|1.4e-19|1.4e-19|1.4e-
19|1.4e-19|1e-31|1e-31|1e-31|1e-31, \
              ve_stress_xx:0.0, ve_stress_yy:0.0, ve_stress_xy:0.0, \
              spcrust:1.4e-19|1.4e-19|1.4e-19|1e-31|1e-31, spharz:1.4e-19|1.4e-19|1.4e-19|1.4e-
19|1.4e-19|1.4e-19|1e-31|1e-31|1e-31|1e-31,\
              opcrust:1.4e-19, opharz:1.4e-19, \
              rdgcrust:0.0000e+00, rdgharz:0.0000e+00

        set Activation energies for Peierls creep =3.20e+05

        set Activation volumes for Peierls creep =0.0

    end
end

subsection Mesh refinement
  set Initial global refinement = 2
  set Minimum refinement level  = 2
  set Initial adaptive refinement = 7
  set Time steps between mesh refinement = 5 #static models = 0, change to 1 when running non-
static models

  set Strategy = minimum refinement function,  maximum refinement function, isosurfaces
  subsection Isosurfaces
    set Isosurfaces = \
              9, 9, Temperature: 0 | 1600;
  end

  subsection Minimum refinement function
    set Coordinate system = spherical
    set Variable names = r, phi
    set Function constants  = erad=6.371e6, cdpt=300e3, lm=1500e3, um=750e3, w1=18, w2=63
    set Function expression = ((erad-r <=um) ? 6 : (((erad-r <=lm) && (((pi/180) * w1) <= phi) &&
(phi<=(w2*(pi/180)))) ?  4 : 3))
  end

  subsection Maximum refinement function
    set Coordinate system   = spherical
    set Variable names      = r, phi
    set Function constants  = erad=6.371e6, cdpt=300e3, lm=1500e3, um=750e3, w1=18, w2=63
    set Function expression = ((erad-r <=um) ? 6 : (((erad-r <=lm) && (((pi/180) * w1) <= phi) &&
(phi<=(w2*(pi/180)))) ?  4 : 3))
  end

end
subsection Gravity model
    set Model name = radial constant
    subsection Radial constant
        set Magnitude = 9.81
    end
end

subsection Checkpointing
   set Steps between checkpoint           = 504
end

subsection Termination criteria
```

```
    set Checkpoint on termination = true
end

subsection Postprocess
  set List of postprocessors = visualization, velocity statistics, temperature statistics,
composition statistics, depth average
  subsection Depth average
    set Number of zones = 100
    set Output format = txt
    set Time between graphical output = 5e4 #years
  end
  subsection Visualization
    set List of output variables     = density, depth,  viscosity, strain rate, stress second
invariant, principal stress, spherical velocity components
    subsection Principal stress
      set Use deviatoric stress = true
    end
    set Output format               = vtu
    set Time between graphical output = 5e4  #yrs; use this setting for 1e6 or longer models
    #set Time steps between graphical output = 1  #use this setting for short tester models
    set Number of grouped files     = 0
  end
end
```

References

Agrusta, R., J. van Hunen, and S. Goes, The effect of metastable pyroxene on the slab dynamics, *Geophysical Research Letters*, *41*(24), 8800–8808, 2014.

Alpert, L., T. Becker, and I. Bailey, Global slab deformation and centroid moment tensor constraints on viscosity, *Geochemistry, Geophysics, Geosystems*, *11*(12), 2010.

Andersen, T. B., K. Mair, H. Austrheim, Y. Y. Podladchikov, and J. C. Vrijmoed, Stress release in exhumed intermediate and deep earthquakes determined from ultramafic pseudotachylyte, *Geology*, *36*(12), 995–998, doi:10.1130/G25230A.1, 2008.

Arredondo, K. M., and M. I. Billen, The effects of phase transitions and compositional layering in two-dimensional kinematic models of subduction, *Journal of Geodynamics*, *100*, 159–174, doi:10.1016/j.jog.2016.05.009, 2016.

Arredondo, K. M., and M. I. Billen, Coupled effects of phase transitions and rheology in 2-D dynamical models of subduction, *Journal of Geophysical Research: Solid Earth*, *122*(7), 5813–5830, doi:10.1002/2017JB014374, 2017.

Arrial, P.-A., and M. I. Billen, Influence of geometry and eclogitization on oceanic plateau subduction, *Earth and Planetary Science Letters*, *363*, 34–43, doi:10.1016/j.epsl.2012.12.011, 2013.

Bangerth, W., J. Dannberg, M. Fraters, R. Gassmoeller, A. Glerum, T. Heister, R. Myhill, and J. Naliboff, Aspect v2.5.0, doi:10.5281/zenodo.8200213, 2023a.

Bangerth, W., J. Dannberg, M. Fraters, R. Gassmoeller, A. Glerum, T. Heister, R. Myhill, and J. Naliboff, ASPECT: Advanced Solver for Problems in Earth's ConvecTion, User Manual, doi:10.6084/m9.figshare.4865333, doi:10.6084/m9.figshare.4865333, 2023b.

Bell, D. R., G. R. Rossman, J. Maldener, D. Endisch, and F. Rauch, Hydroxide in olivine:

A quantitative determination of the absolute amount and calibration of the ir spectrum, *Journal of Geophysical Research: Solid Earth*, *108*(B2), 2003.

Bessat, A., T. Duretz, G. Hetényi, S. Pilet, and S. M. Schmalholz, Stress and deformation mechanisms at a subduction zone: insights from 2-d thermomechanical numerical modelling, *Geophysical Journal International*, *221*(3), 1605–1625, 2020.

Billen, M. I., Deep slab seismicity limited by rate of deformation in the transition zone, *Science Advances*, *6*(22), eaaz7692, doi:10.1126/sciadv.aaz7692, 2020.

Billen, M. I., and K. M. Arredondo, Decoupling of plate-asthenosphere motion caused by non-linear viscosity during slab folding in the transition zone, *Physics of the Earth and Planetary Interiors*, *281*, 17–30, doi:10.1016/j.pepi.2018.04.011, 2018.

Bird, P., An updated digital model of plate boundaries, *Geochemistry, Geophysics, Geosystems*, *4*(3), 2003.

Burnley, P. C., H. W. Green, and D. J. Prior, Faulting associated with the olivine to spinel transformation in mg2geo4 and its implications for deep-focus earthquakes, *Journal of Geophysical Research: Solid Earth*, *96*(B1), 425–443, 1991.

Chen, P.-f., M. Nettles, E. A. Okal, and G. Ekström, Centroid moment tensor solutions for intermediate-depth earthquakes of the wwssn–hglp era (1962–1975), *Physics of the Earth and Planetary Interiors*, *124*(1-2), 1–7, 2001.

Christensen, U. R., and D. A. Yuen, Layered convection induced by phase transitions, *Journal of Geophysical Research: Solid Earth*, *90*(B12), 10,291–10,300, doi: 10.1029/JB090iB12p10291, 1985.

Čížková, H., J. van Hunen, A. P. van den Berg, and N. J. Vlaar, The influence of rheological weakening and yield stress on the interaction of slabs with the 670 km discontinuity, *Earth and Planetary Science Letters*, *199*(3-4), 447–457, 2002.

DeMets, C., R. G. Gordon, and D. F. Argus, Geologically current plate motions, *Geophysical journal international*, *181*(1), 1–80, 2010.

Dziewonski, A., T.-A. Chou, and J. H. Woodhouse, Determination of earthquake source parameters from waveform data for studies of global and regional seismicity, *Journal of Geophysical Research: Solid Earth*, *86*(B4), 2825–2852, 1981.

Dziewonski, A. M., and D. L. Anderson, Preliminary reference earth model, *Physics of the earth and planetary interiors*, *25*(4), 297–356, 1981.

Ekström, G., and M. Nettles, Calibration of the hglp seismograph network and centroid-moment tensor analysis of significant earthquakes of 1976, *Physics of the Earth and Planetary Interiors*, *101*(3-4), 219–243, 1997.

Ekström, G., M. Nettles, and A. Dziewoński, The global cmt project 2004–2010: Centroid-moment tensors for 13,017 earthquakes, *Physics of the Earth and Planetary Interiors*, *200*, 1–9, 2012.

Faccenda, M., T. V. Gerya, N. S. Mancktelow, and L. Moresi, Fluid flow during slab unbending and dehydration: Implications for intermediate-depth seismicity, slab weakening and deep water recycling, *Geochemistry, Geophysics, Geosystems*, *13*(1), 2012.

Farrington, R., L.-N. Moresi, and F. A. Capitanio, The role of viscoelasticity in subducting plates, *Geochemistry, Geophysics, Geosystems*, *15*(11), 4291–4304, 2014.

Fei, Y., et al., Experimentally determined postspinel transformation boundary in mg2sio4 using mgo as an internal pressure standard and its geophysical implications, *Journal of Geophysical Research: Solid Earth*, *109*(B2), 2004.

Ferrand, T. P., et al., Dehydration-driven stress transfer triggers intermediate-depth earthquakes, *Nature communications*, *8*(1), 15,247, 2017.

Fraters, M., The geodynamic world builder, doi:10.5281/zenodo.3900603, 2020.

Fraters, M., C. Thieulot, A. van den Berg, and W. Spakman, The geodynamic world builder: a solution for complex initial conditions in numerical modeling, *Solid Earth*, *10*(5), 1785–1807, 2019.

Frohlich, C., *Deep Earthquakes*, Cambridge University Press, 2006.

Fukao, Y., and M. Obayashi, Subducted slabs stagnant above, penetrating through, and trapped below the 660 km discontinuity, *Journal of Geophysical Research: Solid Earth*, *118*(11), 5920–5938, 2013.

Garel, F., S. Goes, D. Davies, J. H. Davies, S. C. Kramer, and C. R. Wilson, Interaction of subducted slabs with the mantle transition-zone: A regime diagram from 2-d thermo-mechanical models with a mobile trench and an overriding plate, *Geochemistry, Geophysics, Geosystems*, *15*(5), 1739–1765, 2014.

Gasc, J., N. Hilairet, T. Yu, T. Ferrand, A. Schubnel, and Y. Wang, Faulting of natural serpentinite: Implications for intermediate-depth seismicity, *Earth and Planetary Science Letters*, *474*, 138–147, 2017.

Gasc, J., C. Daigre, A. Moarefvand, D. Deldicque, J. Fauconnier, B. Gardonio, C. Madonna, P. Burnley, and A. Schubnel, Deep-focus earthquakes: From high-temperature experiments to cold slabs, *Geology*, *50*(9), 1018–1022, 2022.

Goetze, C., J. P. Poirier, A. Kelly, A. H. Cook, and G. W. Greenwood, The mechanisms of creep in olivine, *Philosophical Transactions of the Royal Society of London. Series A, Mathematical and Physical Sciences*, *288*(1350), 99–119, doi:10.1098/rsta.1978.0008, 1978.

Gorbatov, A., and V. Kostoglodov, Maximum depth of seismicity and thermal parameter of the subducting slab: general empirical relation and its application, *Tectonophysics*, *277*(1-3), 165–187, 1997.

Green, H., and P. Burnley, A new self-organizing mechanism for deep-focus earthquakes, *Nature*, *341*(6244), 733–737, 1989.

Green, H. W., and H. Houston, The mechanics of deep earthquakes, *Annual Review of Earth and Planetary Sciences*, *23*(1), 169–213, 1995.

Green, H. W., and Y. Zhou, Transformation-induced faulting requires an exothermic reaction and explains the cessation of earthquakes at the base of the mantle transition zone, *Tectonophysics*, *256*(1-4), 39–56, 1996.

Griggs, D., and J. Handin, Observations on fracture and a hypothesis of earthquakes, *Geological Society of America Memoirs*, *79*, 347–364, 1960.

Griggs, D., D. Baker, and H. Mark, Properties of matter under unusual conditions, 1969.

Gutenberg, B., and C. Richter, *Seismicity of the Earth*, vol. 34, Geological Society of America, 1941.

Hacker, B. R., and G. Bebout, Eclogite formation and the rheology, buoyancy, seismicity, and h~ 2o content of oceanic crust, *Geophysical Monograph-American Geophysical Union*, *96*, 337–346, 1996.

Hacker, B. R., G. A. Abers, and S. M. Peacock, Subduction factory 1. theoretical mineralogy, densities, seismic wave speeds, and h2o contents, *Journal of Geophysical Research: Solid Earth*, *108*(B1), 2003.

Hansen, L. N., M. E. Zimmerman, and D. L. Kohlstedt, Grain boundary sliding in San Carlos olivine: Flow law parameters and crystallographic-preferred orientation, *Journal of Geophysical Research: Solid Earth*, *116*(B8), doi:10.1029/2011JB008220, 2011.

Hansen, L. N., K. M. Kumamoto, C. A. Thom, D. Wallis, W. B. Durham, D. L. Goldsby, T. Breithaupt, C. D. Meyers, and D. L. Kohlstedt, Low-temperature plasticity in olivine:

Grain size, strain hardening, and the strength of the lithosphere, *Journal of Geophysical Research: Solid Earth*, *124* (6), 5427–5449, 2019.

Hayes, G. P., G. L. Moore, D. E. Portner, M. Hearne, H. Flamme, M. Furtney, and G. M. Smoczyk, Slab2, a comprehensive subduction zone geometry model, *Science*, *362* (6410), 58–61, doi:10.1126/science.aat4723, 2018.

He, Y., E. G. Puckett, and M. I. Billen, A discontinuous Galerkin method with a bound preserving limiter for the advection of non-diffusive fields in solid earth geodynamics, *Physics of the Earth and Planetary Interiors*, *263*, 23 – 37, doi:10.1016/j.pepi.2016.12.001, 2017.

Heister, T., J. Dannberg, R. Gassmöller, and W. Bangerth, High accuracy mantle convection simulation through modern numerical methods. II: Realistic models and problems, *Geophysical Journal International*, *210* (2), 833–851, doi:10.1093/gji/ggx195, 2017.

Hirose, K., Phase transitions in pyrolitic mantle around 670-km depth: Implications for upwelling of plumes from the lower mantle, *Journal of Geophysical Research: Solid Earth*, *107* (B4), ECV–3, 2002.

Hirth, G., and D. Kohlstedt, Rheology of the upper mantle and the mantle wedge: A view from the experimentalists, *Geophysical Monograph-American Geophysical Union*, *138*, 83–106, 2003.

Hobbs, B. E., and A. Ord, Plastic instabilities: Implications for the origin of intermediate and deep focus earthquakes, *Journal of Geophysical Research: Solid Earth*, *93* (B9), 10,521–10,540, 1988.

Houston, H., Deep Earthquakes, in *Treatise on Geophysics (Second Edition)*, edited by G. Schubert, pp. 329–354, Elsevier, Oxford, doi:10.1016/B978-0-444-53802-4.00079-8, 2015.

Huang, W.-C., and E. A. Okal, Centroid-moment-tensor solutions for deep earthquakes predating the digital era: Discussion and inferences, *Physics of the Earth and Planetary interiors*, *106*(3-4), 191–218, 1998.

Idrissi, H., C. Bollinger, F. Boioli, D. Schryvers, and P. Cordier, Low-temperature plasticity of olivine revisited with in situ tem nanomechanical testing, *Science advances*, *2*(3), e1501,671, 2016.

Incel, S., et al., Laboratory earthquakes triggered during eclogitization of lawsonite-bearing blueschist, *Earth and Planetary Science Letters*, *459*, 320–331, 2017.

Inoue, T., et al., The phase boundary between wadsleyite and ringwoodite in mg 2 sio 4 determined by in situ x-ray diffraction, *Physics and Chemistry of Minerals*, *33*, 106–114, 2006.

Isacks, B., and P. Molnar, Distribution of stresses in the descending lithosphere from a global survey of focal-mechanism solutions of mantle earthquakes, *Reviews of Geophysics*, *9*(1), 103–174, 1971.

Ita, J., and S. D. King, Sensitivity of convection with an endothermic phase change to the form of governing equations, initial conditions, boundary conditions, and equation of state, *Journal of Geophysical Research: Solid Earth*, *99*(B8), 15,919–15,938, doi: 10.1029/94JB00852, 1994.

Ji, S., and P. Zhao, Layered rheological structure of subducting oceanic lithosphere, *Earth and planetary science letters*, *124*(1-4), 75–94, 1994.

John, T., S. Medvedev, L. H. Rüpke, T. B. Andersen, Y. Y. Podladchikov, and H. Austrheim, Generation of intermediate-depth earthquakes by self-localizing thermal runaway, *Nature Geoscience*, *2*(2), 137–140, doi:10.1038/ngeo419, 2009.

Kameyama, M., D. A. Yuen, and S.-I. Karato, Thermal-mechanical effects of low-temperature plasticity (the Peierls mechanism) on the deformation of a viscoelastic shear zone, *Earth and Planetary Science Letters*, *168*(1), 159–172, doi:10.1016/S0012-821X(99)00040-0, 1999.

Kanamori, H., D. L. Anderson, and T. H. Heaton, Frictional Melting During the Rupture of the 1994 Bolivian Earthquake, *Science*, *279*(5352), 839–842, doi: 10.1126/science.279.5352.839, 1998.

Karato, S.-I., and H. Jung, Effects of pressure on high-temperature dislocation creep in olivine, *Philosophical Magazine*, *83*(3), 401–414, 2003.

Karato, S.-i., M. R. Riedel, and D. A. Yuen, Rheological structure and deformation of subducted slabs in the mantle transition zone: implications for mantle circulation and deep earthquakes, *Physics of the Earth and Planetary Interiors*, *127*(1), 83–108, doi: 10.1016/S0031-9201(01)00223-0, 2001.

Katsura, T., et al., Olivine-wadsleyite transition in the system (mg, fe) 2sio4, *Journal of Geophysical Research: Solid Earth*, *109*(B2), 2004.

Kelemen, P. B., and G. Hirth, A periodic shear-heating mechanism for intermediate-depth earthquakes in the mantle, *Nature*, *446*(7137), 787–790, doi:10.1038/nature05717, 2007.

Keppler, H., and N. Bolfan-Casanova, Thermodynamics of water solubility and partitioning, *Reviews in Mineralogy and Geochemistry*, *62*(1), 193–230, 2006.

Kirby, S. H., S. Stein, E. A. Okal, and D. C. Rubie, Metastable mantle phase transformations and deep earthquakes in subducting oceanic lithosphere, *Reviews of geophysics*, *34*(2), 261–306, 1996.

Kohlstedt, D., H. Keppler, and D. Rubie, Solubility of water in the α, β and γ phases of (mg, fe) 2 sio 4, *Contributions to Mineralogy and Petrology*, *123*, 345–357, 1996.

Koper, K. D., D. A. Wiens, L. M. Dorman, J. A. Hildebrand, and S. C. Webb, Modeling the tonga slab: Can travel time data resolve a metastable olivine wedge?, *Journal of Geophysical Research: Solid Earth*, *103*(B12), 30,079–30,100, 1998.

Kronbichler, M., T. Heister, and W. Bangerth, High accuracy mantle convection simulation through modern numerical methods, *Geophysical Journal International*, *191*, 12–29, doi: 10.1111/j.1365-246X.2012.05609.x, 2012.

Kumamoto, K. M., C. A. Thom, D. Wallis, L. N. Hansen, D. E. Armstrong, J. M. Warren, D. L. Goldsby, and A. J. Wilkinson, Size effects resolve discrepancies in 40 years of work on low-temperature plasticity in olivine, *Science advances*, *3*(9), e1701,338, 2017.

Levitas, V. I., Resolving puzzles of the phase-transformation-based mechanism of the strong deep-focus earthquake, *Nature Communications*, *13*(1), 6291, 2022.

Litasov, K. D., and E. Ohtani, Phase relations in hydrous morb at 18–28 gpa: implications for heterogeneity of the lower mantle, *Physics of the Earth and Planetary Interiors*, *150*(4), 239–263, 2005.

Meade, C., and R. Jeanloz, Deep-focus earthquakes and recycling of water into the earth's mantle, *Science*, *252*(5002), 68–72, 1991.

Mei, S., A. Suzuki, D. Kohlstedt, N. Dixon, and W. Durham, Experimental constraints on the strength of the lithospheric mantle, *Journal of Geophysical Research: Solid Earth*, *115*(B8), 2010.

Moresi, L., F. Dufour, and H. B. Mühlhaus, A Lagrangian integration point finite element method for large deformation modeling of viscoelastic geomaterials, *Journal of Computational Physics*, *184*(2), 476–497, doi:10.1016/S0021-9991(02)00031-1, 2003.

Morra, G., K. Regenauer-Lieb, and D. Giardini, Curvature of oceanic arcs, *Geology*, *34*(10), 877–880, 2006.

Mosenfelder, J. L., F. C. Marton, C. R. Ross II, L. Kerschhofer, and D. C. Rubie, Experimental constraints on the depth of olivine metastability in subducting lithosphere, *Physics of the Earth and Planetary Interiors*, *127*(1-4), 165–180, 2001.

Myhill, R., Slab buckling and its effect on the distributions and focal mechanisms of deep-focus earthquakes, *Geophysical Journal International*, *192*(2), 837–853, 2013.

Nishi, M., T. Kubo, H. Ohfuji, T. Kato, Y. Nishihara, and T. Irifune, Slow si–al interdiffusion in garnet and stagnation of subducting slabs, *Earth and Planetary Science Letters*, *361*, 44–49, 2013.

Obayashi, M., Y. Fukao, and J. Yoshimitsu, Unusually deep bonin earthquake of 30 may 2015: A precursory signal to slab penetration?, *Earth and Planetary Science Letters*, *459*, 221–226, 2017.

Ogawa, M., Shear instability in a viscoelastic material as the cause of deep focus earthquakes, *Journal of Geophysical Research: Solid Earth*, *92*(B13), 13,801–13,810, doi: 10.1029/JB092iB13p13801, 1987.

Ohuchi, T., Y. Nishihara, T. Kawazoe, D. Spengler, R. Shiraishi, A. Suzuki, T. Kikegawa, and E. Ohtani, Superplasticity in hydrous melt-bearing dunite: Implications for shear localization in earth's upper mantle, *Earth and Planetary Science Letters*, *335*, 59–71, 2012.

Ohuchi, T., T. Kawazoe, Y. Higo, K.-i. Funakoshi, A. Suzuki, T. Kikegawa, and T. Irifune, Dislocation-accommodated grain boundary sliding as the major deformation mechanism of olivine in the earth's upper mantle, *Science advances*, *1*(9), e1500,360, 2015.

Ohuchi, T., X. Lei, H. Ohfuji, Y. Higo, Y. Tange, T. Sakai, K. Fujino, and T. Irifune, Intermediate-depth earthquakes linked to localized heating in dunite and harzburgite, *Nature Geoscience*, *10*(10), 771–776, 2017.

Parson, L., and I. Wright, The lau-havre-taupo back-arc basin: A southward-propagating, multi-stage evolution from rifting to spreading, *Tectonophysics*, *263*(1-4), 1–22, 1996.

Poli, P., G. Prieto, E. Rivera, and S. Ruiz, Earthquakes initiation and thermal shear instability in the Hindu Kush intermediate depth nest, *Geophysical Research Letters*, *43*(4), 1537–1542, doi:10.1002/2015GL067529, 2016.

Raleigh, C. B., and M. Paterson, Experimental deformation of serpentinite and its tectonic implications, *Journal of Geophysical Research*, *70*(16), 3965–3985, 1965.

Ricard, Y., and D. Bercovici, A continuum theory of grain size evolution and damage, *Journal of Geophysical Research: Solid Earth*, *114*(B1), doi:10.1029/2007JB005491, 2009.

Ringwood, A. E., Phase transformations and their bearing on the constitution and dynamics of the mantle, *Geochimica et Cosmochimica Acta*, *55*(8), 2083–2110, 1991.

Ritterbex, S., P. Carrez, and P. Cordier, Deformation across the mantle transition zone: A theoretical mineral physics view, *Earth and Planetary Science Letters*, *547*, 116,438, 2020.

Royden, L. H., and L. Husson, Trench motion, slab geometry and viscous stresses in subduction systems, *Geophysical Journal International*, *167*(2), 881–905, 2006.

Rozel, A., Y. Ricard, and D. Bercovici, A thermodynamically self-consistent damage equation for grain size evolution during dynamic recrystallization, *Geophysical Journal International*, *184*(2), 719–728, doi:10.1111/j.1365-246X.2010.04875.x, 2011.

Rubie, D. C., and C. R. Ross, Kinetics of the olivine-spinel transformation in subducting lithosphere: Experimental constraints and implications for deep slab processes, *Physics of the Earth and Planetary Interiors*, *86*(1-3), 223–243, 1994.

Saikia, A., D. J. Frost, and D. C. Rubie, Splitting of the 520-kilometer seismic discontinuity and chemical heterogeneity in the mantle, *Science*, *319*(5869), 1515–1518, 2008.

Scholz, C. H., *The mechanics of earthquakes and faulting*, Cambridge university press, 2019.

Seton, M., R. D. Müller, S. Zahirovic, S. Williams, N. M. Wright, J. Cannon, J. M. Whittaker, K. J. Matthews, and R. McGirr, A global data set of present-day oceanic crustal age and seafloor spreading parameters, *Geochemistry, Geophysics, Geosystems*, *21*(10), e2020GC009,214, 2020.

Shen, Z., and Z. Zhan, Metastable Olivine Wedge Beneath the Japan Sea Imaged by Seismic Interferometry, *Geophysical Research Letters*, *47*(6), e2019GL085,665, doi: 10.1029/2019GL085665, 2020.

Shirey, S. B., L. S. Wagner, M. J. Walter, D. G. Pearson, and P. E. van Keken, Slab transport of fluids to deep focus earthquake depths—thermal modeling constraints and evidence from diamonds, *AGU advances*, *2*(2), e2020AV000,304, 2021.

Sinogeikin, S. V., J. D. Bass, and T. Katsura, Single-crystal elasticity of ringwoodite to high pressures and high temperatures: implications for 520 km seismic discontinuity, *Physics of the Earth and Planetary Interiors*, *136*(1-2), 41–66, 2003.

Tetzlaff, M., and H. Schmeling, Time-dependent interaction between subduction dynamics and phase transition kinetics, *Geophysical Journal International*, *178*(2), 826–844, 2009.

Thielmann, M., Grain size assisted thermal runaway as a nucleation mechanism for continental mantle earthquakes: Impact of complex rheologies, *Tectonophysics*, *746*, 611–623, doi:10.1016/j.tecto.2017.08.038, 2018.

Thielmann, M., A. Rozel, B. J. P. Kaus, and Y. Ricard, Intermediate-depth earthquake generation and shear zone formation caused by grain size reduction and shear heating, *Geology*, *43*(9), 791–794, doi:10.1130/G36864.1, 2015.

Turcotte, D. L., D. McAdoo, and J. Caldwell, An elastic-perfectly plastic analysis of the bending of the lithosphere at a trench, *Tectonophysics*, *47*(3-4), 193–205, 1978.

Uieda, L., et al., PyGMT: A Python interface for the Generic Mapping Tools, doi: 10.5281/zenodo.7772533, 2023.

Utsu, T., A statistical study on the occurrence of aftershocks, *Geophys. Mag.*, *30*, 521–605, 1961.

Vallée, M., Source time function properties indicate a strain drop independent of earthquake depth and magnitude, *Nature communications*, *4*(1), 2606, 2013.

Van Dinther, Y., T. Gerya, L. Dalguer, P. M. Mai, G. Morra, and D. Giardini, The seismic cycle at subduction thrusts: Insights from seismo-thermo-mechanical models, *Journal of Geophysical Research: Solid Earth*, *118*(12), 6183–6202, 2013.

Van Zelst, I., S. Wollherr, A.-A. Gabriel, E. H. Madden, and Y. van Dinther, Modeling megathrust earthquakes across scales: One-way coupling from geodynamics and seismic cycles to dynamic rupture, *Journal of Geophysical Research: Solid Earth*, *124*(11), 11,414–11,446, 2019.

Wang, Y., T. Uchida, J. Zhang, M. L. Rivers, and S. R. Sutton, Thermal equation of state of akimotoite mgsio3 and effects of the akimotoite–garnet transformation on seismic structure near the 660 km discontinuity, *Physics of the Earth and Planetary Interiors*, *143*, 57–80, 2004.

Weidner, D. J., and Y. Wang, Chemical-and clapeyron-induced buoyancy at the 660 km discontinuity, *Journal of Geophysical Research: Solid Earth*, *103*(B4), 7431–7441, 1998.

Wiens, D. A., and H. J. Gilbert, Effect of slab temperature on deep-earthquake aftershock productivity and magnitude–frequency relations, *Nature*, *384*(6605), 153–156, 1996.

Yamasaki, T., and T. Seno, Double seismic zone and dehydration embrittlement of the subducting slab, *Journal of Geophysical Research: Solid Earth*, *108*(B4), 2003.

Yonggang, G. Y., Z. Wu, and R. M. Wentzcovitch, α–β–γ transformations in mg2sio4 in earth's transition zone, *Earth and Planetary Science Letters*, *273*(1-2), 115–122, 2008.

Yu, Y. G., R. M. Wentzcovitch, V. L. Vinograd, and R. J. Angel, Thermodynamic properties of mgsio3 majorite and phase transitions near 660 km depth in mgsio3 and mg2sio4: A first principles study, *Journal of Geophysical Research: Solid Earth*, *116*(B2), 2011.

Zhan, Z., Gutenberg–Richter law for deep earthquakes revisited: A dual-mechanism hypothesis, *Earth and Planetary Science Letters*, *461*, 1–7, doi:10.1016/j.epsl.2016.12.030, 2017.

Zhan, Z., Mechanisms and Implications of Deep Earthquakes, *Annual Review of Earth and Planetary Sciences*, *48*(1), 147–174, doi:10.1146/annurev-earth-053018-060314, 2020.

Zhang, H., S. van der Lee, C. R. Bina, and Z. Ge, Deep dehydration as a plausible mechanism of the 2013 mw 8.3 sea of okhotsk deep-focus earthquake, *Frontiers in Earth Science*, *9*, 521,220, 2021.

Appendix A: Permission for Published Material

JOHN WILEY AND SONS LICENSE
TERMS AND CONDITIONS

Aug 11, 2023

This Agreement between University of California, Davis -- Rebecca Fildes ("You") and John Wiley and Sons ("John Wiley and Sons") consists of your license details and the terms and conditions provided by John Wiley and Sons and Copyright Clearance Center.

License Number	5606050379917
License date	Aug 11, 2023
Licensed Content Publisher	John Wiley and Sons
Licensed Content Publication	Earth and Space Science
Licensed Content Title	Interevent Seismicity Statistics Associated With the 2018 Quasiperiodic Collapse Events at Kīlauea, HI, USA
Licensed Content Author	John B. Rundle, Donald L. Turcotte, Louise H. Kellogg, et al
Licensed Content Date	Mar 10, 2020
Licensed Content Volume	7
Licensed Content Issue	3
Licensed Content Pages	12
Type of use	Dissertation/Thesis

Requestor type	Author of this Wiley article
Format	Print and electronic
Portion	Full article
Will you be translating?	No
Title	Earthquakes of Varying Depths: Understanding Seismicity at Volcanic Summits and in Subducting Slabs
Institution name	University of California, Davis
Expected presentation date	Sep 2023
Requestor Location	University of California, Davis 1 Shields Ave DAVIS, CA 95616 United States Attn: University of California, Davis
Publisher Tax ID	EU826007151
Total	0.00 USD

Terms and Conditions

TERMS AND CONDITIONS

119

Terms and Conditions

- The materials you have requested permission to reproduce or reuse (the "Wiley Materials") are protected by copyright.

- You are hereby granted a personal, non-exclusive, non-sub licensable (on a stand-alone basis), non-transferable, worldwide, limited license to reproduce the Wiley Materials for the purpose specified in the licensing process. This license, **and any CONTENT (PDF or image file) purchased as part of your order,** is for a one-time use only and limited to any maximum distribution number specified in the license. The first instance of republication or reuse granted by this license must be completed within two years of the date of the grant of this license (although copies prepared before the end date may be distributed thereafter). The Wiley Materials shall not be used in any other manner or for any other purpose, beyond what is granted in the license. Permission is granted subject to an appropriate acknowledgement given to the author, title of the material/book/journal and the publisher. You shall also duplicate the copyright notice that appears in the Wiley publication in your use of the Wiley Material. Permission is also granted on the understanding that nowhere in the text is a previously published source acknowledged for all or part of this Wiley Material. Any third party content is expressly excluded from this permission.

- With respect to the Wiley Materials, all rights are reserved. Except as expressly granted by the terms of the license, no part of the Wiley Materials may be copied, modified, adapted (except for minor reformatting required by the new Publication), translated, reproduced, transferred or distributed, in any form or by any means, and no derivative works may be made based on the Wiley Materials without the prior permission of the respective copyright owner.**For STM Signatory Publishers clearing permission under the terms of the STM Permissions Guidelines only, the terms of the license are extended to include subsequent editions and for editions in other languages, provided such editions are for the work as a whole in situ and does not involve the separate exploitation of the permitted figures or extracts,** You may not alter, remove or suppress in any manner any copyright, trademark or other notices displayed by the Wiley Materials. You may not license, rent, sell, loan, lease, pledge, offer as security, transfer or assign the Wiley Materials on a stand-alone basis, or any of the rights granted to you hereunder to any other person.

- The Wiley Materials and all of the intellectual property rights therein shall at all times remain the exclusive property of John Wiley & Sons Inc, the Wiley Companies, or their respective licensors, and your interest therein is only that of having possession of and the right to reproduce the Wiley Materials pursuant to Section 2 herein during the continuance of this Agreement. You agree that you own no right, title or interest in or to the Wiley Materials or any of the intellectual property rights therein. You shall have no rights hereunder other than the license as provided for above in Section 2. No right, license or interest to any trademark, trade name, service mark or other branding ("Marks") of WILEY or its licensors is granted hereunder, and you agree that you shall not assert any such right, license or interest with respect thereto

- NEITHER WILEY NOR ITS LICENSORS MAKES ANY WARRANTY OR REPRESENTATION OF ANY KIND TO YOU OR ANY THIRD PARTY, EXPRESS, IMPLIED OR STATUTORY, WITH RESPECT TO THE MATERIALS OR THE ACCURACY OF ANY INFORMATION CONTAINED IN THE MATERIALS, INCLUDING, WITHOUT LIMITATION, ANY IMPLIED WARRANTY OF MERCHANTABILITY, ACCURACY, SATISFACTORY QUALITY, FITNESS FOR

120

A PARTICULAR PURPOSE, USABILITY, INTEGRATION OR NON-INFRINGEMENT AND ALL SUCH WARRANTIES ARE HEREBY EXCLUDED BY WILEY AND ITS LICENSORS AND WAIVED BY YOU.

- WILEY shall have the right to terminate this Agreement immediately upon breach of this Agreement by you.

- You shall indemnify, defend and hold harmless WILEY, its Licensors and their respective directors, officers, agents and employees, from and against any actual or threatened claims, demands, causes of action or proceedings arising from any breach of this Agreement by you.

- IN NO EVENT SHALL WILEY OR ITS LICENSORS BE LIABLE TO YOU OR ANY OTHER PARTY OR ANY OTHER PERSON OR ENTITY FOR ANY SPECIAL, CONSEQUENTIAL, INCIDENTAL, INDIRECT, EXEMPLARY OR PUNITIVE DAMAGES, HOWEVER CAUSED, ARISING OUT OF OR IN CONNECTION WITH THE DOWNLOADING, PROVISIONING, VIEWING OR USE OF THE MATERIALS REGARDLESS OF THE FORM OF ACTION, WHETHER FOR BREACH OF CONTRACT, BREACH OF WARRANTY, TORT, NEGLIGENCE, INFRINGEMENT OR OTHERWISE (INCLUDING, WITHOUT LIMITATION, DAMAGES BASED ON LOSS OF PROFITS, DATA, FILES, USE, BUSINESS OPPORTUNITY OR CLAIMS OF THIRD PARTIES), AND WHETHER OR NOT THE PARTY HAS BEEN ADVISED OF THE POSSIBILITY OF SUCH DAMAGES. THIS LIMITATION SHALL APPLY NOTWITHSTANDING ANY FAILURE OF ESSENTIAL PURPOSE OF ANY LIMITED REMEDY PROVIDED HEREIN.

- Should any provision of this Agreement be held by a court of competent jurisdiction to be illegal, invalid, or unenforceable, that provision shall be deemed amended to achieve as nearly as possible the same economic effect as the original provision, and the legality, validity and enforceability of the remaining provisions of this Agreement shall not be affected or impaired thereby.

- The failure of either party to enforce any term or condition of this Agreement shall not constitute a waiver of either party's right to enforce each and every term and condition of this Agreement. No breach under this agreement shall be deemed waived or excused by either party unless such waiver or consent is in writing signed by the party granting such waiver or consent. The waiver by or consent of a party to a breach of any provision of this Agreement shall not operate or be construed as a waiver of or consent to any other or subsequent breach by such other party.

- This Agreement may not be assigned (including by operation of law or otherwise) by you without WILEY's prior written consent.

- Any fee required for this permission shall be non-refundable after thirty (30) days from receipt by the CCC.

- These terms and conditions together with CCC's Billing and Payment terms and conditions (which are incorporated herein) form the entire agreement between you and WILEY concerning this licensing transaction and (in the absence of fraud) supersedes all prior agreements and representations of the parties, oral or written. This Agreement may not be amended except in writing signed by both parties. This Agreement shall be binding upon and inure to the benefit of the parties' successors, legal representatives,

121

and authorized assigns.

- In the event of any conflict between your obligations established by these terms and conditions and those established by CCC's Billing and Payment terms and conditions, these terms and conditions shall prevail.

- WILEY expressly reserves all rights not specifically granted in the combination of (i) the license details provided by you and accepted in the course of this licensing transaction, (ii) these terms and conditions and (iii) CCC's Billing and Payment terms and conditions.

- This Agreement will be void if the Type of Use, Format, Circulation, or Requestor Type was misrepresented during the licensing process.

- This Agreement shall be governed by and construed in accordance with the laws of the State of New York, USA, without regards to such state's conflict of law rules. Any legal action, suit or proceeding arising out of or relating to these Terms and Conditions or the breach thereof shall be instituted in a court of competent jurisdiction in New York County in the State of New York in the United States of America and each party hereby consents and submits to the personal jurisdiction of such court, waives any objection to venue in such court and consents to service of process by registered or certified mail, return receipt requested, at the last known address of such party.

WILEY OPEN ACCESS TERMS AND CONDITIONS

Wiley Publishes Open Access Articles in fully Open Access Journals and in Subscription journals offering Online Open. Although most of the fully Open Access journals publish open access articles under the terms of the Creative Commons Attribution (CC BY) License only, the subscription journals and a few of the Open Access Journals offer a choice of Creative Commons Licenses. The license type is clearly identified on the article.

The Creative Commons Attribution License

The Creative Commons Attribution License (CC-BY) allows users to copy, distribute and transmit an article, adapt the article and make commercial use of the article. The CC-BY license permits commercial and non-

Creative Commons Attribution Non-Commercial License

The Creative Commons Attribution Non-Commercial (CC-BY-NC)License permits use, distribution and reproduction in any medium, provided the original work is properly cited and is not used for commercial purposes.(see below)

Creative Commons Attribution-Non-Commercial-NoDerivs License

The Creative Commons Attribution Non-Commercial-NoDerivs License (CC-BY-NC-ND) permits use, distribution and reproduction in any medium, provided the original work is properly cited, is not used for commercial purposes and no modifications or adaptations are made. (see below)

Use by commercial "for-profit" organizations

122

Use of Wiley Open Access articles for commercial, promotional, or marketing purposes requires further explicit permission from Wiley and will be subject to a fee.

Further details can be found on Wiley Online Library
http://olabout.wiley.com/WileyCDA/Section/id-410895.html

Other Terms and Conditions:

v1.10 Last updated September 2015

Questions? customercare@copyright.com.

123

JOHN WILEY AND SONS LICENSE
TERMS AND CONDITIONS

Aug 11, 2023

This Agreement between University of California, Davis -- Rebecca Fildes ("You") and John Wiley and Sons ("John Wiley and Sons") consists of your license details and the terms and conditions provided by John Wiley and Sons and Copyright Clearance Center.

License Number	5606050191126
License date	Aug 11, 2023
Licensed Content Publisher	John Wiley and Sons
Licensed Content Publication	Earth and Space Science
Licensed Content Title	Natural Time Analysis and Nowcasting of Quasi−Periodic Collapse Events During the 2018 Kīlauea Volcano Eruptive Sequence
Licensed Content Author	John B. Rundle, Donald L. Turcotte, Rebecca A. Fildes
Licensed Content Date	Aug 4, 2022
Licensed Content Volume	9
Licensed Content Issue	8
Licensed Content Pages	14

124

Type of use	Dissertation/Thesis
Requestor type	Author of this Wiley article
Format	Print and electronic
Portion	Full article
Will you be translating?	No
Title	Earthquakes of Varying Depths: Understanding Seismicity at Volcanic Summits and in Subducting Slabs
Institution name	University of California, Davis
Expected presentation date	Sep 2023
Requestor Location	University of California, Davis 1 Shields Ave DAVIS, CA 95616 United States Attn: University of California, Davis
Publisher Tax ID	EU826007151
Total	0.00 USD

Terms and Conditions

TERMS AND CONDITIONS

125

Clearance Center Inc., ("CCC's Billing and Payment terms and conditions"), at the time that you opened your RightsLink account (these are available at any time at http://myaccount.copyright.com).

Terms and Conditions

- The materials you have requested permission to reproduce or reuse (the "Wiley Materials") are protected by copyright.

- You are hereby granted a personal, non-exclusive, non-sub licensable (on a stand-alone basis), non-transferable, worldwide, limited license to reproduce the Wiley Materials for the purpose specified in the licensing process. This license, **and any CONTENT (PDF or image file) purchased as part of your order,** is for a one-time use only and limited to any maximum distribution number specified in the license. The first instance of republication or reuse granted by this license must be completed within two years of the date of the grant of this license (although copies prepared before the end date may be distributed thereafter). The Wiley Materials shall not be used in any other manner or for any other purpose, beyond what is granted in the license. Permission is granted subject to an appropriate acknowledgement given to the author, title of the material/book/journal and the publisher. You shall also duplicate the copyright notice that appears in the Wiley publication in your use of the Wiley Material. Permission is also granted on the understanding that nowhere in the text is a previously published source acknowledged for all or part of this Wiley Material. Any third party content is expressly excluded from this permission.

- With respect to the Wiley Materials, all rights are reserved. Except as expressly granted by the terms of the license, no part of the Wiley Materials may be copied, modified, adapted (except for minor reformatting required by the new Publication), translated, reproduced, transferred or distributed, in any form or by any means, and no derivative works may be made based on the Wiley Materials without the prior permission of the respective copyright owner.**For STM Signatory Publishers clearing permission under the terms of the STM Permissions Guidelines only, the terms of the license are extended to include subsequent editions and for editions in other languages, provided such editions are for the work as a whole in situ and does not involve the separate exploitation of the permitted figures or extracts,** You may not alter, remove or suppress in any manner any copyright, trademark or other notices displayed by the Wiley Materials. You may not license, rent, sell, loan, lease, pledge, offer as security, transfer or assign the Wiley Materials on a stand-alone basis, or any of the rights granted to you hereunder to any other person.

- The Wiley Materials and all of the intellectual property rights therein shall at all times remain the exclusive property of John Wiley & Sons Inc, the Wiley Companies, or their respective licensors, and your interest therein is only that of having possession of and the right to reproduce the Wiley Materials pursuant to Section 2 herein during the continuance of this Agreement. You agree that you own no right, title or interest in or to the Wiley Materials or any of the intellectual property rights therein. You shall have no rights hereunder other than the license as provided for above in Section 2. No right, license or interest to any trademark, trade name, service mark or other branding ("Marks") of WILEY or its licensors is granted hereunder, and you agree that you shall not assert any such right, license or interest with respect thereto

- NEITHER WILEY NOR ITS LICENSORS MAKES ANY WARRANTY OR REPRESENTATION OF ANY KIND TO YOU OR ANY THIRD PARTY, EXPRESS,

126

IMPLIED OR STATUTORY, WITH RESPECT TO THE MATERIALS OR THE
ACCURACY OF ANY INFORMATION CONTAINED IN THE MATERIALS,
INCLUDING, WITHOUT LIMITATION, ANY IMPLIED WARRANTY OF
MERCHANTABILITY, ACCURACY, SATISFACTORY QUALITY, FITNESS FOR
A PARTICULAR PURPOSE, USABILITY, INTEGRATION OR NON-
INFRINGEMENT AND ALL SUCH WARRANTIES ARE HEREBY EXCLUDED
BY WILEY AND ITS LICENSORS AND WAIVED BY YOU.

- WILEY shall have the right to terminate this Agreement immediately upon breach of
  this Agreement by you.

- You shall indemnify, defend and hold harmless WILEY, its Licensors and their
  respective directors, officers, agents and employees, from and against any actual or
  threatened claims, demands, causes of action or proceedings arising from any breach
  of this Agreement by you.

- IN NO EVENT SHALL WILEY OR ITS LICENSORS BE LIABLE TO YOU OR
  ANY OTHER PARTY OR ANY OTHER PERSON OR ENTITY FOR ANY
  SPECIAL, CONSEQUENTIAL, INCIDENTAL, INDIRECT, EXEMPLARY OR
  PUNITIVE DAMAGES, HOWEVER CAUSED, ARISING OUT OF OR IN
  CONNECTION WITH THE DOWNLOADING, PROVISIONING, VIEWING OR
  USE OF THE MATERIALS REGARDLESS OF THE FORM OF ACTION,
  WHETHER FOR BREACH OF CONTRACT, BREACH OF WARRANTY, TORT,
  NEGLIGENCE, INFRINGEMENT OR OTHERWISE (INCLUDING, WITHOUT
  LIMITATION, DAMAGES BASED ON LOSS OF PROFITS, DATA, FILES, USE,
  BUSINESS OPPORTUNITY OR CLAIMS OF THIRD PARTIES), AND WHETHER
  OR NOT THE PARTY HAS BEEN ADVISED OF THE POSSIBILITY OF SUCH
  DAMAGES. THIS LIMITATION SHALL APPLY NOTWITHSTANDING ANY
  FAILURE OF ESSENTIAL PURPOSE OF ANY LIMITED REMEDY PROVIDED
  HEREIN.

- Should any provision of this Agreement be held by a court of competent jurisdiction to
  be illegal, invalid, or unenforceable, that provision shall be deemed amended to
  achieve as nearly as possible the same economic effect as the original provision, and
  the legality, validity and enforceability of the remaining provisions of this Agreement
  shall not be affected or impaired thereby.

- The failure of either party to enforce any term or condition of this Agreement shall not
  constitute a waiver of either party's right to enforce each and every term and condition
  of this Agreement. No breach under this agreement shall be deemed waived or
  excused by either party unless such waiver or consent is in writing signed by the party
  granting such waiver or consent. The waiver by or consent of a party to a breach of
  any provision of this Agreement shall not operate or be construed as a waiver of or
  consent to any other or subsequent breach by such other party.

- This Agreement may not be assigned (including by operation of law or otherwise) by
  you without WILEY's prior written consent.

- Any fee required for this permission shall be non-refundable after thirty (30) days
  from receipt by the CCC.

- These terms and conditions together with CCC's Billing and Payment terms and
  conditions (which are incorporated herein) form the entire agreement between you and
  WILEY concerning this licensing transaction and (in the absence of fraud) supersedes

127

all prior agreements and representations of the parties, oral or written. This Agreement may not be amended except in writing signed by both parties. This Agreement shall be binding upon and inure to the benefit of the parties' successors, legal representatives, and authorized assigns.

- In the event of any conflict between your obligations established by these terms and conditions and those established by CCC's Billing and Payment terms and conditions, these terms and conditions shall prevail.

- WILEY expressly reserves all rights not specifically granted in the combination of (i) the license details provided by you and accepted in the course of this licensing transaction, (ii) these terms and conditions and (iii) CCC's Billing and Payment terms and conditions.

- This Agreement will be void if the Type of Use, Format, Circulation, or Requestor Type was misrepresented during the licensing process.

- This Agreement shall be governed by and construed in accordance with the laws of the State of New York, USA, without regards to such state's conflict of law rules. Any legal action, suit or proceeding arising out of or relating to these Terms and Conditions or the breach thereof shall be instituted in a court of competent jurisdiction in New York County in the State of New York in the United States of America and each party hereby consents and submits to the personal jurisdiction of such court, waives any objection to venue in such court and consents to service of process by registered or certified mail, return receipt requested, at the last known address of such party.

WILEY OPEN ACCESS TERMS AND CONDITIONS

Wiley Publishes Open Access Articles in fully Open Access Journals and in Subscription journals offering Online Open. Although most of the fully Open Access journals publish open access articles under the terms of the Creative Commons Attribution (CC BY) License only, the subscription journals and a few of the Open Access Journals offer a choice of Creative Commons Licenses. The license type is clearly identified on the article.

The Creative Commons Attribution License

The [Creative Commons Attribution License (CC-BY)](#) allows users to copy, distribute and transmit an article, adapt the article and make commercial use of the article. The CC-BY license permits commercial and non-

Creative Commons Attribution Non-Commercial License

The [Creative Commons Attribution Non-Commercial (CC-BY-NC)License](#) permits use, distribution and reproduction in any medium, provided the original work is properly cited and is not used for commercial purposes.(see below)

Creative Commons Attribution-Non-Commercial-NoDerivs License

The [Creative Commons Attribution Non-Commercial-NoDerivs License](#) (CC-BY-NC-ND) permits use, distribution and reproduction in any medium, provided the original work is properly cited, is not used for commercial purposes and no modifications or adaptations are made. (see below)

128

Use by commercial "for-profit" organizations

Use of Wiley Open Access articles for commercial, promotional, or marketing purposes requires further explicit permission from Wiley and will be subject to a fee.

Further details can be found on Wiley Online Library
http://olabout.wiley.com/WileyCDA/Section/id-410895.html

Other Terms and Conditions:

v1.10 Last updated September 2015

Questions? customercare@copyright.com.

129